Summer 2014

Bivariate Doubly Inflated Poisson and Related Regression Models

Pooja Sengupta
Old Dominion University

Recommended Citation

Sengupta, Pooja. "Bivariate Doubly Inflated Poisson and Related Regression Models" (2014). Doctor of Philosophy (PhD), dissertation, Mathematics and Statistics, Old Dominion University, DOI: 10.25777/pj3y-3255
https://digitalcommons.odu.edu/mathstat_etds/59

A LEAST SQUARES CLOSURE APPROXIMATION FOR LIQUID CRYSTALLINE POLYMERS

by

Traci Ann Sievenpiper
B.S. April 2002, University of Pittsburgh
M.S. May 2008, Old Dominion University

A Dissertation Submitted to the Faculty of
Old Dominion University in Partial Fulfillment of the
Requirement for the Degree of

DOCTOR OF PHILOSOPHY

MATHEMATICS AND STATISTICS

OLD DOMINION UNIVERSITY
May 2011

Approved by:

Ruhai Zhou (Director)

Richard Gregory (Member)

Fang Hu (Member)

Hideaki Kaneko (Member)

Gordon Melrose (Member)

ABSTRACT

A LEAST SQUARES CLOSURE APPROXIMATION FOR LIQUID CRYSTALLINE POLYMERS

Traci Ann Sievenpiper
Old Dominion University, 2011
Director: Dr. Ruhai Zhou

An introduction to existing closure schemes for the Doi-Hess kinetic theory of liquid crystalline polymers is provided. A new closure scheme is devised based on a least squares fit of a linear combination of the Doi, Tsuji-Rey, Hinch-Leal I, and Hinch-Leal II closure schemes. The orientation tensor and rate-of-strain tensor are fit separately using data generated from the kinetic solution of the Smoluchowski equation. The known behavior of the kinetic solution and existing closure schemes at equilibrium is compared with that of the new closure scheme. The performance of the proposed closure scheme in simple shear flow for a variety of shear rates and nematic polymer concentrations is examined, along with that of the four selected existing closure schemes. The flow phase diagram for the proposed closure scheme under the conditions of shear flow is constructed and compared with that of the kinetic solution. The study of the closure scheme is extended to the simulation of nematic polymers in plane Couette cells. The results are compared with existing kinetic simulations for a Landau-deGennes mesoscopic model with the application of a parameterized closure approximation. The proposed closure scheme is shown to produce a reasonable approximation to the kinetic results in the case of simple shear flow and plane Couette flow.

ACKNOWLEDGMENTS

I would like to thank my family for their patience, love, and support. I would like to thank my colleagues and committee for their time and guidance. Lastly, I would like to thank my advisor for agreeing to work on this project with me over several geographical moves, a new baby, and numerous other surprises life brought my way. His patience and encouragement were greatly appreciated.

TABLE OF CONTENTS

APPENDICES

LIST OF TABLES

LIST OF FIGURES

CHAPTER I

INTRODUCTION

The interest in simulating liquid crystalline polymers comes from their applications in materials manufacturing. In general, a liquid crystalline polymer describes a polymer which has the fluidity of a liquid and the molecular ordering of a crystal. In particular, nematic liquid crystalline polymers are rigid rod-like or disk-like spheroids. All molecules tend to have a uniaxial symmetry and are oriented along some direction, being almost parallel to one another [2]. They are anisotropic and elastic. They can store stresses that depend on the orientation of the molecules [3]. The complex structures of nematic polymers create a variety of bulk properties of materials including: electrical conductivity, thermal conductivity, strength, gas impermeability, liquid impermeability, and they are lightweight [4, 5]. Liquid crystalline polymers are essential in the production of desired high-performance materials such as aircraft parts, liquid crystal displays (LCDs), and bullet-proof vests (Kevlar). Much of the development of super strong polymers today is done through experimentation. In an effort to reduce experimentation time and streamline this process, researchers are trying to better understand how these materials form. Of particular interest is the potential to injection mold liquid crystalline polymers into high strength parts [4,6]. Injection molding is the process by which a molten material, often a plastic, is forced into a preformed die. The flow experienced by molecules during the injection molding process is very complicated, and so it is not easy to determine their final orientation which has a direct correlation to the physical properties of the material. In contrast, during the extrusion of fibers processing operation, the flowing material experiences mostly elongational flow. The result is that the polymers tend to orient along the flow direction [4].

Over the past few decades, liquid crystalline polymers in the nematic phase have been successfully modeled by S. Z. Hess, M. Doi, G. Marrucci, P.L. Maffettone, R.G. Larson, and H.C. Ottinger. In most studies, the orientation of the rigid-rod nematic polymers are described in terms of a probability distribution function [1,4,6–18]. This is referred to as the Doi or Doi-Hess kinetic theory for liquid crystalline polymers [19, 20]. This approach involves solving a differential equation for a second order moment tensor which describes the orientation of the polymers. In order to solve for the second moment tensor, information from higher moments must be known, which in turn rely on even higher moments. This can be solved numerically through the use of spherical harmonic expansions [1,8,9,14]. This method is computationally intensive, even in the simplest flow cases such as homogeneous shear flow. As a result, closure approximations are employed to represent the higher order moments in terms of the lower second order moments. This results in the differential equation being a closed system written in terms of second moment tensors which, computationally speaking, is significantly less expensive to solve. More recently, studies have been conducted where the orientation of the rigid-rod nematic polymers are described in terms of hierarchy of alignment tensors [5]. Again, this means that lower order moments rely on higher order moments resulting in a need for closure approximations.

The simplest closure for liquid crystalline polymers is the Doi closure [19, 21]. Under equilibrium conditions, the exact solution for the Doi-Hess kinetic theory has two critical bifurcation points [8–10]. The Doi closure does not give an accurate prediction for these points under equilibrium conditions [10, 21]. For simple shear flow, the Doi closure does not simulate any of the periodic flow states [4, 6, 13, 21]. In general, homogeneous shear flow is considered to be one of the most difficult flow types for the closure schemes to approximate. As a result, there is a wealth of information for both the kinetic solution and the solution simulated using various closure schemes under simple shear flow conditions. For more complex flows such as elongational flows [10], fiber flows [11], and extrusion dominated flows [6], the Doi closure outperforms many of the other closure rules. The two Hinch-Leal closures [22] are more complicated to implement and less testing has been done of them. They were derived in an *ad hoc* manor with the main purpose being to capture the two critical bifurcation points of the equilibrium solution to the kinetic equation. The first Hinch-Leal closure is the simpler of the two. Like the Doi closure, it does not give an exact solution to the critical bifurcation points at equilibrium [10]. However, the first Hinch-Leal does predict periodic flow under homogeneous shear flow conditions. Under stronger shear flow conditions, its results are abnormally bad [6, 13]. The second Hinch-Leal closure introduces an exponential term into the closure approximation. The exponential term makes it very difficult to do any non-numerical analysis on the closure scheme. Unlike the Doi and first Hinch-Leal closures, the second Hinch-Leal closure does give an accurate prediction of the two critical bifurcation points from the kinetic solution [10]. Similar to the performance of the first Hinch-Leal closure under shear flow conditions, the second closure scheme predicts periodic flow and has pathological results under strong shear flow conditions. For strong flow conditions in near shear flow, the second Hinch-Leal closure simulates spurious periodic flow [6,13]. Under the conditions of complex flows, the Hinch-Leal closures do not outperform the Doi closure [10,11].

More recently, the Tsuji-Rey and Bingham closures have been suggested. The Tsuji-Rey closure differs from the other closures in that it is written completely in terms of second-order traceless tensors [3]. Qualitatively, its performance under equilibrium conditions and in the case of simple shear flow is similar to the performance of the Doi closure rule [13], but it does have the advantage of predicting some periodic flow. The Bingham closure is a closure approximation for nematic polymers based on the canonical distribution subspace theory, specifically the Bingham distribution [4]. Like the second Hinch-Leal closure, this closure gives an accurate prediction of the two critical bifurcation points from the kinetic solution under equilibrium conditions. Unlike the Doi, Tsuji-Rey, and Hinch-Leal closures, the Bingham closure performs well over a wide range of parameters and it is therefore a better approximation to the exact Doi kinetic theory for the homogeneous shear flow problem [4,6]. However, it also has its fair share of shortcomings. While the Bingham closure predicts all types of periodic flow and the subsequent chaos flow phase, it fails to predict the return of the flow-aligning phase at high shear rates [7]. For more complex flows, such as the flow between rotating eccentric cylinders, the Bingham closure only behaves satisfactorily at low shear rates [17].

In addition to the Doi, Tsuji-Rey, first and second Hinch-Leal closures, and the Bingham closures, there are many other closures such as those derived from alignment tensors [5] or hybrids of the above closures [10,11]. As a general rule, they all have some defect when compared with the kinetic solution at equilibrium or under simple shear flow conditions. Further, considering the vast array of complex flow types, it is very difficult to compare the results from simulations utilizing closure schemes in order to determine which is best for complex flow. It is clear that none of the closures rules discussed are perfect and there is not a "one size fits all" closure in terms of all flow types.

In summary, the time and monetary cost of experimentally producing new super strong polymers is very high. As a results, scientists and engineers are interested in being able to model these materials. However, the mathematical model is computationally intensive in its original kinetic form. Specifically, the solution depends on information from higher order moments. As a result, the kinetic equations utilize closure rules which approximate higher order moments in terms of lower order moments and thus produce a closed system of differential equations. However, the current closure schemes have many shortcomings and therefore there is a need to derive a better closure scheme. Ideally, a new closure scheme would be more accurate in both the equilibrium and shear flow conditions. In the case of more complex flows it should perform as well as the other closure schemes, as comparison with the kinetic solution is not possible. In Ottinger's recent paper "On the Stupendous Beauty of Closure" [18], he suggests that "closure should not be considered as a helpful mathematical approximation but as the cornerstone of establishing autonomous levels of description." Considering the discussion above and Ottinger's statement, it is evident that there is a need to develop an improved closure scheme.

CHAPTER II

LEAST SQUARES FIT

In this chapter, a new closure rule is derived using a least squares fit on data that is simulated from existing closure rules. First, the Doi kinetic theory is introduced and the computational costs of simulating it is discussed. Next, the four existing closure rules used in the least squares fit are defined and the application of general least squares on their simulated data is presented in detail. Finally, a new closure rule, referred to as the DQ closure, is proposed.

II.1 THE DOI KINETIC THEORY

Let $f(\mathbf{m},t)$ describe the orientational probability distribution function (PDF) for rigid, rod-like or plate-like, spheroidal molecules with axis of symmetry $\mathbf{m}$ on the unit sphere. The dimensionless Smoluchowski (kinetic) equation for $f(\mathbf{m},t)$ is given by [1, 2, 8, 12–14]:

$$\frac{Df}{Dt} = \mathcal{R}\cdot\left[D_r(\mathbf{m})\left(\mathcal{R}f+\frac{1}{kT}f\mathcal{R}V\right)\right]-\mathcal{R}\cdot\left[\mathbf{m}\times\dot{\mathbf{m}}f\right], \quad (1)$$

with Jeffrey orbit [1, 8, 12–14]

$$\dot{\mathbf{m}} = \mathbf{\Omega}\cdot\mathbf{m}+a\left[\mathbf{D}\cdot\mathbf{m}-\mathbf{D}:\mathbf{mmm}\right], \quad (2)$$

where $D_r(\mathbf{m})$ is the dimensionless rotational diffusion coefficient; $\mathcal{R}$ is the rotational gradient operator $\mathcal{R}=\mathbf{m}\times\frac{\partial}{\partial\mathbf{m}}$; k is the Boltzmann constant; T is the absolute temperature; $\mathbf{D}$ and $\mathbf{\Omega}$ denote the dimensionless rate-of-strain and vorticity tensors in the flow field $\mathbf{v}$,

$$\mathbf{D}=\frac{1}{2}(\nabla\mathbf{v}+\nabla\mathbf{v}^T), \qquad \mathbf{\Omega}=\frac{1}{2}(\nabla\mathbf{v}-\nabla\mathbf{v}^T). \quad (3)$$

In this chapter, only simple shear flow is considered. That is, the velocity, $\mathbf{v} = Pe(y,0,0)$, is linear in the flow gradient direction y (x is the flow direction, and z is the vorticity direction) [1, 8, 14]. It follows directly from (3), that $\mathbf{D}$ and $\mathbf{\Omega}$ can be written as:

$$\mathbf{D}=\frac{Pe}{2}\begin{pmatrix}0&1&0\\1&0&0\\0&0&0\end{pmatrix} \qquad \mathbf{\Omega}=\frac{Pe}{2}\begin{pmatrix}0&1&0\\-1&0&0\\0&0&0\end{pmatrix}, \quad (4)$$

where the Peclet number, Pe, is the normalized flow rate parameter. The geometry parameter a from the Jeffrey orbit (2) is given by,

$$a = \frac{r^2 - 1}{r^2 + 1}, \tag{5}$$

which parametrizes the effect of the molecular aspect ratio $r = L/d$ of the length L of the rigid rod (or the thickness of the plate) to the diameter d of the circular traverse cross-section as depicted in Fig 1. Fig. 2 is the graph of geometry parameter a as a function of molecular aspect ratio r from (5) which shows that, for an extremely long rod, the $\lim_{r \to \infty} a = 1$; while for an extremely thin plate, $\lim_{r \to 0} a = -1$. Because of the symmetry results [13, 23] between a and $-a$, only $a > 0$ is considered. Also, a typical physical value of r is $r = 50$, which makes $a \approx 0.98$. Therefore, the geometry parameter is simply taken to be $a = 1.0$ in this research.

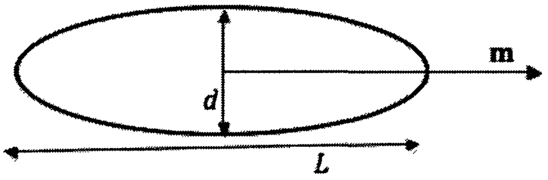

FIG. 1: Rigid-rod molecule with length L of the symmetry axis $\mathbf{m}$ and diameter d of the circular traverse cross-section.

The second moment of the PDF, $\mathbf{M}$, determines the Maier-Saupe mean-field excluded-volume potential, V, with dimensionless nematic polymer concentration N [1, 12, 17].

$$\begin{aligned} \mathbf{M} &= \langle \mathbf{mm} \rangle = \int_{\|\mathbf{m}\|=1} \mathbf{mm} f(\mathbf{m}, t)\, d\mathbf{m}; && (6) \\ V &= -\frac{3}{2} N k T \mathbf{mm} : \mathbf{M}. && (7) \end{aligned}$$

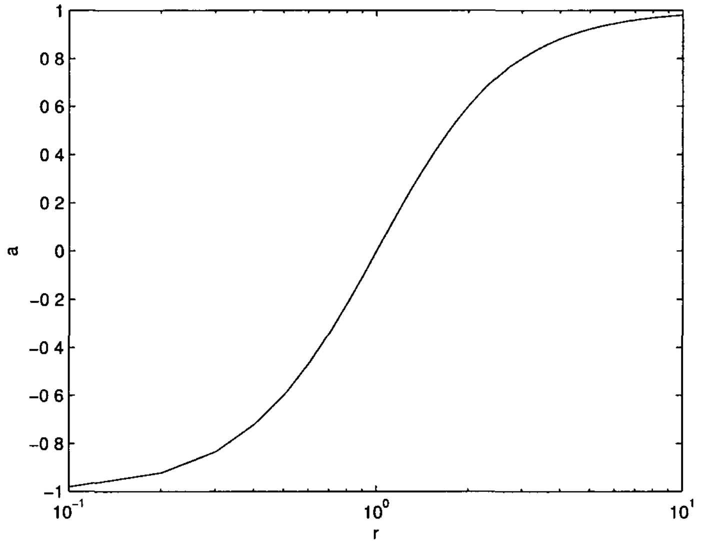

FIG. 2: Semi-log graph of geometry parameter a as a function of molecular aspect ratio r.

Where the symbol $\langle\cdot\rangle$ indicates the average taken over the unit sphere, and the second moment has the characteristic $tr(\mathbf{M}) = 1$. Note, there are some other potentials, for example the Onsager potential [24], but here only the Maier-Saupe potential is used.

The Smoluchowski equation (1) is very complicated to solve in its current form, especially when heterogeneity is introduced into the system. Solutions of the differential equation can be found in the form of spherical harmonic expansions. The result is a system of infinitely many differential equations that can be solved numerically after suitable truncation at a high computational cost [9, 13, 14, 25]. Usually, the kinetic equation is referred to as an infinitely many dimensional problem Instead of solving this problem, mathematicians and scientists have derived an alternate method to solve the dynamic equation of the second moment orientation tensor $\mathbf{Q}$, where $\mathbf{Q}$ is the traceless portion of $\mathbf{M}$

$$\mathbf{Q} = \mathbf{M} - \frac{1}{3}\mathbf{I}, \tag{8}$$

which is symmetric. The resulting system is, therefore, only 5-dimensional.

Taking the second moment of the kinetic equation, the dimensionless dynamic equation [12, 13] for $\mathbf{Q}$ is:

$$\frac{\partial \mathbf{Q}}{\partial t} - \boldsymbol{\Omega} \cdot \mathbf{Q} + \mathbf{Q} \cdot \boldsymbol{\Omega} - a\left[\mathbf{D} \cdot \mathbf{Q} + \mathbf{Q} \cdot \mathbf{D}\right]$$
$$= \frac{2}{3}a\mathbf{D} - 2a\mathbf{D} : \langle \mathbf{mmmm} \rangle - \frac{1}{\Lambda}\left[\mathbf{Q} - N\left(\mathbf{Q} + \frac{1}{3}\mathbf{I}\right) \cdot \mathbf{Q} + N\mathbf{Q} : \langle \mathbf{mmmm} \rangle\right] \quad (9)$$

where Λ is the approximation for D_r^{-1}. It is in the dimensionless dynamic equation (9) that the fourth order tensor $\langle \mathbf{mmmm} \rangle$ appears. This term results in the second order system having a dependency on higher (fourth) order moments. Upon close inspection of (9) it can be seen that $\langle \mathbf{mmmm} \rangle$ does not need to be explicitly known in order for $\mathbf{Q}$ to be solved, rather the second order tensors which result from the tensor contractions $\mathbf{D} : \langle \mathbf{mmmm} \rangle$ and $\mathbf{Q} : \langle \mathbf{mmmm} \rangle$ must be determined. A description of the tensor notation can be found in the appendix. While the exact values of these contractions cannot be calculated without deriving the fourth moment equation for $\langle \mathbf{mmmm} \rangle$, an approximation to the contractions in terms of lower (second) moments can be made. These approximations have been widely used in the literature and are referred to as closure rules or closure schemes. Some well known ones are the Doi closure, Tsuji-Rey closure, Hinch-Leal 1 closure and Hinch-Leal 2 closure (see Table I below). As discussed in the introduction, these rules capture some of the phenomena described in the kinetic equation, but no single closure gives satisfactory results for all flow conditions. The purpose here is to derive a new rule based on the numerical simulations of the kinetic equation in an effort to get better results.

$\mathbf{M}$ and $\mathbf{Q}$ share an orthonormal frame of eigenvectors, referred to as optical axes or directors, $\mathbf{n}_i, i = 1, 2, 3$, with $\mathbf{M}$ having corresponding ordered eigenvalues, $d_i, i = 1, 2, 3$, such that $0 \leq d_3 \leq d_2 \leq d_1 \leq 1$ for stable solutions and $d_1 + d_2 + d_3 = 1$. $\mathbf{Q}$ has eigenvalues $d_i - \frac{1}{3}$. The eigenvalues can be referred to in terms of order parameters, where each d_i describes the degree to which $\mathbf{m}$ is aligned with respect to the primary director $\mathbf{n}_i$. The major director is denoted by $\mathbf{n}_1$ for which d_1 is the unique maximum [8, 13].

From the spectral decomposition

$$\theta = \sum_i d_i \mathbf{n}_i \mathbf{n}_i, \quad (10)$$

the second moment equation (8) has an equivalent form in terms of the directors, $\mathbf{n}_i, i = 1, 2, 3$, (using the identity $\sum \mathbf{n}_i \mathbf{n}_i = \mathbf{I}$) [13]:

$$\mathbf{Q} = s\left(\mathbf{n}_1\mathbf{n}_1 - \frac{1}{3}\mathbf{I}\right) + \beta\left(\mathbf{n}_2\mathbf{n}_2 - \frac{1}{3}\mathbf{I}\right), \quad (11)$$

$$s = d_1 - d_3, \quad \beta = d_2 - d_3, \tag{12}$$

where the order parameters s and β describe the alignment of the axis. The maximum normalized birefringence is defined as the maximum of $|d_i - d_j|$ [13]. Birefringence is a physical property of liquid crystalline polymers; it describes how light passes through the optical axes. If $s = \beta = 0$, the system is in its isotropic phase and all eigenvalues are equal. The system is in its nematic uniaxial phase when $d_i = d_j \neq d_k$; there is one unique eigenvalue. Lastly, if all three eigenvalues differ, the nematic is biaxial and s and β are both non-zero [8, 13]. Geometrically, $\mathbf{M}$ and $\mathbf{Q}$ uniquely define an orientation axis and radius [13].

II.2 FORMULATION OF DQ CLOSURE RULE

Current closure rules were developed by devising a single approximation method that could describe both $\mathbf{D} : \langle \mathbf{mmmm} \rangle$ and $\mathbf{Q} : \langle \mathbf{mmmm} \rangle$ effectively. Recall that $\mathbf{D}$ is a rate of strain tensor with one non-zero independent component in the simple shear case, and $\mathbf{Q}$ is a symmetric and traceless second moment orientation tensor with five independent components. Since $\mathbf{D}$ and $\mathbf{Q}$ have different physical meanings, the approach taken in the development of the new closure rule is to treat $\mathbf{D}$ and $\mathbf{Q}$ separately. If preexisting closure rules for approximating $\mathbf{D} : \langle \mathbf{mmmm} \rangle$ and $\mathbf{Q} : \langle \mathbf{mmmm} \rangle$ are linearly combined in such a manner as to minimize their differences from the actual values for $\mathbf{D} : \langle \mathbf{mmmm} \rangle$ and $\mathbf{Q} : \langle \mathbf{mmmm} \rangle$ respectively, a more accurate closure rule may be devised. The derivation of this new rule is the focus of this chapter, and it will be referred to as the DQ closure rule (DQ).

The four closure rules being utilized are the Doi (DOI) [19], Tsuji-Rey (TR) [3], Hinch-Leal 1 (HL1) and Hinch-Leal 2 (HL2) closure rules [22]. The four closure schemes are given in Table I in terms of $\mathbf{A}$, where $\mathbf{A}$ is any traceless symmetric second order tensor. They will be referred to by their abbreviations for the remainder of this paper. A few characteristics of the closures rules should be noted. The Doi closure rule is by far the simplest rule to implement, both analytically and numerically, as it contains the least number of terms [2]. It is also a component of the other three closure rules. The Tsuji and Rey closure rule is written in terms of $\mathbf{A} : \mathbf{Q}_4$, where $\mathbf{A}$ is any traceless symmetric second order tensor and $\mathbf{Q}_4$ is the fourth rank order tensor parameter related to $\mathbf{Q}$ [3]. For the purpose of the DQ closure rule, the component rules are written in terms of $\mathbf{A} : \langle \mathbf{mmmm} \rangle$ [13]. The Hinch-Leal closures are designed to match the exact solution of the kinetic equation under equilibrium conditions (in the absence of flow). Therefore, many of the coefficients in the terms are found through interpolation or other *ad hoc* methods [22]. Also, note the appearance of the exponential terms in the HL2 closure. This term makes the analytical study of the HL2 closure and the proposed DQ closure challenging in many cases and not feasible in others.

TABLE I: Closure rules for approximating $\mathbf{Q} : \langle \mathbf{mmmm} \rangle$

Rule	$\mathbf{A} : \langle \mathbf{mmmm} \rangle \approx$
DOI:	$(\mathbf{A} : \mathbf{M})\,\mathbf{M}$
TR:	$\frac{1}{4}[(\mathbf{A}\colon \mathbf{M})\mathbf{M} + \mathbf{A}\cdot\mathbf{M}\cdot\mathbf{M} + \mathbf{M}\cdot\mathbf{A}\cdot\mathbf{M} + \mathbf{M}^2\cdot\mathbf{A} - (\mathbf{M}^2\colon \mathbf{A})\mathbf{I}] + \frac{1}{3}\mathbf{A}\colon \mathbf{MI}$
HL1:	$\frac{1}{5}\Big[6\mathrm{M}\cdot\mathbf{A}\cdot\mathbf{M} - \mathbf{M}\,(\mathbf{A}\colon \mathbf{M}) - 2\,((\mathbf{MM}) : \mathbf{A})\,\mathbf{I} + 2\mathrm{M} : \mathbf{AI}\Big]$
HL2:	$\mathbf{M}\,(\mathbf{M}\colon \mathbf{A}) + 2\,[\mathbf{M}\cdot\mathbf{A}\cdot\mathbf{M} - \mathbf{M}^2\,(\mathbf{M}^2\colon \mathbf{A})\,/\,(\mathbf{I} : \mathbf{M}^2)]$
	$+\alpha\left[\frac{52}{315}\mathbf{A} - \frac{8}{21}\left(\mathbf{A}\cdot\mathbf{M} + \mathbf{M}\cdot\mathbf{A} - \frac{2}{3}\,(\mathbf{M}\colon \mathbf{A})\,\mathbf{I}\right)\right]$
	where $\alpha = exp\,[2\,(1 - 3\mathbf{M}^2 : \mathbf{I})\,/\,(1 - \mathbf{M}^2 : \mathbf{I})]$.

The DQ closure rule states:

$$\begin{aligned} \mathbf{D} : \langle \mathbf{mmmm} \rangle &\approx x_1\mathbf{DOI} + x_2\mathbf{TR} + x_3\mathbf{HL1} + x_4\mathbf{HL2} \\ \mathbf{Q} : \langle \mathbf{mmmm} \rangle &\approx x_5\mathbf{DOI} + x_6\mathbf{TR} + x_7\mathbf{HL1} + x_8\mathbf{HL2} \end{aligned} \tag{13}$$

where $x_1, ..., x_8$ are coefficients which minimize the error of the respective closure rule. General least squares curve fitting is utilized to find these eight coefficients.

II.2.1 The Application of General Least Squares

General least squares can be applied to curve fitting a set of data points in the following manner [26,27]. For an $m \times n$ matrix $\mathbf{A}$ and a vector $\mathbf{b}$, the residual r can be expressed as $r = r(\mathbf{x}) = \mathbf{Ax} - \mathbf{b}$. The general least squares problems is to find a vector $\mathbf{x}$ that minimizes the quantity

$$\sum_{i=1}^{m} r_i^2 = ||r||_2^2 = ||\mathbf{Ax} - \mathbf{b}||^2 = (\mathbf{Ax} - \mathbf{b})^T\,(\mathbf{Ax} - \mathbf{b})\,. \tag{14}$$

From (14), the set of solutions $\mathbf{x}$ which minimizes $||r||_2$ can be found from

$$\mathbf{A^T A x} = \mathbf{A^T b}. \tag{15}$$

Solving for $\mathbf{x}$ yields the matrix equation

$$\mathbf{x} = \left(\mathbf{A}^{\mathbf{T}}\mathbf{A}\right)^{-1}\left(\mathbf{A}^{\mathbf{T}}\mathbf{b}\right). \tag{16}$$

From the DQ closure rule (13), define

$$\mathbf{A} = \begin{pmatrix} DOI_1 & TR_1 & HL1_1 & HL2_1 \\ DOI_2 & TR_2 & HL3_1 & HL2_3 \\ \vdots & \vdots & \vdots & \vdots \\ DOI_m & TR_m & HL1_m & HL2_m \end{pmatrix}, \mathbf{b} = \begin{pmatrix} y_1 \\ y_2 \\ \vdots \\ y_m \end{pmatrix}, \mathbf{x} = \begin{pmatrix} x_1 \\ x_2 \\ x_3 \\ x_4 \end{pmatrix},$$

where y_i, $i = 1, 2, ..., m$, is the actual value of $\mathbf{D} : \langle\mathbf{mmmm}\rangle$ calculated from the kinetic simulations, and DOI_i, TR_i, HL1_i, and HL2_i are approximations to that tensor contraction calculated from the corresponding closure rules. By solving (16), the coefficients $x_1, ..., x_4$ can be found. Similarly, to find $x_5, ..., x_8$, y_i would be the actual value of $\mathbf{Q} : \langle\mathbf{mmmm}\rangle$. Given that the process to solve for $x_1, ..., x_4$ and $x_5, ..., x_8$ are the same, the remainder of this section will focus only on how $x_1, ..., x_4$ are found. The results from the least squares fit for both sets of coefficients will be discussed in the next section.

II.2.2 Solving the System of Equations

In order to solve for the coefficients $x_1 ... x_4$, AUTO bifurcation software [28] is used to generate the data needed to calculate $\mathbf{b}$, the y_i values. Consider the PDF

$$\begin{aligned} f(\mathbf{m}, t) &= \sum_{l=0}^{L} \sum_{m=-l}^{l} a_{lm}(t) Y_l^m(\theta, \phi) \\ Y_l^m(\theta, \phi) &= P_l^m(\cos\theta) e^{\imath m\phi} \end{aligned} \tag{17}$$

where Y_l^m are complex spherical harmonic expansions and P_l^m are normalized Legendre polynomials for l even; $\mathbf{m}$ is a representation of the molecule axis in spherical coordinates (a vector on the unit sphere with polar angle θ and azimuthal angle ϕ); and L is the order of truncation in the Galerkin method [8]. Through the use of this spherical harmonic expansion (17), Forest, Zhou, and Wang were able to derive a system of fifteen explicit equations for $\langle\mathbf{mmmm}\rangle$ in terms of fourteen independent a_{lm} components [14], as well as a system of five explicit equations for $\mathbf{Q}$ in terms of five independent a_{lm} components [23]. When implemented in AUTO, the kinetic equation is solved using a system of equations with 65 components corresponding to the truncation $L = 10$ [8,14,23]. By post-processing the data files from AUTO in MATLAB, values for $\mathbf{Q}$ and $\langle\mathbf{mmmm}\rangle$ can be obtained. Using those values, $\mathbf{D} : \langle\mathbf{mmmm}\rangle$ and $\mathbf{Q} : \langle\mathbf{mmmm}\rangle$ can be computed from the kinetic simulation. Recall from (4), $\mathbf{D}$ is known and its value is completely dependent on the Peclet number. Finally, by using the same $\mathbf{Q}$ values, the approximations for $\mathbf{D} : \langle\mathbf{mmmm}\rangle$ and $\mathbf{Q} : \langle\mathbf{mmmm}\rangle$ from each of the pre-existing closure rules (DOI, TR, HL1, and HL2) can be calculated. Note, for each kinetic solution for $\mathbf{D} : \langle\mathbf{mmmm}\rangle$ and $\mathbf{Q} : \langle\mathbf{mmmm}\rangle$ calculated for a given $\mathbf{Q}$, there are four corresponding approximations to the contraction, one for each closure scheme.

AUTO is run for a variety of N and Pe values. For each run of AUTO, Pe is set to a predetermined constant ranging from 0.1 to 10.0, reflecting both weaker and stronger shear flow. The geometry parameter is set to $a = 1.0$ for all computations in this study, representing large aspect ratio rod-like liquid crystalline polymers as per (5) and Fig. 2. Recall in (4) it was shown that for the case of simple shear flow, $\mathbf{D}$ and $\boldsymbol{\Omega}$ depend solely on the value of the Peclet number Pe. N varies during each run of AUTO between 0.0 and 8.0. The data generated from each run of AUTO is combined into a single large data file with 47,497 entries for different combinations of N and Pe, including all stable and unstable steady solutions. The data set is used to calculate accurate values of $\mathbf{D} : \langle\mathbf{mmmm}\rangle$ and $\mathbf{Q} : \langle\mathbf{mmmm}\rangle$, as well as the approximations for $\mathbf{D} : \langle\mathbf{mmmm}\rangle$ and $\mathbf{Q} : \langle\mathbf{mmmm}\rangle$ from each of the preexisting closure rules (DOI, TR, HL1, and HL2). Then the coefficient sets $x_1, ..., x_4$ and $x_5, ..., x_8$, are each found from a single least squares fit. Table II lists the values of the coefficients for $0 < Pe <= 10$.

TABLE II: Coefficients from the least squares data fit

DOI	TR	HL1	HL2	Simple Sum	Weighted Sum
x_1	x_2	x_3	x_4		
-0.09873244	0.30939743	0.67545960	0.03690273	0.92302731	1.00037667
x_5	x_6	x_7	x_8		
-0.02891184	0.17859696	0.19104295	0.62051140	0.96123947	1.00588871

The values for $x_1...x_4$ and $x_5...x_8$, respectively, are averaged over the range of Pe and then summed in two different ways. A simple sum and a weighted sum (ws).

Each closure rule should satisfy the condition $tr\left(\mathbf{A} : \langle\mathbf{mmmm}\rangle\right) = \mathbf{A} : \mathbf{M}$, where A is a second moment tensor. DOI, HL1, and HL2 closure rules fulfill the condition, while the TR closure rule does not. For TR, $tr\left(\mathbf{D} : \langle\mathbf{mmmm}\rangle\right) = 1.25\left(\mathbf{D} : \mathbf{M}\right)$, and similarly $tr\left(\mathbf{Q} : \langle\mathbf{mmmm}\rangle\right) = 1.25\left(\mathbf{Q} : \mathbf{M}\right)$. A detailed analysis of the trace of each closure rule can be found in the Appendix. The weighted sum takes this into account and is expanded as $x_1 + 1.25x_2 + x_3 + x_4$. The new closure rule is a linear combination of the other four rules, therefore the coefficients' sum should equal 1 for the condition $tr\left(\mathbf{Q} : \langle\mathbf{mmmm}\rangle\right) = \mathbf{Q} : \mathbf{M}$ to be satisfied. Note, that the weighted sum does not equal one, but it is relatively close to one. Given that this was a numerical fit, the results are being considered acceptable and these coefficients are used for evaluating the performance of the DQ closure rule.

II.3 STATEMENT OF THE DQ CLOSURE RULE

Notice that many of the terms in the DOI, TR, HL1, and HL2 closure schemes repeat. By combining like terms, the proposed closure rule can be simplified. The DQ closure is stated below:

$$\begin{aligned}\mathbf{D} : \langle\mathbf{mmmm}\rangle \approx{} & -0.1196\left(\mathbf{D} : \mathbf{M}\right)\mathbf{M} + 0.9617(\mathbf{M}\cdot\mathbf{D}\cdot\mathbf{M}) \\ & +0.0773(\mathbf{M}\cdot\mathbf{M}\cdot\mathbf{D} + \mathbf{D}\cdot\mathbf{M}\cdot\mathbf{M}) - 0.3475\left(\mathbf{D}\colon \mathbf{M}^2\right)\mathbf{I} \\ & +0.3733\left(\mathbf{D}\colon \mathbf{M}\right)\mathbf{I} + 0.0369\Big(-2\left(\mathbf{D}\colon \mathbf{M}^2\right)\mathbf{M}^2/\left(\mathbf{I}\colon \mathbf{M}^2\right) \\ & +\alpha\left[\frac{52}{315}\mathbf{D} - \frac{8}{21}(\mathbf{DM}+\mathbf{MD}) + \frac{16}{63}\left(\mathbf{D}\colon \mathbf{M}\right)\mathbf{I}\right]\Big)\end{aligned} \tag{18}$$

$$\begin{aligned}\mathbf{Q} : \langle\mathbf{mmmm}\rangle \approx{} & 0.5980\left(\mathbf{Q} : \mathbf{M}\right)\mathbf{M} + 1.6042(\mathbf{M}\cdot\mathbf{Q}\cdot\mathbf{M}) \\ & -0.1211\left(\mathbf{Q}\colon \mathbf{M}^2\right)\mathbf{I} + 0.1359\left(\mathbf{Q}\colon \mathbf{M}\right)\mathbf{I} \\ & +0.6205\Big(-2\left(\mathbf{Q}\colon \mathbf{M}^2\right)\mathbf{M}^2/\left(\mathbf{I}\colon \mathbf{M}^2\right) \\ & +\alpha\left[\frac{52}{315}\mathbf{Q} - \frac{16}{21}\mathbf{QM} + \frac{16}{63}\left(\mathbf{Q}\colon \mathbf{M}\right)\mathbf{I}\right]\Big)\end{aligned} \tag{19}$$

where $\mathbf{M}\cdot\mathbf{Q}\cdot\mathbf{M} = \mathbf{M}\cdot\mathbf{M}\cdot\mathbf{Q} = \mathbf{Q}\cdot\mathbf{M}\cdot\mathbf{M}$ and $\mathbf{M}\cdot\mathbf{Q} = \mathbf{Q}\cdot\mathbf{M}$. The same equalities do not hold for the case of $\mathbf{D} : \langle\mathbf{mmmm}\rangle$.

In addition to doing a single least squares fit on the data generated from these four existing closure rules, several other approaches were made to design a new closure rule. Originally, the data files were arranged according to the Peclet number, and $x_1, ..., x_8$ were found at each value of Pe. The values of $x_1, ..., x_8$ were then averaged to determine the values of the coefficients for the new closure rule. Alternatively, multiple attempts were made at fitting the common terms listed in the the pre-existing closure rules directly, as opposed to fitting the closure rules and then combining the common terms as was done above. However, the variance in all of these approaches was calculated and found to be the smallest for the single least squares fit of the DQ closure rule. Multiple other metrics were used in determining which approach yielded the most acceptable results, the clear favorite being the single least squares fit from the four existing closure.

CHAPTER III

BIFURCATION DIAGRAMS IN (N, s) SPACE IN EQUILIBRIUM

In this chapter, the proposed DQ closure is examined under equilibrium, or no flow, conditions. The second moment equation is written in terms of its major director and a single order parameter. By substituting this equivalent form of $\mathbf{Q}$ into the dimensionless dynamic equation (9), the bifurcation diagrams at equilibrium for each of the four existing closure rules and the new proposed closure rule can be constructed. From its bifurcation diagram, the isotropic and nematic flow phases and transitions of the proposed DQ closure are examined in detail. In addition, the critical bifurcations from the equilibrium diagrams of the five closure rules are compared with each other, as well as to the known solution of the kinetic equation [8–11, 21].

III.1 EQUATION OF THE ORDER PARAMETER

The following lemmas are straightforward, and will be used frequently.

Lemma III.1.1 *Let* $\mathbf{A}$, $\mathbf{B}$, $\mathbf{C}$, *and* $\mathbf{D}$ *be second order symmetric tensors. Suppose that* $\mathbf{B} = \mathbf{C} + \mathbf{D}$. *Then* $\mathbf{A} : \mathbf{B} = \mathbf{A} : \mathbf{C} + \mathbf{A} : \mathbf{D}$.

Lemma III.1.2 *Let* $\mathbf{A}$ *and* $\mathbf{B}$ *be second order symmetric tensors. Then* $\mathbf{A} : \mathbf{B} = tr(\mathbf{A} \cdot \mathbf{B})$.

Recall from the earlier description of Doi kinetic theory that $\mathbf{M}$ and $\mathbf{Q}$ share an orthonormal frame of eigenvectors, referred to as directors, $\mathbf{n}_i, i = 1, 2, 3$, with $\mathbf{M}$ having corresponding ordered eigenvalues, $d_i, i = 1, 2, 3$. At equilibrium, the material must be either uniaxial, meaning exactly two of the eigenvalues must be equal, $d_i = d_j \neq d_k$, or isotropic, wherein in all three eigenvalues are the same, $d_1 = d_2 = d_3$ [8, 13]. For the case of simple shear flow at equilibrium, $\beta = 0$ in (12) and so $s = d_1 - d_3$ is now the single order parameter where d_1 corresponds to the unique major director $\mathbf{n}_1$ [8, 13]. Using the harmonic expansions for the second-moment $\mathbf{M}$, the second-moment orientation tensor $\mathbf{Q}$, and the dimensionless dynamic equation for $\mathbf{Q}$, the bifurcation diagrams at equilibrium can be given in terms of the order parameter, s, and the nematic concentration, N.

The major director $\mathbf{n}$ is defined as

$$\mathbf{n} = \begin{pmatrix} \sin\theta\cos\phi \\ \sin\theta\sin\phi \\ \cos\theta \end{pmatrix}, \tag{20}$$

in spherical coordinates, where

$$\mathbf{nn} = \begin{pmatrix} \sin^2\theta\cos^2\phi & \sin^2\theta\sin\phi\cos\phi & \sin\theta\cos\theta\cos\phi \\ \sin^2\theta\sin\phi\cos\phi & \sin^2\theta\sin^2\phi & \sin\theta\cos\theta\sin\phi \\ \sin\theta\cos\theta\cos\phi & \sin\theta\cos\theta\sin\phi & cos^2\theta \end{pmatrix}, \tag{21}$$

$$\mathbf{nn} = \mathbf{nn}^{\mathbf{T}}, \quad \mathbf{nn} : \mathbf{nn} = \mathbf{n}^{\mathbf{T}}\mathbf{n} = 1. \tag{22}$$

θ is the polar angle measured from the vorticity (z) axis and ϕ is the latitude angle in the shear (x-y) plane. ϕ is measured counter-clockwise from the positive flow direction (x); y is the flow gradient direction [8]. From the values of θ and ϕ, the type of flow can be determined. Flow regimes will be explained in detail in the following chapters. In equilibrium, the second moment equation (8) can be written in terms of the major director $\mathbf{n}$ (20) and the order parameter s (12) [8, 10, 11, 13]:

$$\mathbf{Q} = s\left(\mathbf{nn} - \frac{1}{3}\mathbf{I}\right) = s\left(\mathbf{nn}^{\mathbf{T}} - \frac{1}{3}\mathbf{I}\right). \tag{23}$$

Subsequently, s can be found from (23) in terms of $\mathbf{n}$ and $\mathbf{Q}$ by applying Lemma III.1.1 and the identity $\mathbf{nn} : \mathbf{nn} = 1$.

$$\mathbf{Q} : \mathbf{nn} = \frac{2}{3}s \tag{24}$$

Similarly,

$$\mathbf{Q}^2 = s^2\left(\frac{1}{3}\mathbf{nn} + \frac{1}{9}\mathbf{I}\right), \tag{25}$$

$$\mathbf{Q}^2 : \mathbf{nn} = \frac{4}{9}s^2. \tag{26}$$

At equilibrium there is no flow, $Pe = 0$, therefore the dimensionless dynamic equation (9) simplifies to

$$\frac{\partial\mathbf{Q}}{\partial t} = -\mathbf{Q} + N\left(\mathbf{Q} + \frac{1}{3}\mathbf{I}\right)\cdot\mathbf{Q} - N\mathbf{Q} : \langle\mathbf{mmmm}\rangle \tag{27}$$

for $\Lambda = 1$, the usual approximation to D_r^{-1}. Additionally, at equilibrium $\frac{\partial \mathbf{Q}}{\partial t} = 0$.

The last term in (27) introduces a fourth order tensor to the equation, thus the system is not closed. The approximation of $\mathbf{Q} : \langle \mathbf{mmmm} \rangle$ by various closure rules will be addressed in the next sections. Contracting (27) with $\mathbf{nn}$ (or multiplying by $\mathbf{n}^T$ from the left and $\mathbf{n}$ from the right) and having $\frac{\partial \mathbf{Q}}{\partial t} = 0$, (27) will be written in terms of the order parameter s and concentration N. The expressions needed for the DQ closure scheme's equilibrium equation are derived below, and the basic process by which the schemes are written in terms of s is discussed.

At the end of the chapter, the resulting functions are graphed, showing their bifurcation points under equilibrium conditions. The bifurcation diagrams of the existing four closure rules are compared to the proposed DQ closure rule and the location of critical bifurcation points is examined.

III.2 THE DQ CLOSURE RULE AT EQUILIBRIUM

III.2.1 Relations between s and N in DQ closure

Recall the proposed DQ closure rule for the $\mathbf{Q} : \langle \mathbf{mmmm} \rangle$ contraction:

$$\begin{aligned} \mathbf{Q} : \langle \mathbf{mmmm} \rangle \approx{}& 0.5980\,(\mathbf{Q} : \mathbf{M})\,\mathbf{M} + 1.6042(\mathbf{M} \cdot \mathbf{Q} \cdot \mathbf{M}) \\ & -0.1211\left(\mathbf{Q} \colon \mathbf{M}^2\right)\mathbf{I} + 0.1359\,(\mathbf{Q} \colon \mathbf{M})\,\mathbf{I} \\ +0.6205\Bigg(\left(\mathbf{Q} \colon \mathbf{M}^2\right)\mathbf{M}^2/\left(\mathbf{I} \colon \mathbf{M}^2\right) &+ \alpha\left[\frac{52}{315}\mathbf{Q} - \frac{16}{21}\mathbf{QM} + \frac{16}{63}\,(\mathbf{Q} \colon \mathbf{M})\,\mathbf{I}\right]\Bigg) \qquad (28) \\ \alpha ={}& exp\left[2\left(1 - 3\mathbf{M}^2 : \mathbf{I}\right)/\left(1 - \mathbf{M}^2 : \mathbf{I}\right)\right] \end{aligned}$$

Recall some of the basic properties of $\mathbf{Q}$ and $\mathbf{M}$ that will be of use in the derivation:

$$\mathbf{Q} = \mathbf{M} - \frac{1}{3}\mathbf{I}, \quad tr(\mathbf{M}) = 1, \quad tr(\mathbf{Q}) = 0. \qquad (29)$$

Using (23), (26), and (29), and Lemmas III.1.1 and III.1.2, the DQ closure rule can be derived in terms of s.

$$\mathbf{Q} \colon \mathbf{M} = tr(\mathbf{Q} \cdot \mathbf{Q}) + \frac{1}{3}tr(\mathbf{Q} \cdot \mathbf{I}) = \frac{2}{3}s^2, \qquad (30)$$

giving

$$\begin{aligned}(\mathbf{Q}:\mathbf{M})\,\mathbf{M} &= \frac{2}{3}s^2\left(\mathbf{Q}+\frac{1}{3}\mathbf{I}\right)\\ &= \frac{2}{3}s^3\mathbf{nn}-\frac{2}{9}s^3\mathbf{I}+\frac{2}{9}s^2\mathbf{I}.\end{aligned} \tag{31}$$

$$\begin{aligned}\mathbf{Q}\cdot\mathbf{M}\cdot\mathbf{M} &= \left[\frac{1}{3}s^2\left(\mathbf{nn}+\frac{1}{3}\mathbf{I}\right)+\frac{1}{3}\left(\mathbf{nn}-\frac{1}{3}\mathbf{I}\right)\right]\left[s\left(\mathbf{nn}-\frac{1}{3}\mathbf{I}\right)+\frac{1}{3}\mathbf{I}\right]\\ &= \frac{1}{3}s^3\left(\mathbf{nn}-\frac{1}{9}\mathbf{I}\right)+\frac{2}{9}s^2\left(\mathbf{nn}+\frac{1}{3}\mathbf{I}\right)+\frac{1}{9}s\left(\mathbf{nn}-\frac{1}{3}\mathbf{I}\right).\end{aligned} \tag{32}$$

$$\mathbf{Q}:(\mathbf{MM}) = tr(\mathbf{Q}\cdot\mathbf{M}\cdot\mathbf{M}) = \frac{2}{9}s^3+\frac{4}{9}s^2. \tag{33}$$

Note, $\mathbf{M}\cdot\mathbf{Q} = \left(\mathbf{Q}+\frac{1}{3}\mathbf{I}\right)\mathbf{Q} = \mathbf{Q}\left(\mathbf{Q}+\frac{1}{3}\mathbf{I}\right) = \mathbf{Q}\cdot\mathbf{M}$, and similarly

$$\mathbf{Q}\cdot\mathbf{M}\cdot\mathbf{M} = \mathbf{M}\cdot\mathbf{Q}\cdot\mathbf{M} = \mathbf{M}\cdot\mathbf{M}\cdot\mathbf{Q}. \tag{34}$$

The only term left to put in terms of s and N is $\mathbf{I}:\mathbf{M}^2$. By applying Lemma III.1.2 it simplifies to

$$\mathbf{I}:\mathbf{M}^2 = tr(\mathbf{M}^2) = \frac{2}{3}s^2+\frac{1}{3}. \tag{35}$$

Substituting (30), (31), (33), (32), and (35) into the DQ closure rule (28) gives an expression for the $\mathbf{Q}:\langle\mathbf{mmmm}\rangle$ in terms of s and N. Recall $tr(\mathbf{nn}) = 1$. On contracting this equivalent form of (28) by $\mathbf{nn}$, the result is an implicit function of s with respect to N.

$$\begin{aligned}0 &= -\frac{2}{3}+N\Bigg[-0.7142s^2-0.2006s+0.1034\\ &+ 0.6205\Big(6s\Big(\frac{8}{81}s^3+\frac{8}{27}s^2+\frac{2}{9}s+\frac{4}{81}\Big)/\Big(1+2s^2\Big)+\alpha\Big(\frac{32}{189}s+\frac{8}{135}\Big)\Big)\Bigg]\\ \alpha &= exp\left[-6s^2/\left(1-s^2\right)\right]\end{aligned} \tag{36}$$

Due to the exponential term, an analytic expression for $s = s(N)$ cannot be determined. However, a graphical solution can be found by using an implicit numerical solver.

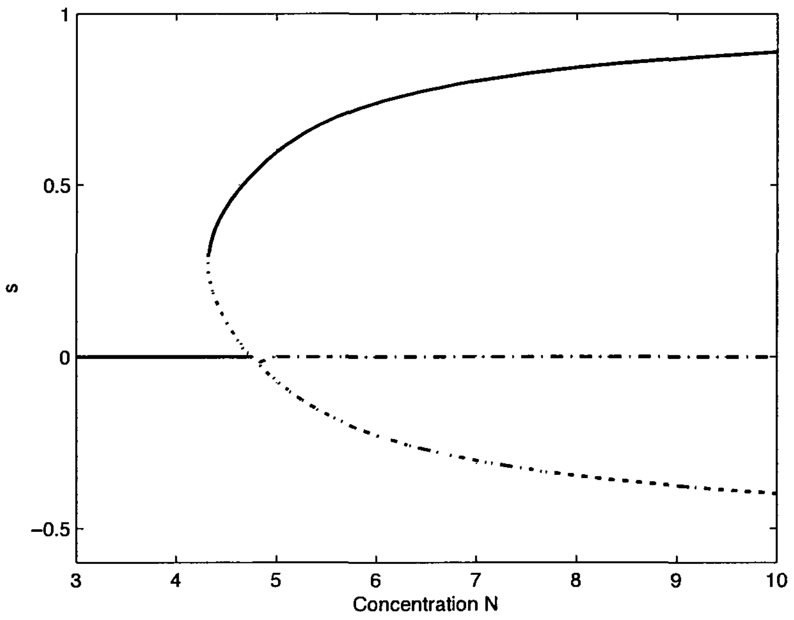

FIG. 3: Bifurcation diagram for the DQ closure rule under equilibrium conditions. The solid lines indicate the stable solutions; the dashed lines indicate the unstable solutions.

\

III.2.2 Equilibrium bifurcation diagram

When $Pe = 0$, there is no flow and thus there is no external field for ordering the anisotropic states. This means that the major director has no preferred orientation in the nematic phase; it can be oriented in any direction. By solving $s(N)$ graphically for (36), in accordance with Bhave's study of the kinetic equation [21], the equilibrium bifurcation diagram for the DQ closure scheme is given in Fig. 3. From the study of the kinetic equation at equilibrium, much is known about the phase transitions of nematic liquid crystalline polymers [8–10, 21].

The order parameter for the kinetic equation at equilibrium, as well as the DQ closure (see Fig. 3), falls into the range of $-\frac{1}{2} < s < 1$. Recall from the discussions of Doi kinetic theory and the equation of the order parameter (12), s is defined in terms of the eigenvalues, d_i, $i = 1, 2, 3$. For $s < 0$, the system exhibits unstable oblate uniaxial symmetry ($d_i = d_j \neq d_k$) wherein the molecular axes $\mathbf{m}$ are aligned in planes at angle to the director axis. For $s = 0$, the system is in its isotropic base state ($d_k < d_i = d_j$). For $s > 0$ the system exhibits prolate uniaxial symmetry

($d_i > d_j = d_k$) wherein the molecular axes $\mathbf{m}$ are aligned about the director axis. At the upper limit of the order parameter, $s = 1$, the nematic is stable and perfect alignment of the molecular axes $\mathbf{m}$ about the director axis is achieved. At the lower limit, $s = -\frac{1}{2}$, the nematic is unstable and all molecules lie randomly in planes orthogonal to the director axis [13, 21].

There are two critical bifurcation points from the isotropic base state $s = 0$. From Fig. 3, one can clearly see the bifurcation at $s = 0$ when $N = 4.76$. Here there is a phase transition from the stable isotropic phase for $N < 4.76$ to the unstable isotropic phase for $N > 4.76$. Additionally at the point $s = 0, N = 4.76$, the isotropic, $s = 0$, branch crosses with the nematic, $s \neq 0$, branch. The unstable prolate phase and stable isotropic phase collide and an unstable oblate phase emerges for s negative. For $0 < s < 0.275$ and $4.32 < N < 4.76$, the system is in its unstable prolate phase, or moderately aligned prolate phase. The second critical bifurcation point is at $s = 0.275$ and $N = 4.32$. Here a second order isotropic-nematic phase transition occurs and the stable prolate phase is born. Between $4.32 \leq N \leq 4.76$, the system is both isotropic and nematic stable (bistable). With a decrease in concentration, the stable nematic state becomes a stable isotropic state at $N = 4.32$; with an increase in concentration, the stable isotropic state becomes a stable nematic state at $N = 4.76$. As $s \to 1$, the system is in its highly aligned stable prolate phase [8–10, 21].

III.3 EXISTING CLOSURE SCHEMES

The equilibrium equations for the existing closure schemes are well known [10, 11]. The relation between order parameter s and concentration N at equilibrium are given below. By applying the substitutions for the $\mathbf{Q}$ and $\mathbf{M}$ terms given in the previous section, one can easily derive the expressions for the following expressions.

Recall the Doi closure rule:

$$\mathbf{Q} : \langle \mathbf{mmmm} \rangle \approx (\mathbf{Q} : \mathbf{M})\, \mathbf{M}. \tag{37}$$

(27) can be written in terms of s and N as

$$\frac{\partial s}{\partial t} = -\frac{2}{3} + N \left[-\frac{4}{9} s^2 + \frac{2}{9} s + \frac{2}{9} \right] = 0, \tag{38}$$

giving

$$s(N) = \frac{1 \pm 3\sqrt{1 - \frac{8}{3N}}}{4}. \tag{39}$$

Recall the Tsuji-Rey (TR) closure rule:

$$\begin{aligned}\mathbf{Q}:\langle\mathbf{mmmm}\rangle &\approx \frac{1}{4}\Big[(\mathbf{Q}:\mathbf{M})\,\mathbf{M}+\mathbf{Q}\cdot\mathbf{M}\cdot\mathbf{M}+\mathbf{M}\cdot\mathbf{Q}\cdot\mathbf{M}\\ &\quad +\mathbf{M}^2\cdot\mathbf{Q}-\left(\mathbf{M}^2:\mathbf{Q}\right)\mathbf{I}\Big]+\frac{1}{3}\mathbf{Q}:\mathbf{MI}\end{aligned}\tag{40}$$

$\frac{\partial s}{\partial t}$ can be expressed in terms of the TR closure rule as

$$\frac{\partial s}{\partial t}=-\frac{2}{3}+N\left[-\frac{5}{18}s^2+\frac{1}{18}s+\frac{3}{18}\right]=0,\tag{41}$$

giving

$$s(N)=\frac{1\pm\sqrt{61-\frac{240}{N}}}{10}.\tag{42}$$

The Hinch-Leal (HL1) closure rule for weak Brownian motion is

$$\begin{aligned}\mathbf{Q}:\langle\mathbf{mmmm}\rangle &\approx \frac{1}{5}\Big[6\mathbf{M}\cdot\mathbf{Q}\cdot\mathbf{M}-\mathbf{M}\,(\mathbf{Q}:\mathbf{M})\\ &\quad -2\left((\mathbf{MM}):\mathbf{Q}\right)\mathbf{I}+2\mathbf{M}:\mathbf{QI}\Big].\end{aligned}\tag{43}$$

$\frac{\partial s}{\partial t}$ can be written in terms of the HL1 closure rule as

$$\frac{\partial s}{\partial t}=-\frac{2}{3}+N\left[-\frac{8}{45}s^2+\frac{2}{45}s+\frac{6}{45}\right]=0,\tag{44}$$

giving

$$s(N)=\frac{1\pm\sqrt{1-\frac{240}{49N}}}{8}.\tag{45}$$

The Hinch-Leal (HL2) closure rule for strong Brownian motion is

$$\begin{aligned}\mathbf{Q}:\langle\mathbf{mmmm}\rangle &\approx \mathbf{M}\,(\mathbf{M}:\mathbf{Q})+2\left[\mathbf{M}\cdot\mathbf{Q}\cdot\mathbf{M}-\mathbf{M}^2\left(\mathbf{M}^2:\mathbf{Q}\right)/\left(\mathbf{I}:\mathbf{M}^2\right)\right]\\ &\quad +\alpha\left[\frac{52}{315}\mathbf{Q}-\frac{8}{21}\left(\mathbf{Q}\cdot\mathbf{M}+\mathbf{M}\cdot\mathbf{Q}-\frac{2}{3}\,(\mathbf{M}:\mathbf{Q})\,\mathbf{I}\right)\right]\\ \alpha &= exp\left[2\left(1-3\mathbf{M}^2:\mathbf{I}\right)/\left(1-\mathbf{M}^2:\mathbf{I}\right)\right]\end{aligned}\tag{46}$$

$\frac{\partial s}{\partial t}$ in terms of the HL2 closure rule is

$$\begin{aligned}\frac{\partial s}{\partial t} &= -\frac{2}{3}+N\Bigg[-\frac{4}{27}s^2-\frac{10}{27}s+\frac{2}{27}\\ &\quad -6s\left(\frac{8}{81}s^3+\frac{8}{27}s^2+\frac{2}{9}s+\frac{4}{81}\right)/\left(1+2s^2\right)+\alpha\left(\frac{32}{189}s+\frac{8}{135}\right)\Bigg]\\ &= 0\\ \alpha &= exp\left[-6s^2/\left(1-s^2\right)\right],\end{aligned}\tag{47}$$

which can only be solved implicitly due to the exponential term.

III.4 GRAPHICAL COMPARISON OF CLOSURE RULES

Substituting the closure rule derivations for the approximation of $\mathbf{Q} : \langle \mathbf{mmmm} \rangle$ into (27) results in the five closed equations (36), (38), (41), (44), and (47). These are graphed in MATLAB using an implicit graphing tool [29], yielding the bifurcation diagrams for each closure rule at equilibrium. From the kinetic equation, it is known that the equilibrium solution has critical bifurcation points at $N = 4.49$ and $N = 5.0$ [8, 10]. $N = 4.49$ is a saddle-node bifurcation point [8]; it is located at the vertex of the parabola-like shape and indicates the transition from unstable to stable states as well as the birth of the nematic phases for $N > 4.49$ and $s \neq 0$. $N = 5.0$ is a transcritical bifurcation point [9] that is located at the s-intercept of the parabola-like shape; for the line $s = 0$, it indicates the change from the stable isotropic phase to the unstable isotropic phase for all values of $N > 5.0$.

TABLE III: Polymer Concentration Value (N) at Critical Points in Equilibrium

Closure	DOI	TR	HL1	HL2	DQ
saddle-node bifurcation	2.67	3.93	4.90	4.38	4.32
transcritical bifurcation (s=0)	3.0	4.0	5.0	5.0	4.76

The purpose of a closure rule is to simplify the analysis and computation, while also capturing the right physical phenomenon of the liquid crystalline polymers. Thus it is desirable for the graph of the new proposed DQ closure rule to have a saddle-node bifurcation and transcritical bifurcation at these two critical points, or at least be closer to them than the existing closure rules. Table III lists the values of the polymer concentration N at the saddle-node and transcritical bifurcation points for each closure depicted in Fig. 4. Each closure rule shares the same isotropic-nematic phase transition features, at the vertex of the parabola-like shape of their respective bifurcation diagrams in Fig. 4, as those described in Fig. 3 for the DQ closure rule. From inspection of these equilibrium bifurcation diagrams and the corresponding table, it can be concluded that the HL2 closure rule artificially has the exact transcritical bifurcation point value as the kinetic equation, as well as the saddle-node bifurcation point which is closest to that of the kinetic equation. However, the new proposed DQ closure out performs the other three closure rules in comparing these two critical points. A shift parameter can be used to ensure the

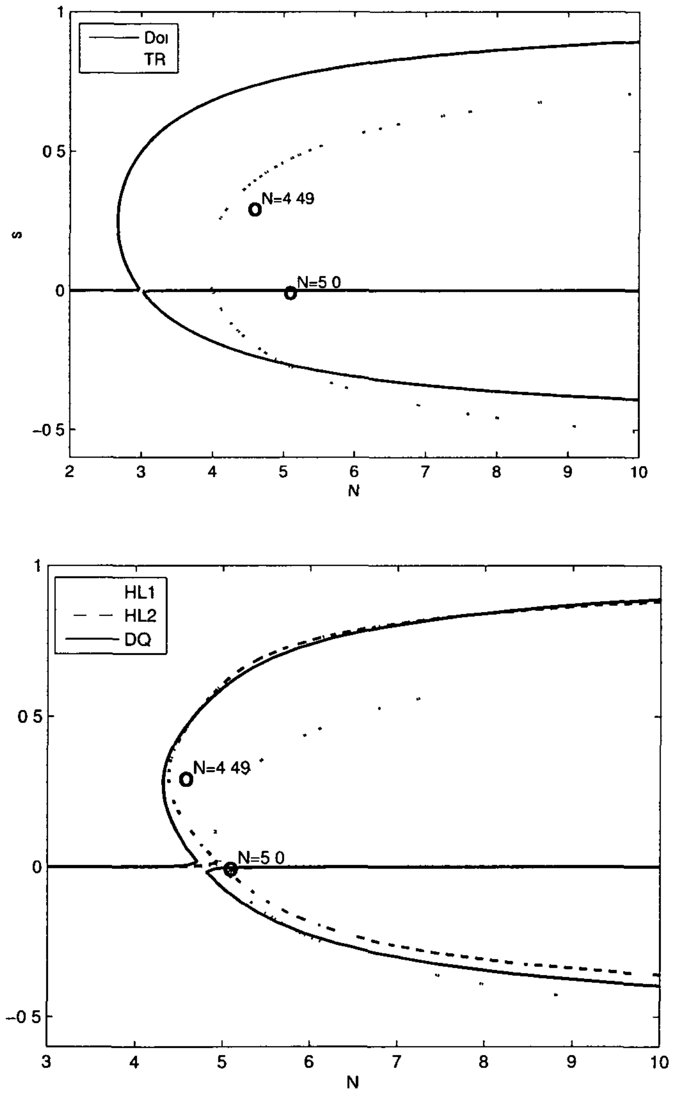

FIG. 4: Comparison of the closure rules at equilibrium. N=5.0 is a transcritical bifurcation point and N=4.49 is a saddle-node bifurcation point from the kinetic solution. Top: DOI and TR closures. Bottom: HL1, HL2, and DQ closures.

DQ closure has the exact bifurcation points of the kinetic equation [16], but that is artificial. The HL1 closure rule also yields the identical transcritical bifurcation point as the kinetic equation at equilibrium, but the error of its saddle-node bifurcation point is significant when compared to the HL2 and DQ closure rules. It is important here to note that when Hinch and Leal constructed both the HL1 and HL2 closure schemes, they were done so in an *ad hoc* method [22]. They chose the coefficients for many of the terms in their rules so that, at equilibrium, the critical points of the closure schemes and the kinetic solution would be in agreement.

CHAPTER IV

DQ CLOSURE UNDER SHEAR FLOW CONDITIONS

The goal of this portion of the research is to assess the validity of the proposed DQ closure scheme in comparison with the kinetic solution and four existing closure schemes. First, the proposed DQ closure rule is compared with the kinetic solution and the Doi (D), Tsuji-Rey (TR), Hinch-Leal 1 (HL1), and Hinch-Leal 2 (HL2) closure schemes. Various properties of the second moment tensor $\mathbf{Q}$ are studied. Upon completion of the initial study, simulations with the DQ closure scheme are run for a variety of N and Pe values. The resulting bifurcation diagrams in $(Pe, \mathbf{Q})$ and $(N, \mathbf{Q})$ space are generated noting the flow phases, along with other characteristic properties of $\mathbf{Q}$. Using this information, a bifurcation diagram of all stable states for the DQ closure scheme is built in (N, Pe) space, indicating the characteristic flow for each stable region. Lastly, the normal stress differences and apparent viscosity of the solutions simulated with the DQ closure are studied for each flow type, and compared to the known behavior of the kinetic solution. In all cases, the shape parameter is set to $a = 1.0$. This restricts the study to large aspect ratio rod-like liquid crystalline polymers, as described by (5) and Fig. 2.

In order to build the flow phase diagram for the solution, the bifurcation points need to be identified. As in previous research [1,7,8,12], AUTO bifurcation software is chosen. AUTO is designed to solve continuation and bifurcation ordinary differential equations. It identifies local bifurcation points based on the behavior of the eigenvalues, which are complex numbers. When an eigenvalue goes to zero there is a saddle node, transcritical, or pitch-fork bifurcation point (BP) which indicates a phase transition in the steady flow or periodic flow, but not between them. Note, AUTO does not differentiate between these three types of local bifurcation points. In order to change from steady flow to periodic flow, or vice versa, a Hopf bifurcation (HB) must occur. AUTO identifies a Hopf bifurcation by the eigenvalues being non-zero and purely imaginary. When solving the periodic portion of an ODE, AUTO has the capability to identify periodic doubling bifurcation points (PD). In the last case, if a local bifurcation is found and it has an eigenvalue with a modulus of one; if that eigenvalue is -1, then AUTO labels it a periodic doubling bifurcation.

IV.1 COMPARISON OF PROPOSED DQ CLOSURE SCHEME WITH KINETIC SOLUTION AND EXISTING CLOSURE SCHEMES

The proposed DQ closure rule is compared with the kinetic solution and the Doi (D), Tsuji-Rey (TR), Hinch-Leal 1 (HL1), and Hinch-Leal 2 (HL2) closure schemes. Three sample parameters, $Pe = 0.1$, $Pe = 10.0$, and $N = 6.0$, are selected in an attempt to capture a variety of behavior. Additionally, the four existing closure schemes are compared with each other and the kinetic solution.

At each sample N and Pe value, the flow phases for the solution generated by the DQ closure rule are listed. In order to determine the type of flow for any given (N, Pe) value, the eigenvectors $(\mathbf{n}_1, \mathbf{n}_2, \mathbf{n}_3)$ of $\mathbf{Q}$ are calculated, where $\mathbf{n}_1$ is the major director. $\mathbf{n}_1$ is written in terms of its spherical coordinates θ and ϕ where $\mathbf{n}_1 = (\sin\theta\cos\phi, \sin\theta\sin\phi, \cos\theta)$. From the values of θ and ϕ, the type of flow can be determined. For steady stable solutions, if $\theta = 90$ it is in-plane flow aligning (**FA**), if $\theta = 0$ it is log-rolling (**LR**), and otherwise it is out-of-plane steady (**OS**). For stable periodic solutions, if $\theta = 90$ it is in-plane; for all other values of θ it is out-of-plane. To determine the type of periodic flow, the value of ϕ over a single period must also be observed. For $\theta = 90$, if ϕ rotates between -90^o and 90^o, it is tumbling (**T**); otherwise it is wagging (**W**). For $\theta \neq 90$, if ϕ rotates between -90^o and 90^o, it is kayaking 1 (**K1**); otherwise it is kayaking 2 (**K2**) [1,8,13].

IV.1.1 $Pe = 0.1$

The first conditions under which the DQ closure rule is being studied are low shear rates, $0.0 < Pe < 1.0$. In previous studies [8], the kinetic solutions for $Pe = 0.1$ are generated, and therefore $Pe = 0.1$ is the chosen value for the initial study of the DQ closure scheme. Additionally, the nematic polymer concentration varies for $0.0 < N \leq 8.0$. Due to the wealth of research [8] that has been done on existing closure schemes and the kinetic solution under these shear flow conditions, the results from this section serve as a benchmarks for the kinetic and closure rule code in AUTO.

From the data, three components of the second moment tensor $\mathbf{Q}$ are calculated and graphed versus the nematic polymer concentration N. The components are chosen based on current literature for the kinetic simulations [1,8,13]; they include the L_2 norm of $\mathbf{Q}$, the value of the a_{20} component from the spherical harmonic expansion (17) of the PDF, $f(\mathbf{m}, t)$, and the Leslie alignment angle, ϕ_L, of $\mathbf{Q}$ which corresponds to the peak angle of the PDF [1]. When the closure rules are implemented in AUTO, the resulting outputs are the five independent components of the second moment tensor $\mathbf{Q}$. From this data, MATLAB is utilized to construct $\mathbf{Q}$ and calculate the L_2 norm in post-processing.

As discussed previously, when the kinetic solution is simulated in AUTO, the resulting output is a 65-parameter system. One of these parameters is the a_{20} component from the spherical harmonic expansion (17) of the PDF. In terms of the second moment tensor $\mathbf{Q}$, a_{20} can be found from the explicit definition [8]:

$$\begin{aligned}
\mathbf{Q}_{xx} &= -\frac{2}{3}\sqrt{\frac{\pi}{5}}a_{20} + \sqrt{\frac{8\pi}{15}}Re(a_{22}) \\
\mathbf{Q}_{yy} &= -\frac{2}{3}\sqrt{\frac{\pi}{5}}a_{20} - \sqrt{\frac{8\pi}{15}}Re(a_{22}) \\
\mathbf{Q}_{xy} &= -\sqrt{\frac{8\pi}{15}}Im(a_{22}) \\
\mathbf{Q}_{xz} &= -\sqrt{\frac{8\pi}{15}}Re(a_{21}) \\
\mathbf{Q}_{yz} &= \sqrt{\frac{8\pi}{15}}Im(a_{21}).
\end{aligned} \tag{48}$$

The systems of equations in (48) is used to construct $\mathbf{Q}$ from the kinetic output and to calculate the a_{20} component from the closure rule output. The significance of using the a_{20} component is that it serves as a specific point of comparison between the kinetic simulation and the closure rule simulations, in contrast to the L_2 norm of $\mathbf{Q}$.

Lastly, the Leslie alignment angle, ϕ_L, for steady solutions is calculated for each simulation. Recall, the Leslie alignment angle corresponds to the peak angle of the PDF $f(\mathbf{m}, t)$ [1]. In post-processing, MATLAB is used to find the eigenvalues and eigenvectors of $\mathbf{Q}$. The eigenvector corresponding to the largest eigenvalue signifies the major director, $\mathbf{n}_1$. The major director takes the form

$$\mathbf{n}_1 = (\sin\theta\cos\phi, \sin\theta\sin\phi, \cos\theta). \tag{49}$$

Recall θ is the polar angle measured from the vorticity (z) axis and ϕ is the latitude angle in the shear (x-y) plane. ϕ is measured counter-clockwise from the positive flow direction (x); y is the flow gradient direction [8]. In the case of in-plane flow aligning, $\theta = 90^o$, giving $\mathbf{n}_1 = (\cos\phi_L, \sin\phi_L, 0)$. For log-rolling, $\theta = 0^o$, giving $\mathbf{n}_1 = (0, 0, 1)$, and so ϕ_L is not calculated.

TABLE IV: Monodomain attractors and phase transitions vs nematic polymer concentration N at fixed shear rate $Pe = 0.1$ for the DQ closure scheme.

State	**FA**	**LR**
N Region	$(0, 4.8)$	$(4.8, 8.0)$

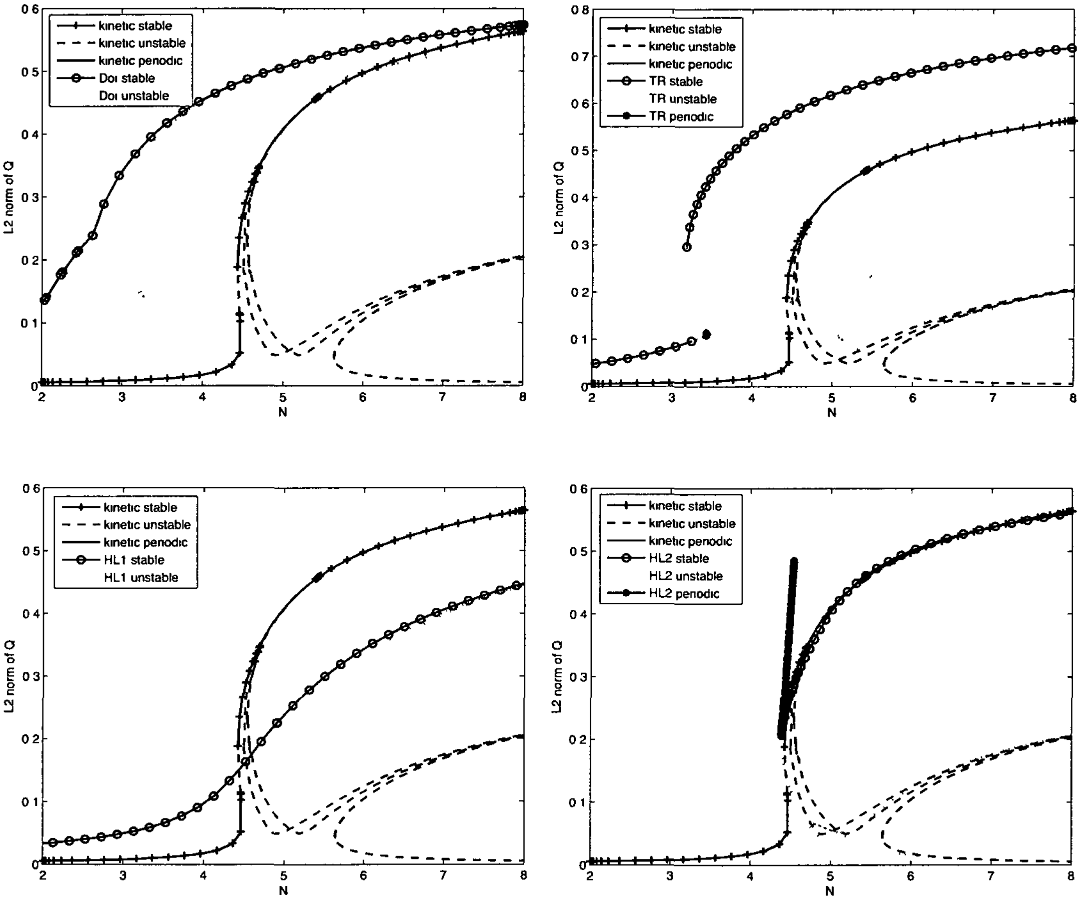

FIG. 5: Comparison of the L_2 norm of $\mathbf{Q}$ between the existing closure rules and the kinetic solution at $Pe = 0.1$. Top left: DOI closure. Top right: TR closure. Bottom left: HL1 closure. Bottom right: HL2 closure.

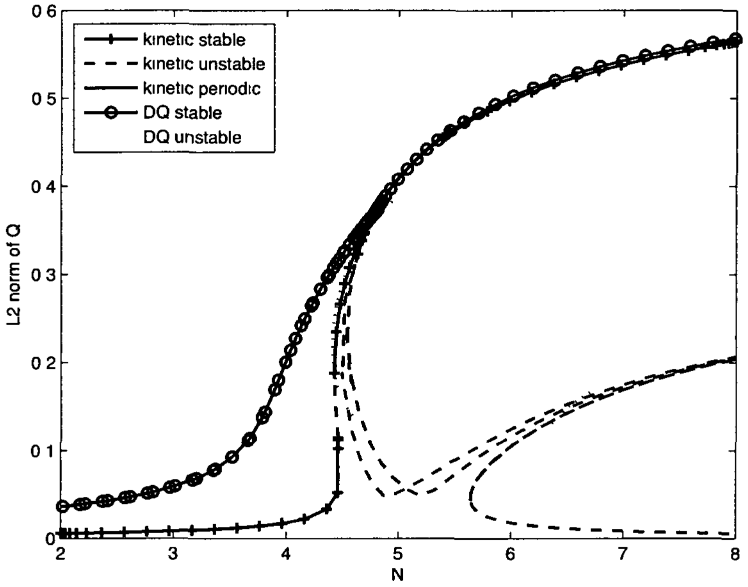

FIG. 6: Comparison of the L_2 norm of $\mathbf{Q}$ between the DQ closure rule and the kinetic solution at $Pe = 0.1$.

For $Pe = 0.1$, periodic solutions exist for the kinetic solution as well as the TR and HL2 closure schemes. The periodic solutions shown in Fig. 5 through Fig. 8 occur at the Hopf bifurcations (HB) which indicate a phase transition from stable steady flow to periodic flow. The steady flow may be either in the plane or out of the plane. The in-plane steady flow is referred to as flow aligning (**FA**) and the major director of the rigid-rod nematic polymer aligns with the direction of shear flow in the plane of deformation. For out-of-plane steady flow (**OS**), the major director does not line in the plane of deformation and it is not aligned with the vorticity axis. When the major director is in a stable state of flow aligned with the vorticity axis, it is referred to as log-rolling (**LR**) [1]. For the condition $Pe = 0.1$, periodic solutions stemming from Hopf bifurcations which occur between any periodic or log-rolling regions are not given Table IV details the phase transitions identified by the DQ closure scheme at $Pe = 0.1$. Note that the only flow phases simulated are **FA** and the **LR**, with the transition occurring at $N = 4.8$. For the DQ closure scheme, AUTO does not generate an HB point for $Pe = 0.1$. The lowest point in (N, Pe) space that AUTO detects an HB point for the proposed closure scheme is (4.85,0.189).

For the L_2 norm of $\mathbf{Q}$ at $Pe = 0.1$, Fig. 6 indicates that the DQ closure scheme

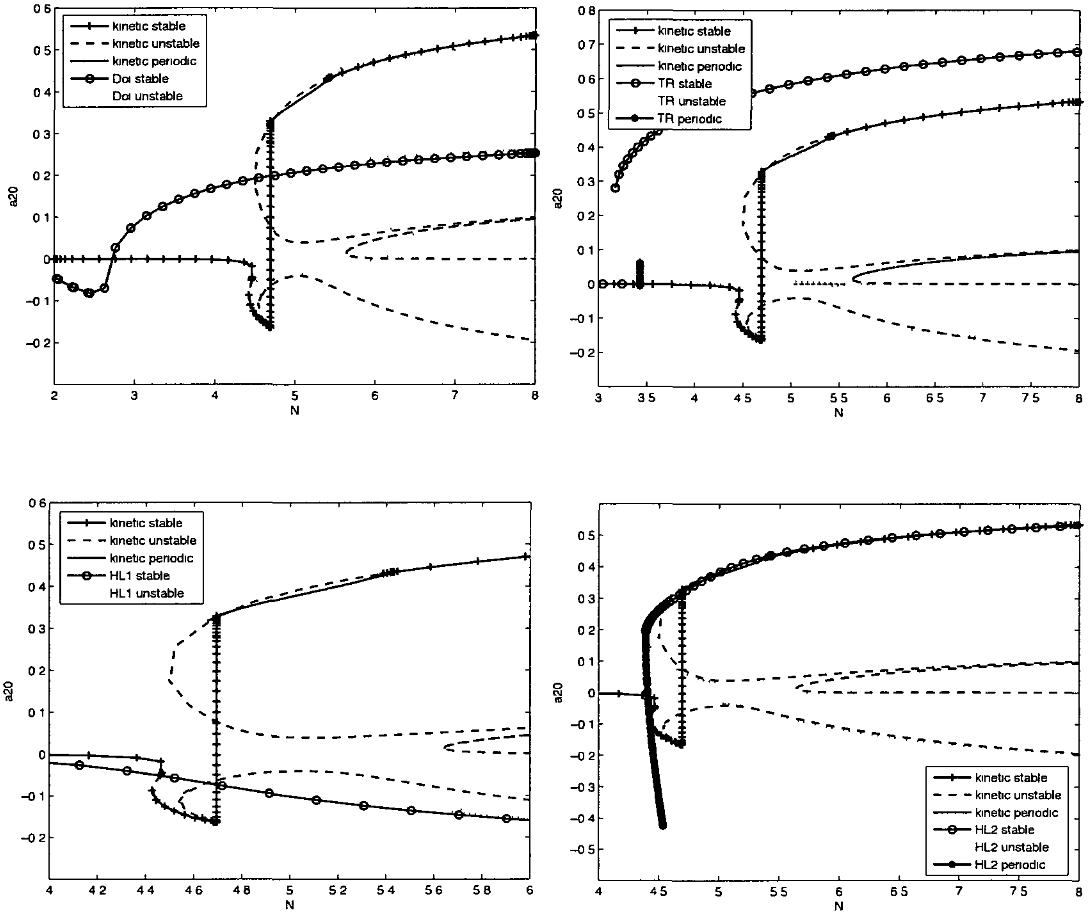

FIG. 7: Comparison of the a_{20} component of $\mathbf{Q}$ between the existing closure rules and the kinetic solution at $Pe = 0.1$. Top left: DOI closure. Top right: TR closure. Bottom left: HL1 closure. Bottom right: HL2 closure.

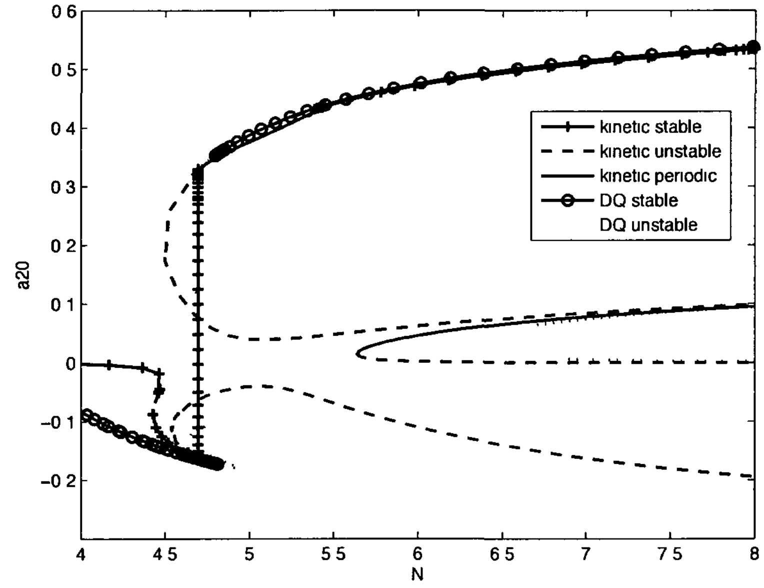

FIG. 8: Comparison of the a_{20} component of $\mathbf{Q}$ between the DQ closure rule and the kinetic solution at $Pe = 0$ 1.

detects branches comparable to the kinetic solution. The branches correspond to the bifurcation points. However, Fig 6 also shows that the DQ closure scheme fails to find any HB points and thus fails to predict all types of periodic flow. Looking at Fig. 5, the TR closure generates a very small periodic solution at $N \approx 3.5$, and the HL2 closure generates a periodic solution at $N \approx 4.4$. The kinetic solution has a HB point at $N \approx 4$ 5, thus indicating the birth of a periodic solution It is not of major concern that the periodic solutions from the closure schemes do not quantitatively align with those of the kinetic solution. It is more important that they predict some sort of periodic behavior. These types qualitative results are of particular significance for the manufacturing applications of liquid crystalline polymers How can one accurately design materials if the mathematical models they are using fail to predict entire flow phases? Extending the comparison of $\mathbf{Q}$ between the kinetic simulations and closure simulations down to a component-wise level, Fig. 7 and Fig. 8 indicate that similar observations for the existing closure schemes and proposed closure scheme can be made for the a_{20} component.

Lastly, when calculating the Leslie alignment angle, ϕ_L, for the steady solutions, the data is limited to the values of $\mathbf{Q}$ for which ϕ_L is determinable. This constraint

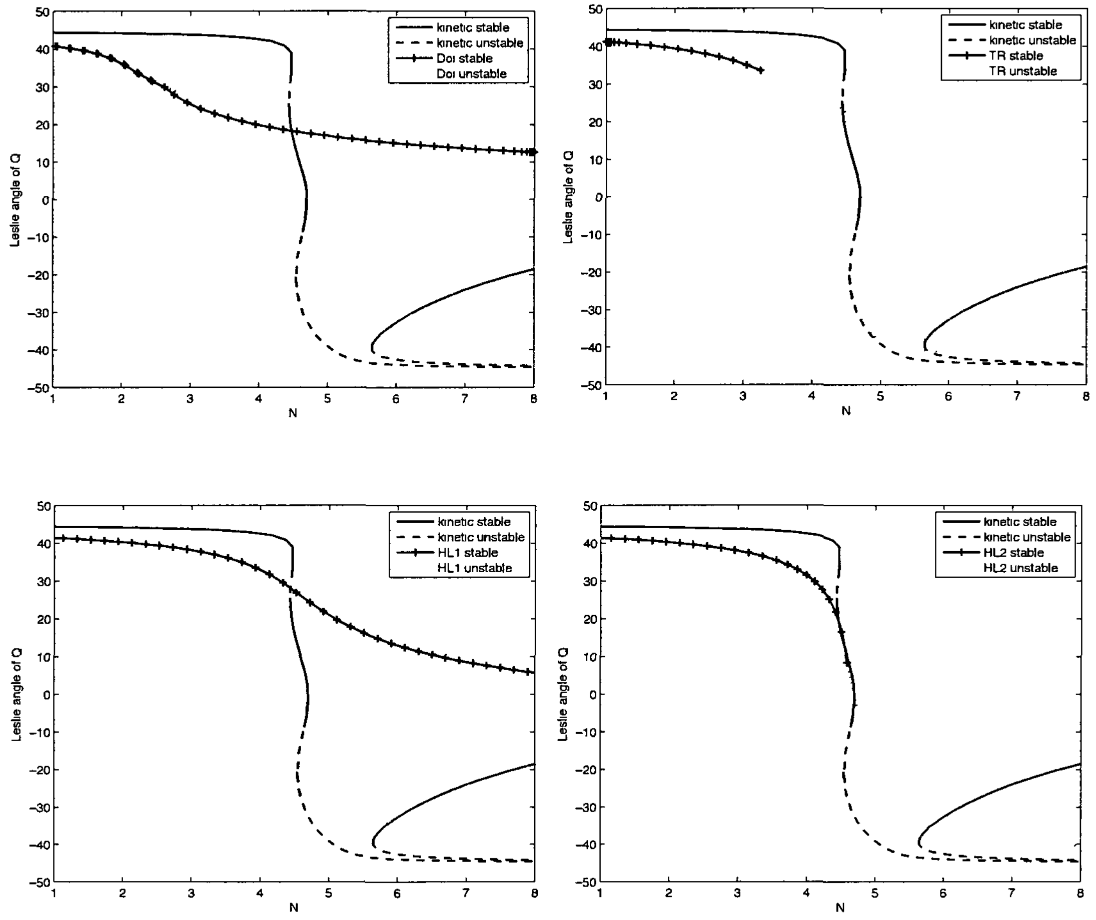

FIG. 9: Comparison of the Leslie alignment angle of **Q** between the existing closure rules and the kinetic solution at $Pe = 0.1$. Top left: DOI closure. Top right: TR closure. Bottom left: HL1 closure. Bottom right: HL2 closure.

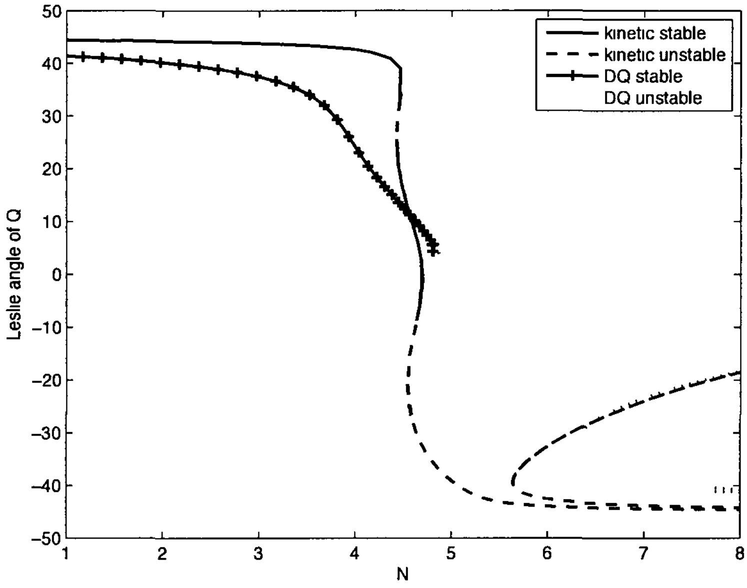

FIG. 10: Comparison of the Leslie alignment angle of **Q** between the DQ closure rule and the kinetic solution at $Pe = 0.1$.

is easily implemented in post-processing by excluding all log-rolling solutions. The results are graphed in Fig. 9 and Fig. 10 where ϕ_L is a function of the nematic concentration N over the domain $1.0 \leq N \leq 8.0$. The kinetic solution consists of a primary curve which originates from the stable flow-aligning phase at low polymer concentration, and a secondary unstable curve for higher concentrations. Looking at the primary curves in Fig. 9, for the kinetic simulation, $-45^o \leq \phi_L \leq 45^o$; there is a temporary change in stability around the angle $\phi_L \approx 35^o$ and a permanent change from stable to unstable at $\phi_L \approx -10^o$. For the Doi simulation, $13^o \leq \phi_L \leq 41^o$ and the solution is entirely stable. For the TR simulation, $-43^o \leq \phi_L \leq 41^o$. Unlike the kinetic solution, the TR solution has a permanent change in stability at $\phi_L \approx 35^o$. For the HL1 and HL2 simulations, $-41^o \leq \phi_L \leq 41^o$ and $-40^o \leq \phi_L \leq 41^o$, respectively. Like the Doi closure, the HL1 simulation fail to detect any unstable flow aligning solutions. The HL2 simulation fails detect the temporary change in stability around $\phi_L = 35^o$, but it does identify a permanent transition to instability at $\phi_L \approx 5^o$. This is closer to the kinetic solution's transition point of $\phi_L \approx -10^o$ than the other existing closures. Finally, for the DQ simulation depicted in Fig. 10, $-41^o \leq \phi_L \leq 42^o$. Note that the DQ closure scheme also fails to detect the intermittent unstable solution, however the transition to unstable occurs at $\phi_L \approx 5^o$, which agrees with the HL2 closure scheme. Looking at the secondary curves in Fig. 9 and Fig. 10, it is clear that only the HL1 and DQ closures simulate an unstable solution with a parabola-like curve for higher concentrations, similar to that of the kinetic case.

IV.1.2 $Pe = 10.0$

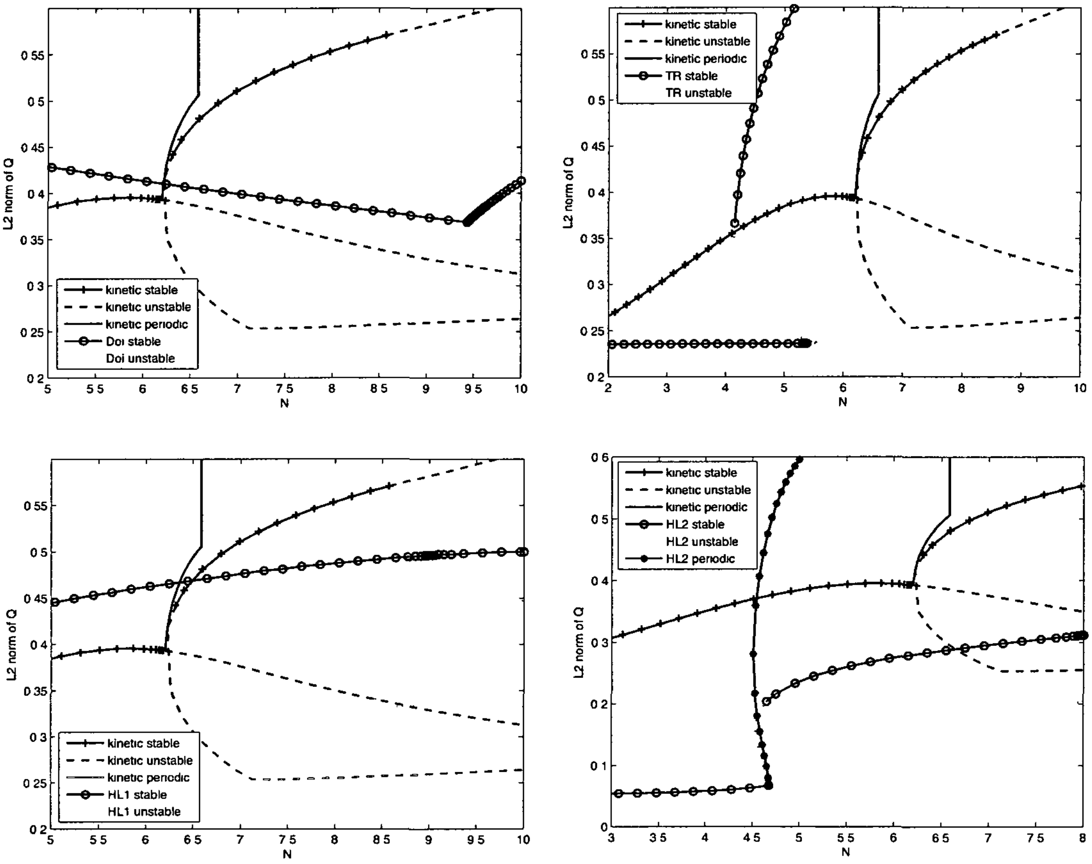

FIG. 11: Comparison of the L_2 norm of $\mathbf{Q}$ between the existing closure rules and the kinetic solution at $Pe = 10.0$. Top left: DOI closure. Top right: TR closure. Bottom left: HL1 closure. Bottom right: HL2 closure.

Secondly, the DQ closure rule is being studied under the conditions of higher finite shear rates, $1.0 \leq Pe \leq 10.0$. In previous studies [1], the flow phase diagram for the kinetic solution was generated for $1.0 \leq Pe \leq 10.0$ and $4.5 \leq N \leq 6.5$. The shear rate parameter is set to $Pe = 10.0$ and nematic polymer concentration varies for $0.0 < N \leq 10.0$. The flow phase diagram is used to ensure that all branches of

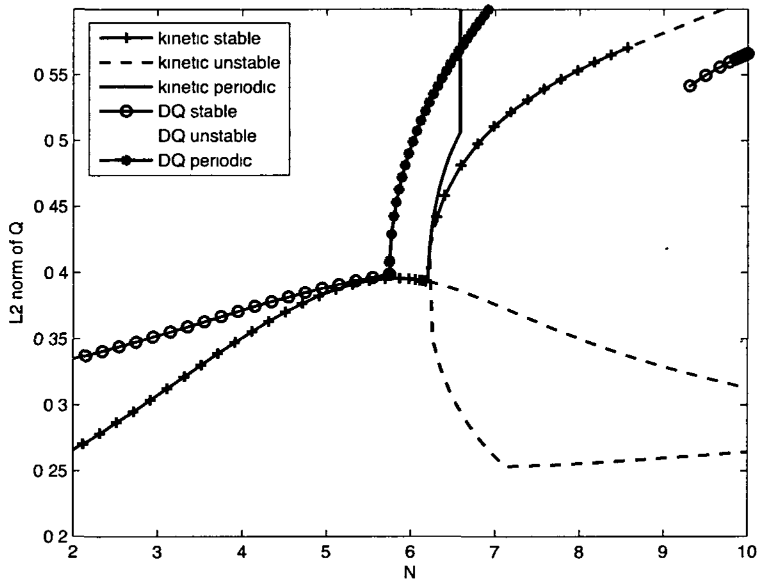

FIG. 12: Comparison of the $L_2 0$ norm of $\mathbf{Q}$ between the DQ closure rule and the kinetic solution at $Pe = 10.0$.

the solution have been generated by the kinetic simulation in AUTO. AUTO is a numerical solver and so as parameter values change, the step sizes and the tolerances often need to be adjusted in order to capture all bifurcations.

For $Pe = 10.0$, periodic solutions bifurcating from the steady stable flow exist for the kinetic solution as well as the HL2 and DQ closure schemes. The periodic solutions shown in Fig. 11 through Fig. 14 occur at Hopf bifurcations separating the stable steady flow regions from the periodic regions Periodic solutions stemming from Hopf bifurcations which occur between any periodic or log-rolling regions are not shown. For $Pe = 10.0$, the L_2 norm of $\mathbf{Q}$, the value of the a_{20} component of $\mathbf{Q}$, and the Leslie angle (ϕ_L) of $\mathbf{Q}$ are found and graphed for the kinetic solution and each closure rule.

For the L_2 norm of $\mathbf{Q}$ at $Pe = 10.0$, Fig. 11 indicates that the Doi closure scheme fails to find one unstable branch of the steady kinetic solution, while the solutions from the TR and HL2 closures more closely resemble the kinetic solution. The HL1 closure fails to have the pitchfork shape of the kinetic solution within the given domain for N. The nematic solution was only run for $0.0 \leq N \leq 10.0$, at some point $N > 10.0$, the two upper branches of the HL1 solution will intersect. There must be

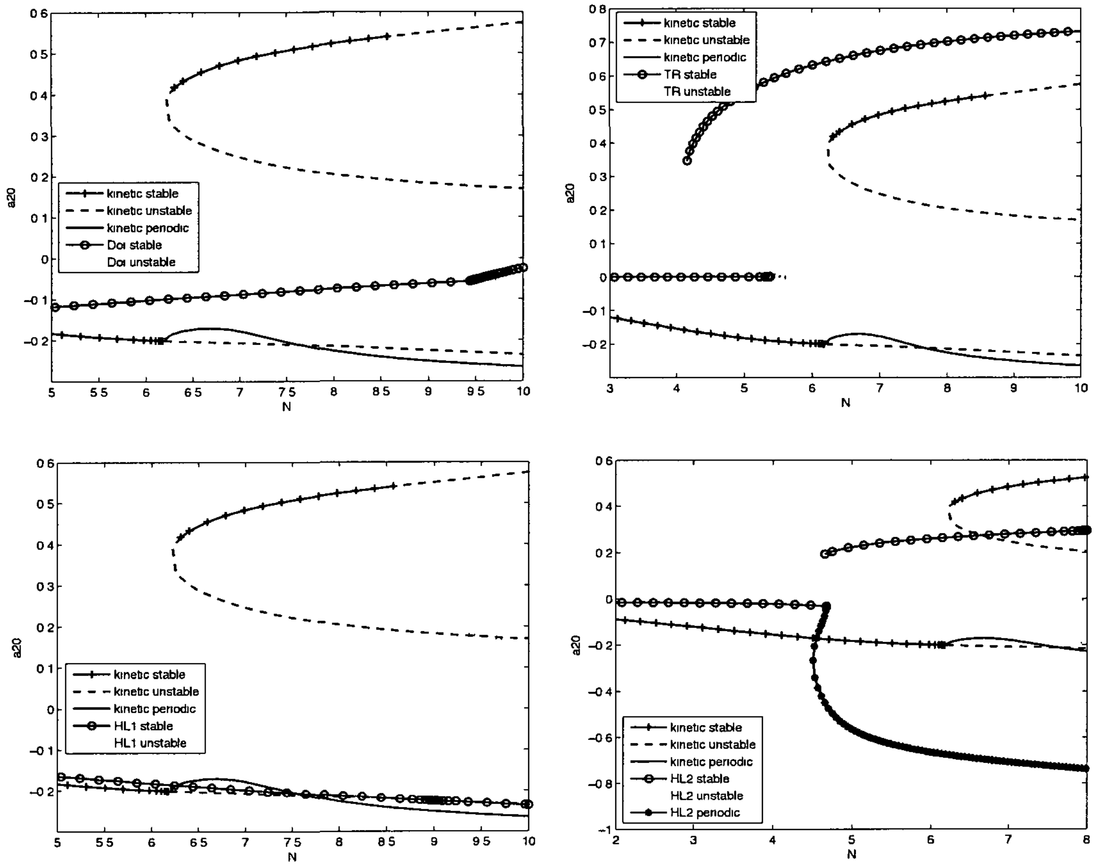

FIG. 13: Comparison of the a_{20} component of $\mathbf{Q}$ between the existing closure rules and the kinetic solution at $Pe = 10.0$. Top left: DOI closure. Top right: TR closure. Bottom left: HL1 closure. Bottom right: HL2 closure.

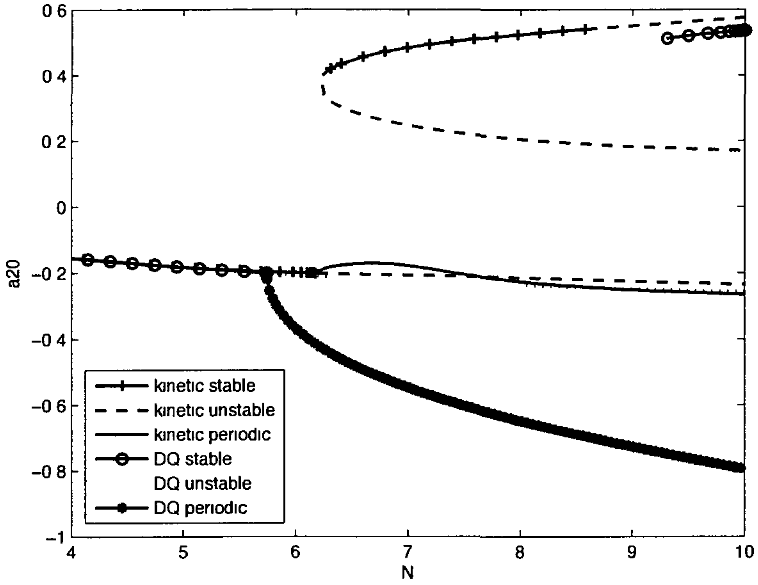

FIG. 14: Comparison of the a_{20} component of $\mathbf{Q}$ between the DQ closure rule and the kinetic solution at $Pe = 10.0$.

a bifurcation point in order for a branch to exist. Looking at Fig. 11, the HL2 closure generates a periodic solution at $N \approx 4.65$. The kinetic solution has a HB point at $N \approx 6.2$, thus indicating the birth of a periodic solution. Fig. 12, indicates the DQ closure generates a periodic solution at $N \approx 5.5$. Note how the birth periodic solution for the HL2 closure is at the start of the pitchfork, just as in the case of the kinetic solution. In the case of the DQ closure, the birth of the periodic solution occurs at a polymer concentration much lower than where the pitchfork splits ($N \approx 8.9$). Alternatively, the location of the Hopf bifurcation and the resulting periodic solution for the DQ closure is closer to the kinetic solution than that of the HL2 closure. Table V gives a detailed description of the phase transitions at $Pe = 10\ 0$ under the DQ closure scheme. An initial phase transition occurs from **FA** to **W** at $N = 5.75$. This periodic branch undergoes a second phase transition to **T** at $N = 9.55$ and it ceases at $N = 9\ 81$. At $N = 5\ 75$, the **FA** branch becomes an unstable steady solution until $N = 9.3$, when a phase transition into **LR** occurs. The **LR** branch remains stable for the remainder of the domain in the simulation.

Extending the comparison of $\mathbf{Q}$ between the kinetic simulations and closure simulations down to a component-wise level, Fig. 13 and Fig. 14 indicate that the similar

TABLE V: Monodomain attractors and phase transitions vs nematic polymer concentration N at fixed shear rate $Pe = 10.0$ for the DQ closure scheme.

State	**FA**	**W**	**LR/W**
N Region	$(0, 5.75)$	$(5.75, 9.3)$	$(9.3, 9.55)$
State	**LR/T**	**LR**	
N Region	$(9.55, 9.81)$	$(9.81, 10.0)$	

observations for the existing closure schemes and proposed closure scheme can be made for the a_{20} component. The most significant observation from Fig. 11 and Fig. 13 is that the HL2 closure rule more closely resembles the kinetic solution than the other existing closures, but the solutions seem shifted to areas of lower polymer concentration than in the kinetic case. For the DQ closure, the opposite behavior occurs. Fig. 12 and Fig. 14 illustrate how the solution from proposed closure seems shifted to areas of higher polymer concentration when compared to the kinetic solution, with the exception of the location of the periodic solution for the DQ closure scheme. This observation will be of importance later.

In the case of calculating the Leslie alignment angle, ϕ_L, for steady solutions, the data does not include log-rolling flow. The results are graphed in Fig. 15 and Fig. 16 where the ϕ_L is a function of the nematic concentration N over the domain $0 \leq N \leq 10.0$. From Fig. 15, for the kinetic simulation, $-22^o \leq \phi_L \leq 20^o$; there is a transitions from stable to unstable at $\phi_L \approx -5^o$. For the Doi simulation, there is very little change in the leslie alignment angle, $10^o \leq \phi_L \leq 12^o$, and there is no change in stability. For the TR simulation, $-5^o \leq \phi_L \leq 4^o$. For the HL1 and HL2 simulations, $0^o \leq \phi_L \leq 7^o$ and $-2^o \leq \phi_L \leq 3^o$, respectively. Like the Doi simulation, the HL1 closure's simulation fails to detect any unstable steady solution, as in the case of $Pe = 0.1$. The TR and HL2 simulations both detect a transition from stable to unstable at $\phi_L \approx 0^o$. From Fig. 16 for the DQ simulation, $-5^o \leq \phi_L \leq 5^o$. Like the TR and HL2 simulations, the DQ closure identifies a change in stability at $\phi_L \approx 0^o$.

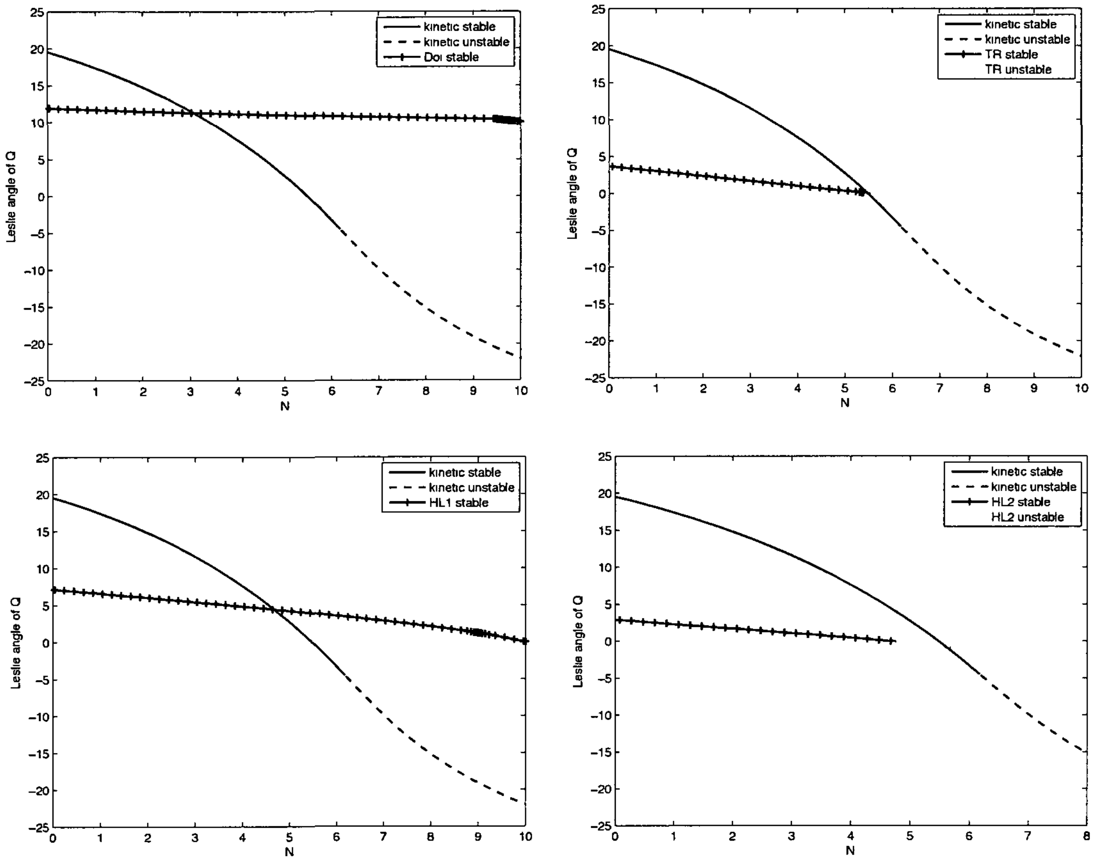

FIG. 15: Comparison of the Leslie alignment angle of **Q** between the existing closure rules and the kinetic solution at $Pe = 10.0$. Top left: DOI closure. Top right: TR closure. Bottom left: HL1 closure. Bottom right: HL2 closure.

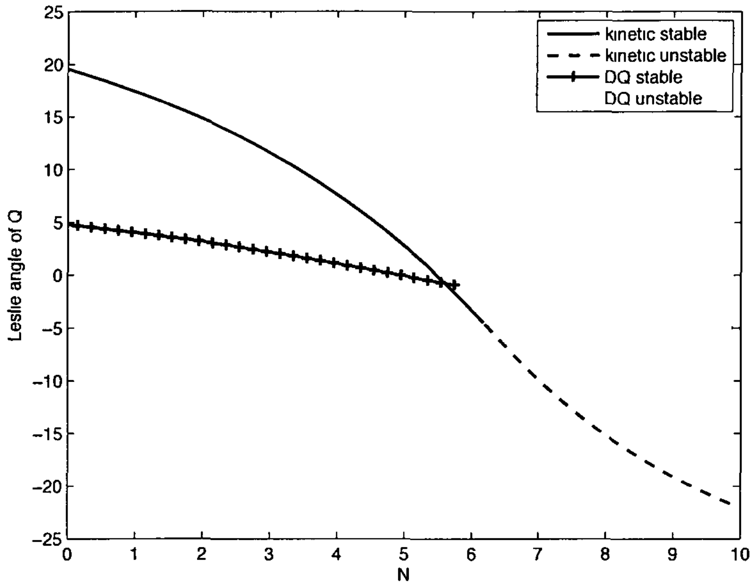

FIG. 16: Comparison of the Leslie alignment angle of **Q** between the DQ closure rule and the kinetic solution at $Pe = 10.0$.

IV.1.3 $N = 6.0$

Lastly, the closure rules are being compared under the conditions of varying finite shear rates with a constant nematic concentration. In previous studies [12], the kinetic solutions for constant polymer concentration $N = 6\ 0$ are generated. For this reason, $N = 6\ 0$ is the chosen for the study of the DQ closure scheme and the shear rate varies for $0.0 \leq Pe \leq 10\ 0$. Due to the wealth of research [1,12] that has been done on the kinetic solution under these shear flow conditions, the kinetic solutions in Fig. 17 through Fig. 20 can be validated. This ensures a correct frame of reference for comparisons among the kinetic simulations and closure rule simulations. The L_2 norm of **Q** and the value of the a_{20} component of **Q** are calculated and graphed for the kinetic solution and each closure rule at $N = 6.0$. The Leslie angle ϕ_L for $N = 6.0$ is discussed in a later section.

For $N = 6.0$, periodic solutions were generated for the kinetic solution and the DQ closure scheme. In Fig. 17 and Fig. 19, it can be seen that the TR and HL2 closures do not attain a steady stable state at $N = 6.0$ for any shear rate in the domain $0.0 \leq Pe \leq 10.0$. While the Doi and HL1 closures demonstrate both stability and

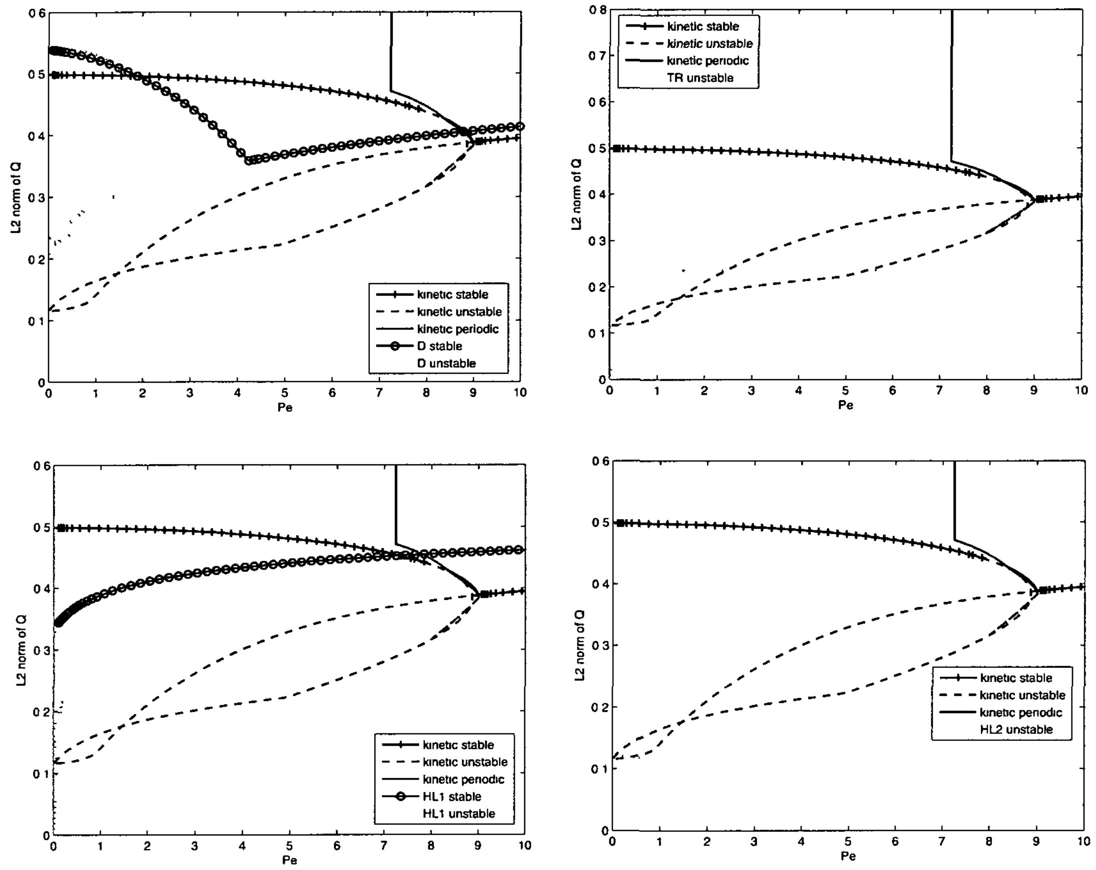

FIG. 17: Comparison of the L_2 norm of $\mathbf{Q}$ between the existing closure rules and the kinetic solution at $N = 6.0$. Top left: DOI closure. Top right: TR closure. Bottom left: HL1 closure. Bottom right: HL2 closure.

TABLE VI: Monodomain attractors and phase transitions vs shear rate Pe at fixed nematic polymer concentration $N = 6.0$ for the DQ closure scheme.

State	**LR**	**LR/W**
Pe Region	$(0, 1.18)$	$(1.18, 1.22)$
State	**K1/W**	**W**
Pe Region	$(1.22, 1.31)$	$(1.31, 10.0)$

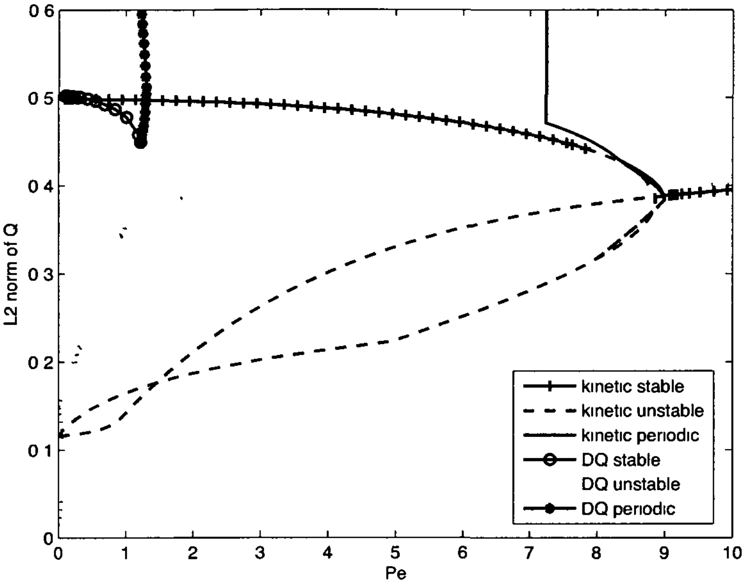

FIG. 18: Comparison of the L_2 norm of $\mathbf{Q}$ between the DQ closure rule and the kinetic solution at $N = 6.0$.

instability, AUTO did not detect an HB point from their steady stable flow phases In Fig. 17 through Fig. 20, the periodic solution for the kinetic and DQ closure rule solutions occur at the Hopf bifurcations separating the stable steady flow regions from the adjacent periodic regions. Periodic solutions stemming from Hopf bifurcations which occur between any periodic regions are not shown. In the next section, the types of flow for the DQ closure rule are inspected and all periodic solutions are given regardless of the region. Table VI gives a detailed description of the phase transitions at $N = 6.0$ under the proposed DQ closure scheme. The DQ simulation does not attain a steady flow aligning or out-of-plane steady state at this value. All stable flows in Fig. 18 and Fig. 20 are **LR**. A phase transition from **LR** to **LR/W** occurs at $Pe = 1.18$, and the **LR** phase ceases at $Pe = 1.22$ with the birth of the **K1** flow phase. This is a very interesting, and unexpected, characteristic of the DQ closure rule which will be examined further in the next section.

IV.1.4 Summary

In sum, the DQ closure rule outperforms the other closure rules in many areas. For weak flow, $Pe = 0\ 1$, the DQ closure finds all steady branches the kinetic solution

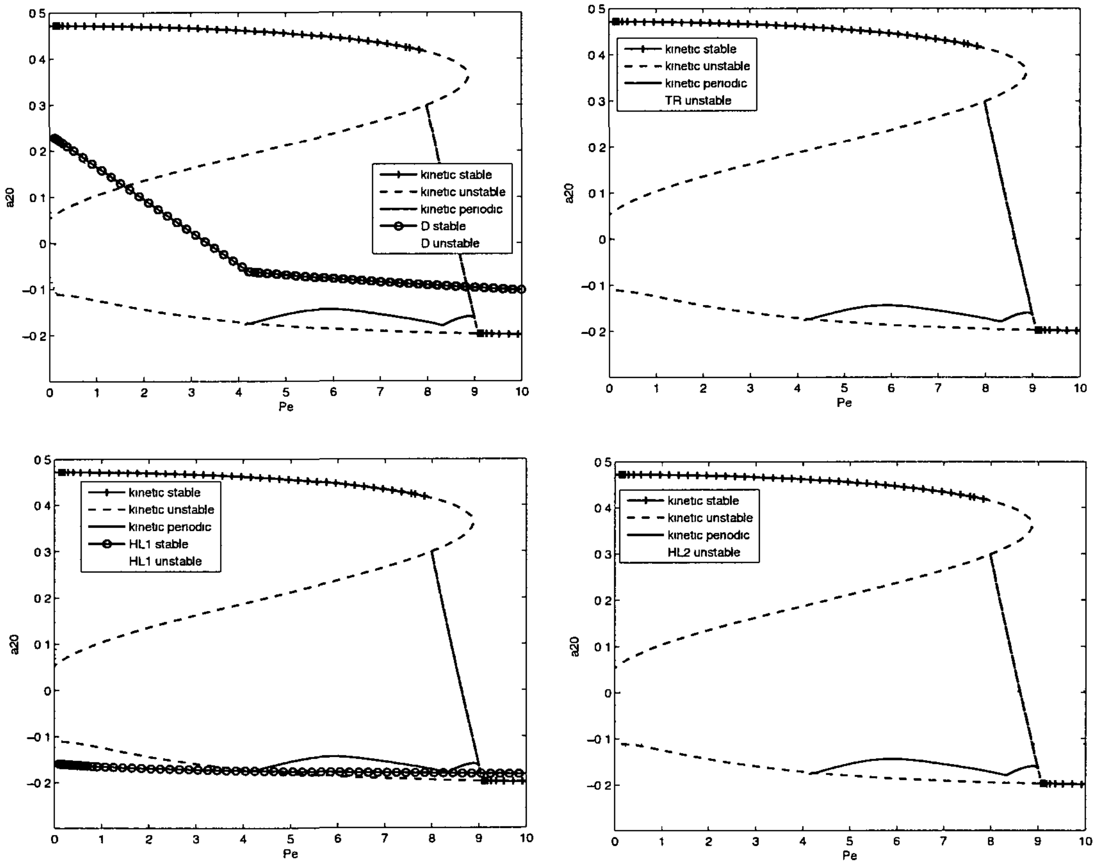

FIG. 19: Comparison of the a_{20} component of $\mathbf{Q}$ between the existing closure rules and the kinetic solution at $N = 6.0$. Top left: DOI closure. Top right: TR closure. Bottom left: HL1 closure. Bottom right: HL2 closure.

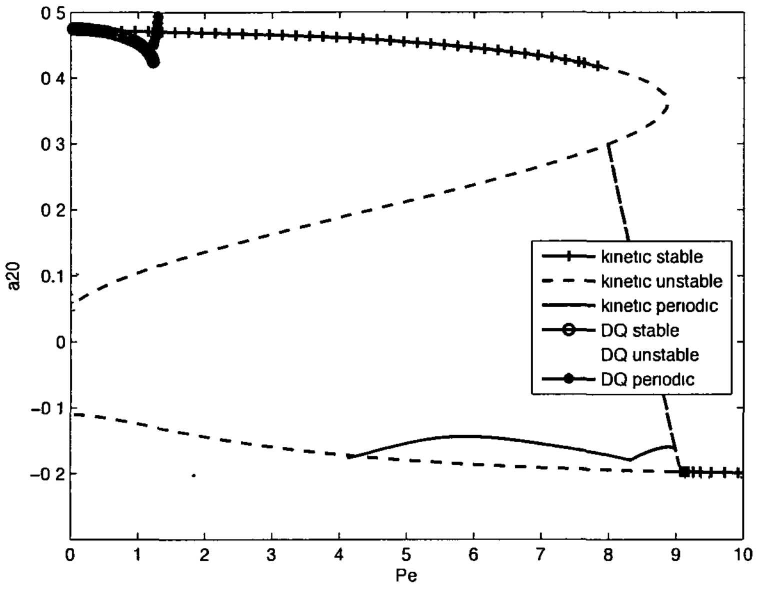

FIG. 20: Comparison of the a_{20} component of $\mathbf{Q}$ between the DQ closure rule and the kinetic solution at $N = 6.0$.

identifies, while the DOI, TR, and HL1 do not. However, the proposed closure fails to identify any periodic solutions, while the HL2 and TR closure captures those types of solutions. Quantitatively, the values of those periodic solutions are not representative of the periodic solutions form the kinetic equation at $Pe = 0.1$. This failing of the proposed closure seems to disappear as the flow is increased; for $Pe \geq 0.189$, periodic flow can be identified. For stronger flow, $Pe = 10.0$, the DQ closure finds both the steady and periodic branches that the kinetic solution identifies, while the DOI, TR, and HL1 do not. When looking at both the weak flow and stronger flow, the DQ closures simulations have stable solutions which are more similar to those of the kinetic solution than any of the other four closures.

When looking at the case of varying flow with steady concentration at $N = 6.0$, the DQ closure is the only closure rule in this study that identifies both the steady and periodic branches found in the kinetic solution. As a natural consequence, the general shape of the solution with the DQ closure rule more closely resembles that of the kinetic solution, and thus it is qualitatively superior.

These combined results indicate that, in general, for a given region of nematic concentration, N, and flow rate, Pe, the proposed closure may be more likely to capture similar attractors. In the following section, the attractors and transitions of nematic polymers for solutions using the DQ closure scheme will be investigated. These results will be compared with the known results of the kinetic solution.

IV.2 ATTRACTORS AND TRANSITIONS OF NEMATIC POLYMERS USING THE DQ CLOSURE SCHEME

The DQ closure scheme is run for a variety of N and Pe values. The values are chosen based on a basic bifurcation diagram in (N, Pe) space that shows how the flow regions for the DQ closure rule are divided. Each region needs to have at least one N and one Pe value to ensure that all flow transitions are detected resulting in five sample parameters being chosen: $Pe = 1.0$, $Pe = 5.0$, $N = 5.5$, $N = 6.0$, and $N = 8.0$. All periodic solutions are generated for each parameter.

IV.2.1 $Pe = 1.0$

For $Pe = 1.0$, the norm of $\mathbf{Q}$, the Leslie angle, and the components $\mathbf{Q}_{xx}$ and $\mathbf{Q}_{xz}$ are graphed. For $\mathbf{Q}_{xz} = 0$, it is an in-plane attractor; for $\mathbf{Q}_{xz} \neq 0$, it is an out-of-plane attractor. By selecting $Pe = 1.0$, all flow regions for the lower half of the bifurcation diagram for the DQ closure scheme in (N, Pe) space can be identified.

TABLE VII: Monodomain attractors and phase transitions vs nematic polymer concentration N at fixed shear rate $Pe = 1.0$ for the DQ closure scheme.

State	**FA**	**OS**	**K2**	**W**
N Region	$(0, 5.15)$	$(5.15, 5.31)$	$(5.31, 5.63)$	$(5.63, 5.73)$
State	**K1/W**	**W/LR**	**LR**	
N Region	$(5.73, 5.78)$	$(5.78, 5.86)$	$(5.86, 8.00)$	

At $Pe = 1.0$, the DQ closure scheme simulates a multitude of flow types. Table VII gives a detailed description of the stable phase transitions, while Fig. 21 graphs the L_2 norm of $\mathbf{Q}$ along with its phase transitions. At $N \approx 0$, the solution is **FA** until $N = 5.15$, where it undergoes a bifurcation into **OS** flow. With a slight increase in the nematic concentration, the **OS** solution transitions into the out-of-plane periodic **K2** phase at the occurrence of a HB point at $N = 5.31$. At $N = 5.63$, the out-of-plane periodic solution transitions into a steady in-plane periodic **W** phase. The

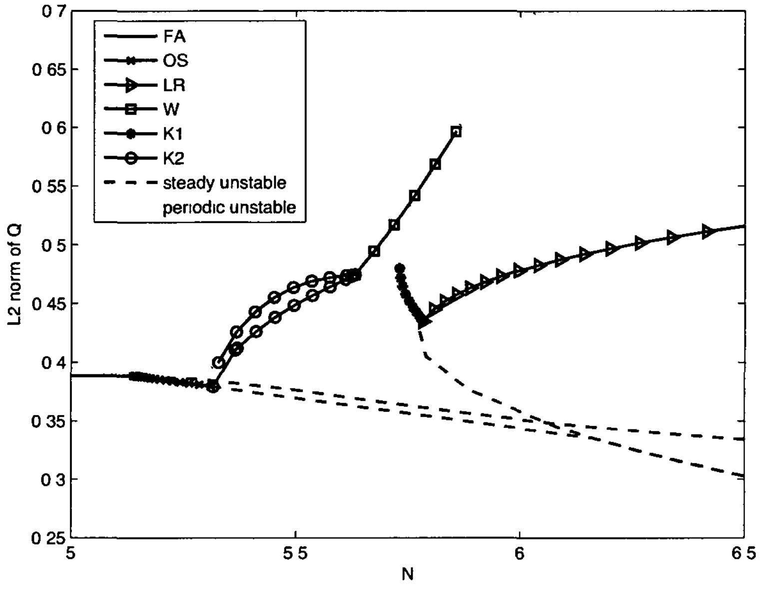

FIG. 21: L_2 norm of $\mathbf{Q}$ for DQ closure rule along with its phase transitions at $Pe = 1.0$.

simulation enters a period of bi-stability at $N = 5.73$ with the birth of the **K1** flow phase. The solution continues to have bi-stability until a change in stability of the **W** flow phase at $N = 5.86$. While the solution is exhibiting periodic flow, the unstable steady flow branch exhibits a pitch-fork bifurcation as N increases. The top branch of the pitchfork has a Hopf-bifurcation at $N = 5.78$ which corresponds to the end of the stable periodic **K1** flow phase and the birth of the stable steady **LR** flow phase.

The Leslie alignment angle, ϕ_L for steady solutions, does not include data from log-rolling flow phase The results are graphed in Fig. 22, where the ϕ_L is a function of the nematic concentration N over the domain $0 \leq N \leq 8.0$. For the kinetic simulation, $-40^o \leq \phi_L \leq 40^o$; there is a transitions from stable to unstable at $\phi_L \approx -5^o$. For the DQ simulation, $-21^o \leq \phi_L \leq 25^o$. The DQ closure identifies a transition from stable to unstable at $\phi_L \approx -4^o$. This follows the general pattern of the Leslie alignment angle from the DQ closure scheme having a smaller range than that of the kinetic solution established during the simulations for $Pe = 0.1$ and $Pe = 10.0$. The order parameter d1 (largest eigenvalue) for the flow aligning and log-rolling states at the flow rate $Pe = 1.0$ is given in Fig. 23. As the concentration N increases, the degree of alignment increases. In Fig. 24, for higher concentrations

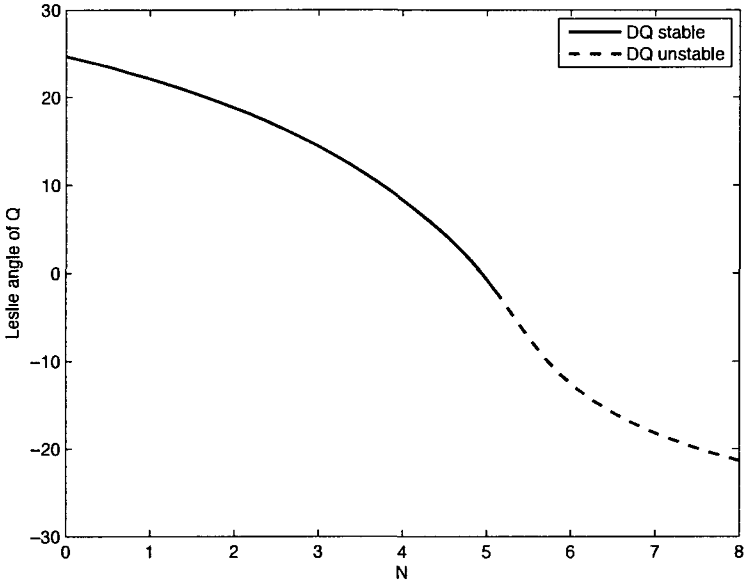

FIG. 22: Leslie alignment angle of **Q** under the DQ closure at $Pe = 1.0$.

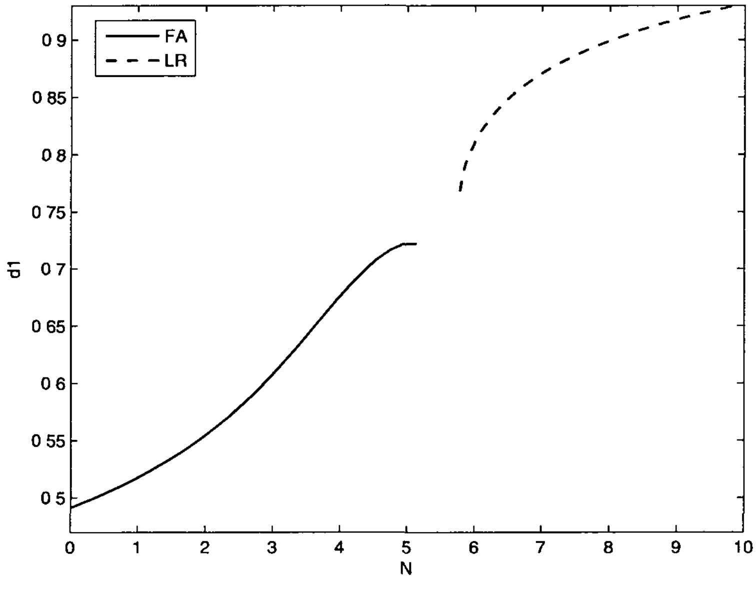

FIG. 23: Order parameter (largest eigenvalue) d1 for the DQ closure at $Pe = 1.0$.

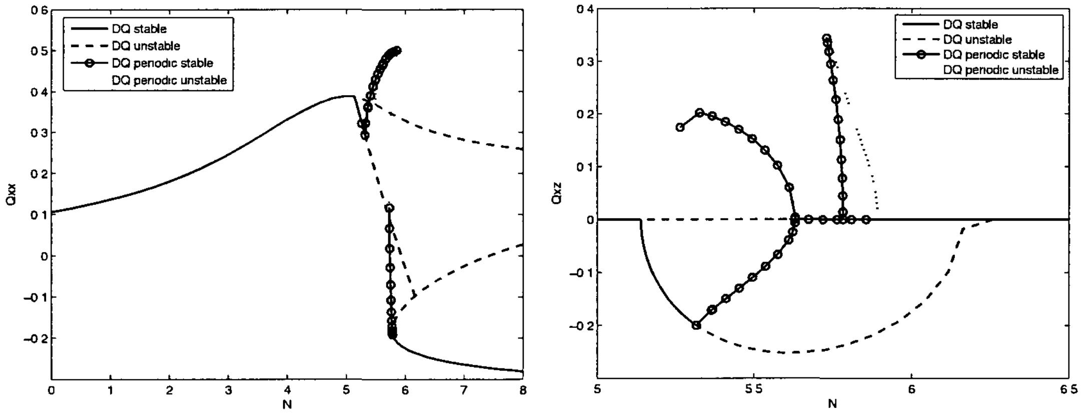

FIG. 24: Components $\mathbf{Q}_{xx}$ and $\mathbf{Q}_{xz}$ vs N for $Pe = 1.0$ from simulation with DQ closure rule. Left: $\mathbf{Q}_{xx}$. Right: $\mathbf{Q}_{xz}$.

of N and $\mathbf{Q}_{xx} < 0$ the solution is in its log-rolling state. As the concentration is decreased, a phase transition occurs and the solution enters its **K1** flow phase which is marked by a steep change in the value of $\mathbf{Q}_{xx}$ from negative to positive. All other flow phases are marked by $\mathbf{Q}_{xx} > 0$. For $\mathbf{Q}_{xz} \neq 0$, one can see the transitions from in-plane, steady and periodic stable and log-rolling solutions, to out of plane steady and periodic solutions.

IV.2.2 $Pe = 5.0$

For $Pe = 5.0$, the norm of $\mathbf{Q}$, the Leslie angle, and the components $\mathbf{Q}_{xx}$ and $\mathbf{Q}_{xz}$ are graphed. By selecting $Pe = 5.0$, all flow regions for the upper half of the bifurcation diagram for the DQ closure scheme in (N, Pe) space can be identified.

TABLE VIII: Monodomain attractors and phase transitions vs nematic polymer concentration N at fixed shear rate $Pe = 5.0$

State	**FA**	**W**	**T**
N Region	$(0, 5.73)$	$(5.73, 7.70)$	$(7.70, 7.87)$
State	**T/K1**	**T/LR**	**LR**
N Region	$(7.87, 8.07)$	$(8.07, 8.28)$	$(8.28, 10.0)$

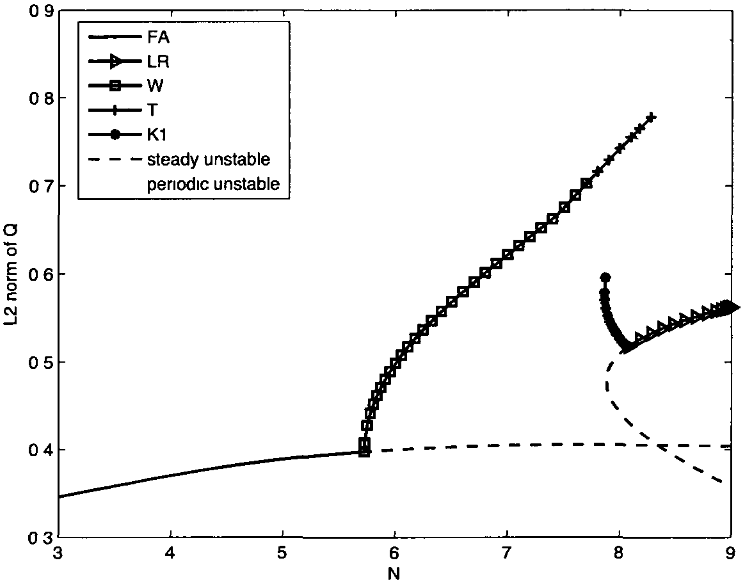

FIG. 25: L_2 norm of $\mathbf{Q}$ for DQ closure rule along with its phase transitions at $Pe = 5.0$.

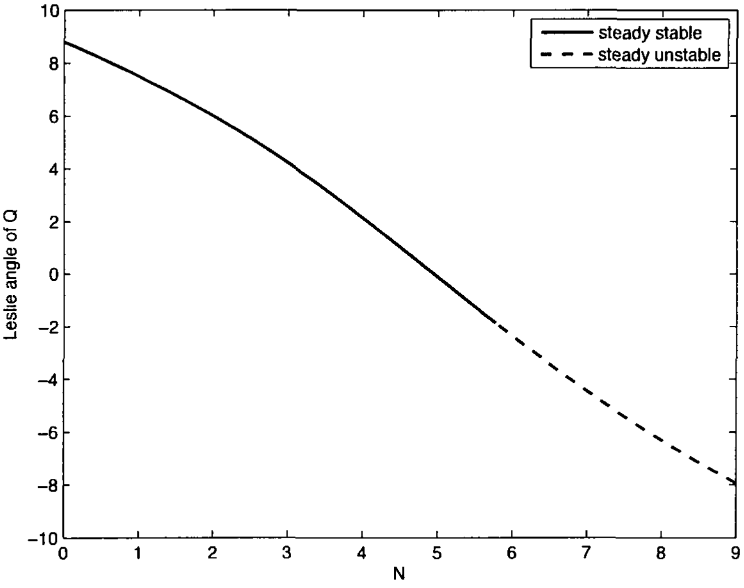

FIG. 26: Leslie alignment angle of $\mathbf{Q}$ under the DQ closure at $Pe = 5.0$.

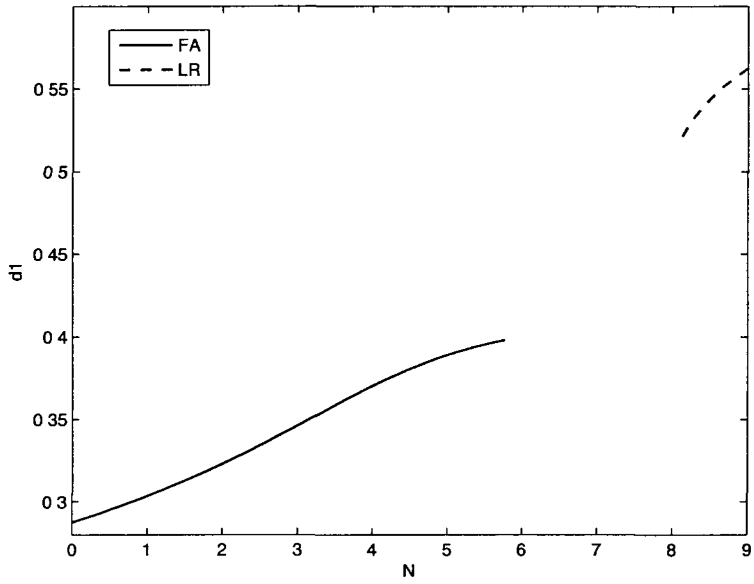

FIG. 27: Order parameter (largest eigenvalue) d1 for the DQ closure at $Pe = 5.0$.

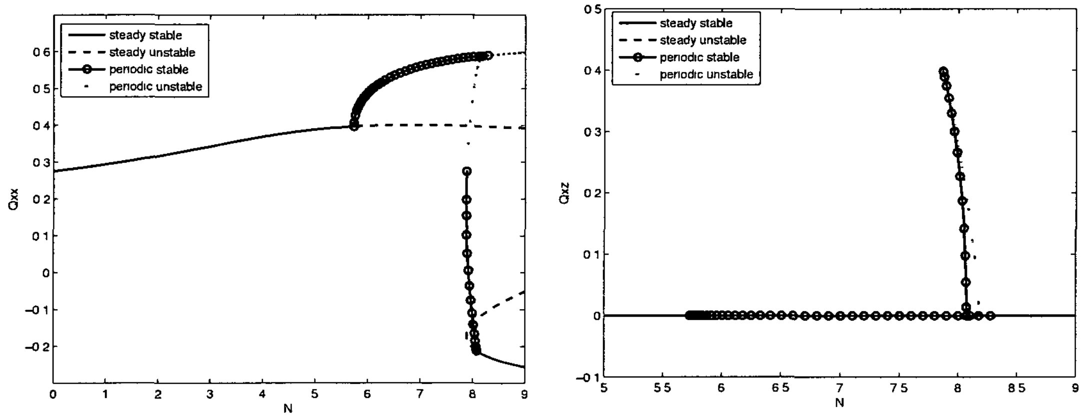

FIG. 28: Components $\mathbf{Q}_{xx}$ and $\mathbf{Q}_{xz}$ vs N for $Pe = 5.0$ from simulation with DQ closure rule. Left: $\mathbf{Q}_{xx}$. Right: $\mathbf{Q}_{xz}$.

At $Pe = 5.0$, the DQ closure scheme simulates many flow types. Table VIII gives a detailed description of the stable phase transitions, while Fig. 25 graphs the L_2 norm of $\mathbf{Q}$ along with its phase transitions. At $N \approx 0$, the solution is **FA** until the occurrence of a HB point at $N = 5.73$, where it bifurcates into the in-plane periodic **W** phase and an unstable steady flow phase. Unlike the $Pe = 1.0$ case, the **FA** phase does not transition into the **OS** flow phase. While N is increasing, the period of the **W** solution is also increasing until it reaches a maximum of 90^0 at which point in enters the **T** flow phase at $N = 7.70$. The **T** branch remains stable until $N = 8.28$. The simulation enters a period of bi-stability at $N = 7.87$ with the birth of the **K1** flow phase. The solution continues to have bi-stability until the end of the stable in-plane periodic flow phase, **T**. While the solution is exhibiting periodic flow, the unstable steady flow branch exhibits a pitch-fork bifurcation as N increases. The top branch of the pitchfork has a Hopf-bifurcation at $N = 8.07$ which corresponds to the end of the stable periodic **K1** flow phase and the birth of the stable steady **LR** flow phase.

The Leslie alignment angle, ϕ_L for steady solutions, does not include data from log-rolling flow phase. The results are graphed in Fig. 26, where the ϕ_L is a function of the nematic concentration N over the domain $0 \leq N \leq 9.0$. For the DQ simulation, $-8^o \leq \phi_L \leq 9^o$; a transition from stable to unstable identified at $\phi_L \approx -2^o$. The order parameter d1 (largest eigenvalue) for the flow aligning and log-rolling states at the flow rate $Pe = 1.0$ is given in Fig. 27. As in the case of the constant flow rate $Pe = 1.0$, for $Pe = 5.0$, the degree of alignment increases as concentration N increases. Additionally, the characteristic behavior of $\mathbf{Q}_{xx}$ and $\mathbf{Q}_{xz}$ for $Pe = 5.0$ is also similar to that of the case $Pe = 1.0$. In Fig. 28, for higher concentrations of N and $\mathbf{Q}_{xx} < 0$ the solution is in its log-rolling state. As the concentration is decreased slightly, a phase transition occurs and the solution enters its **K1** flow phase which is marked by a change in sign of $\mathbf{Q}_{xx}$ from negative to positive. All other flow phases are marked by $\mathbf{Q}_{xx} > 0$. For $\mathbf{Q}_{xz} \neq 0$, one can see the transitions from in-plane, steady and periodic stable and log-rolling solutions, to out of plane stable periodic solutions.

IV.2.3 $N = 5.5$

For $N = 5.5$, the norm of $\mathbf{Q}$ and the components $\mathbf{Q}_{xx}$ and $\mathbf{Q}_{xz}$ are graphed. By selecting $N = 5.5$, the flow regions with smaller N values and the lowest Pe boundaries for the DQ closure scheme in (N, Pe) space can be identified The Leslie angle ϕ_L for $N = 5.5$ is discussed in a later section.

TABLE IX: Monodomain attractors and phase transitions vs shear rate Pe at fixed nematic polymer concentration $N = 5.5$ for the DQ closure scheme.

State	**LR**	**LR/W**	**K2/LR**	**K1/K2**
Pe Region	$(0, 0.61)$	$(0.61, 0.69)$	$(0.69, 0.73)$	$(0.73, 0.77)$
State	**K2**	**OS**	**FA**	
Pe Region	$(0.77, 1.40)$	$(1.40, 1.49)$	$(1.49, 10.00)$	

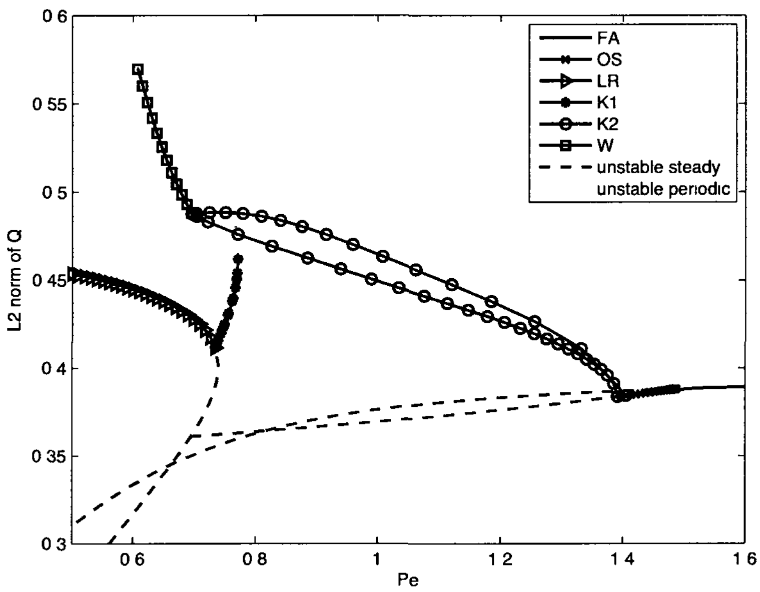

FIG. 29: L_2 norm of $\mathbf{Q}$ for DQ closure rule along with its phase transitions at $N = 5.5$.

At $N = 5.5$, every flow type the DQ closure scheme simulates is identified, except for **T**. Table IX gives a detailed description of the stable phase transitions, while Fig. 29 graphs the L_2 norm of $\mathbf{Q}$ along with its phase transitions. At $Pe = 0$, the solution is **LR** until the simulation enters a period of bi-stability at $Pe = 0.61$ with

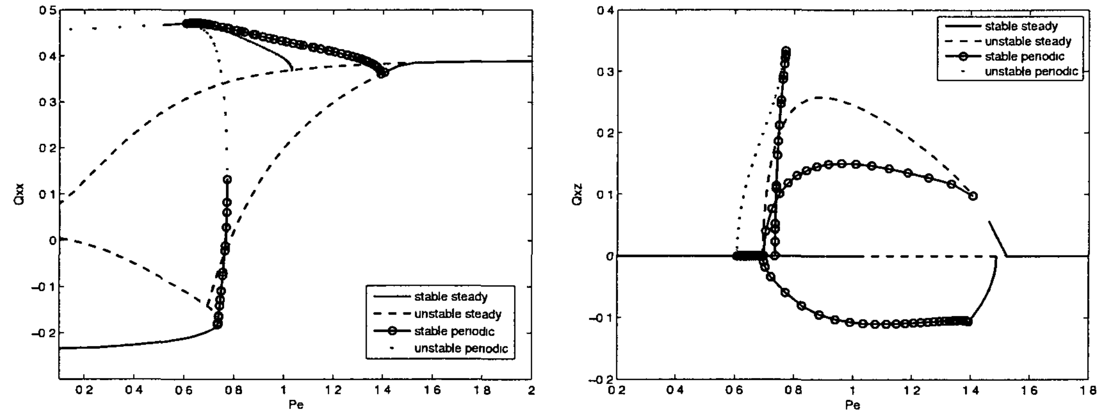

FIG. 30: Components $\mathbf{Q}_{xx}$ and $\mathbf{Q}_{xz}$ vs Pe for $N = 5.5$ from simulation with DQ closure rule. Left: $\mathbf{Q}_{xx}$. Right: $\mathbf{Q}_{xz}$.

the birth of the in-plane periodic **W** flow phase. With a slight increase in the shear flow strength, the periodic solution undergoes a phase transition into out-of-plane periodic **K2** flow at $Pe = 0.69$. Another slight increase in the shear flow strength results in the cessation of the **LR** flow phase and the birth of the **K1** flow phase at the HB point, $Pe = 0.73$. The simulation remains bi-stable until $Pe = 0.77$, when the **K1** solution becomes unstable. At $Pe = 1.40$, there is a HB point which denotes the end of stable periodic **K2** flow and the start of the **OS** solution. The **OS** region is very narrow which corresponds to the behavior of the kinetic solution [1]. At $Pe = 1.49$, the last phase transition in the domain $0 \leq Pe \leq 10.0$ occurs for $Pe = 1.49$ with the change from **OS** to **FA**. This result is also in agreement with the kinetic solution over the same domain [1].

The behaviors of components $\mathbf{Q}_{xx}$ and $\mathbf{Q}_{xz}$ are depicted in Fig. 30. For low shear rates and $\mathbf{Q}_{xx} < 0$, the solution is in its log-rolling state. As Pe is increased slightly, a phase transition occurs and the solution enters its **K1** flow phase which is marked by a change in sign of $\mathbf{Q}_{xx}$ from negative to positive. All other flow phases are marked by $\mathbf{Q}_{xx} > 0$. For $\mathbf{Q}_{xz} \neq 0$, one can see the transitions from in-plane, steady and periodic stable and log-rolling solutions, to stable out of plane steady and periodic solutions.

IV.2.4 $N = 6.0$

For $N = 6.0$, the norm of $\mathbf{Q}$ and the components $\mathbf{Q}_{xx}$ and $\mathbf{Q}_{xz}$ are graphed. By selecting $N = 6.0$, the flow regions with Pe boundaries near the center of the bifurcation diagram for the DQ closure scheme in (N, Pe) space can be identified. As noted in the previous section, the Leslie angle ϕ_L for $N = 6.0$ is discussed later.

TABLE X: Monodomain attractors and phase transitions vs shear rate Pe at fixed nematic polymer concentration $N = 6.0$ for the DQ closure scheme.

State	**LR**	**LR/W**
Pe Region	$(0, 1.18)$	$(1.18, 1.22)$
State	**K1/W**	**W**
Pe Region	$(1.22, 1.31)$	$(1.31, 10.0)$

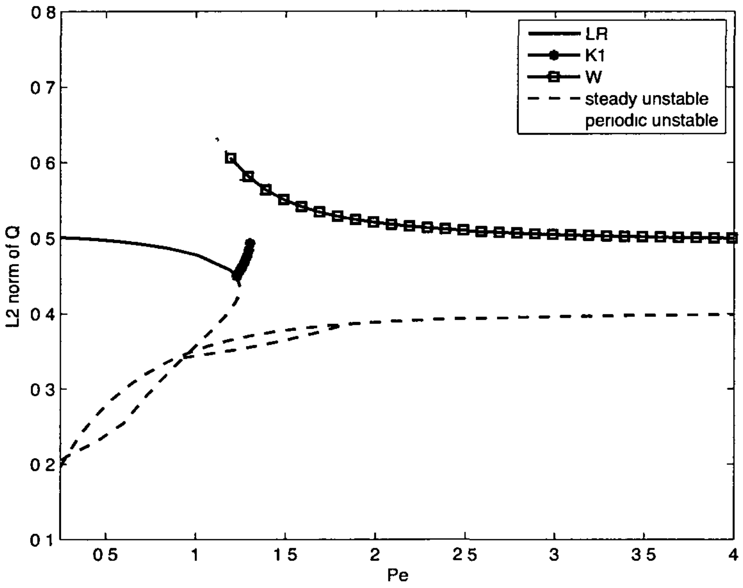

FIG. 31: L_2 norm of $\mathbf{Q}$ for DQ closure rule along with its phase transitions at $N = 6.0$.

At $N = 6.0$, only three flow types are identified from the simulation with the DQ closure scheme. Table X gives a detailed description of the stable phase transitions, while Fig. 31 graphs the L_2 norm of $\mathbf{Q}$ along with its phase transitions. At $Pe = 0$,

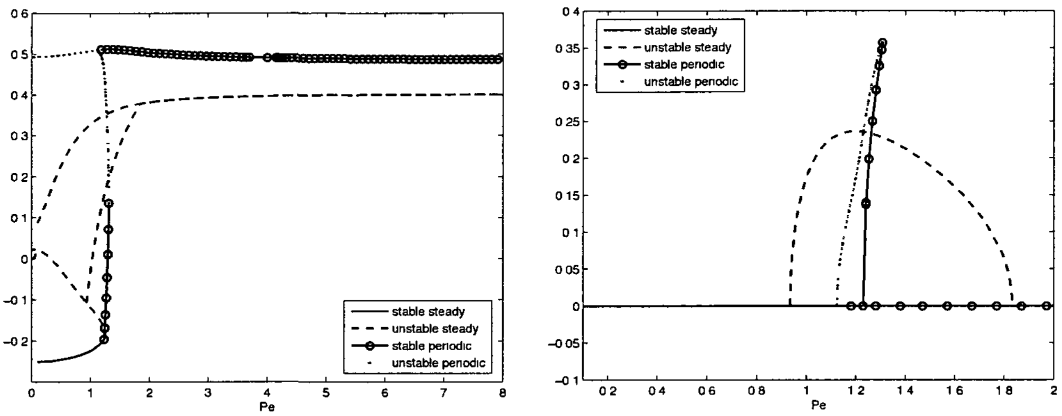

FIG. 32: Components $\mathbf{Q}_{xx}$ and $\mathbf{Q}_{xz}$ vs Pe for $N = 6.0$ from simulation with DQ closure rule. Left: $\mathbf{Q}_{xx}$. Right: $\mathbf{Q}_{xz}$.

the solution is **LR** until the simulation enters a period of bi-stability at $Pe = 1.18$ with the birth of the in-plane periodic **W** flow phase. A slight increase in the shear flow strength results in the cessation of the **LR** flow phase and the birth of the **K1** flow phase at the HB point, $Pe = 1.22$. The simulation remains bi-stable until $Pe = 1.31$, when the **K1** solution becomes unstable. In the remainder of the domain, $1.31 \leq Pe \leq 10.0$, the stable solution from DQ closure scheme is **W**. This result is not agreement with the kinetic solution over the same domain [1]. Of most significance is that the solution does not return to a stable **FA** state as the shear strength is increased.

The behaviors of components $\mathbf{Q}_{xx}$ and $\mathbf{Q}_{xz}$ are depicted in Fig. 32; they are similar to that of the case $N = 5.5$. For low shear rates and $\mathbf{Q}_{xx} < 0$ the solution is in its log-rolling state. As Pe is increased slightly, a phase transition occurs and the solution enters its **K1** flow phase which is marked by a steep change in the value of $\mathbf{Q}_{xx}$ from negative to positive. All other flow phases are marked by $\mathbf{Q}_{xx} > 0$. For $\mathbf{Q}_{xz} \neq 0$, one can see the transitions from in-plane periodic stable and log-rolling solutions to stable out of plane periodic solutions.

IV.2.5 $N = 8.0$

For $N = 8.0$, the norm of $\mathbf{Q}$ and the components $\mathbf{Q}_{xx}$ and $\mathbf{Q}_{xz}$ are graphed. By selecting $N = 8.0$, the all flow regions for the far left of the bifurcation diagram for the DQ closure scheme in (N, Pe) space can be identified.

TABLE XI: Monodomain attractors and phase transitions vs shear rate Pe at fixed nematic polymer concentration $N = 8.0$

State	**LR**	**LR/T**	**K1/T**
Pe Region	$(0, 4.59)$	$(4.59, 4.79)$	$(4.79, 5.44)$
State	**T**	**W**	
Pe Region	$(5.44, 5.84)$	$(5\ 84, 10.0)$	

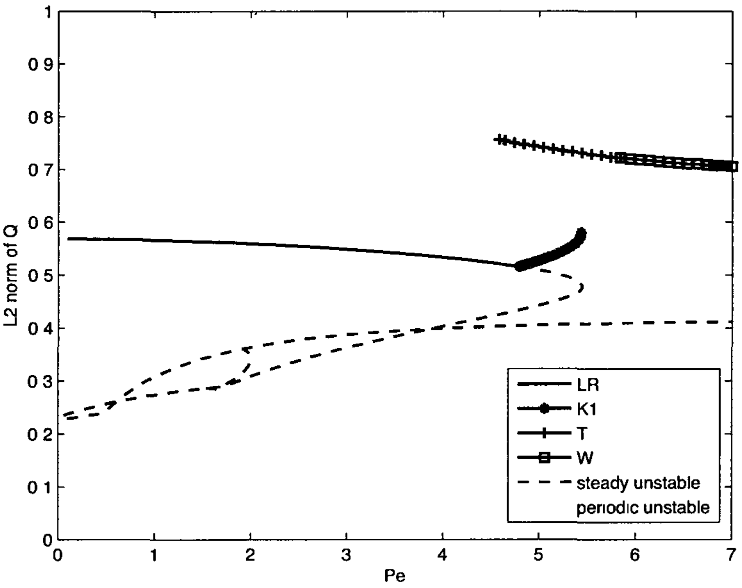

FIG. 33: L_2 norm of $\mathbf{Q}$ for DQ closure rule along with its phase transitions at $N = 8.0$.

At $N = 8\ 0$, four flow types are identified from the simulation with the DQ closure scheme. The results are similar to those for $N = 6.0$, with the addition of a **T** flow phase. Table XI gives a detailed description of the stable phase transitions, while Fig. 33 graphs the L_2 norm of $\mathbf{Q}$ along with its phase transitions. At $Pe = 0$, the solution is **LR** until the simulation enters a period of bi-stability at $Pe = 4.59$ with the birth of the in-plane periodic **T** flow phase. A slight increase in the shear flow strength results in the cessation of the **LR** flow phase and the birth of the **K1** flow phase at the HB point, $Pe = 4\ 79$. The simulation remains bi-stable until

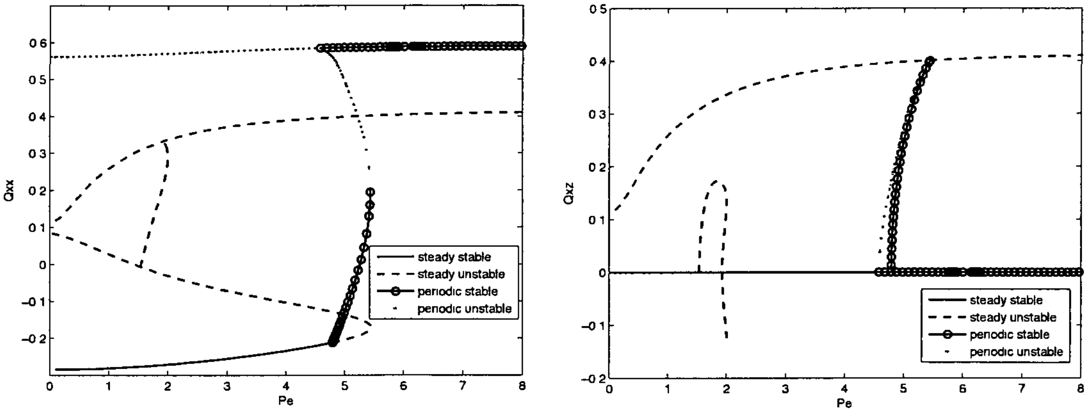

FIG. 34: Components $\mathbf{Q}_{xx}$ and $\mathbf{Q}_{xz}$ vs Pe for $N = 8.0$ from simulation with DQ closure rule. Left: $\mathbf{Q}_{xx}$. Right: $\mathbf{Q}_{xz}$.

$Pe = 5.44$, when the **K1** solution becomes unstable. In the remainder of the domain, $5.44 \leq Pe \leq 10.0$, the stable solution from DQ closure scheme is periodic in-plane. As the shear flow strength is increased, the amplitude of the periodic rotation decreases until the **T-W** transition occurs at $Pe = 5.84$, resulting in stable **W** flow phase. As in the simulation for $N = 6.0$, this result is not agreement with the kinetic solution over the same domain [1], due to the failure of the DQ simulation to return to a stable **FA** state as the shear strength is increased.

The behaviors of components $\mathbf{Q}_{xx}$ and $\mathbf{Q}_{xz}$ are depictedIn Fig. 34; they are in agreement with the results of the previous cases. For low shear rates and $\mathbf{Q}_{xx} < 0$ the solution is in its log-rolling state. After a significant increase in the shear rate value, Pe, a phase transition occurs and the solution enters its **K1** flow phase, marked by a rapid change in sign of $\mathbf{Q}_{xx}$ from negative to positive. All other flow phases are marked by $\mathbf{Q}_{xx} > 0$. For $\mathbf{Q}_{xz} \neq 0$, one can see the transitions from in-plane periodic stable and log-rolling solutions to stable out of plane periodic solutions.

IV.3 THE TUMBLING-WAGGING TRANSITION

The tumbling to wagging transition (**T-W**) occurs when the largest two eigenvalues of $\mathbf{Q}$ are equal. It is marked by a decrease in the rotation of ϕ from 180^o, the tumbling phase, to less than 180^o, the wagging phase. In order to capture this transition, the differential equation for $\mathbf{Q}$ as a function of time (9) must be solved. The initial conditions are $t_0 = 0$ and $\mathbf{Q}_0 = s(\mathbf{n}\mathbf{n}^T - \frac{1}{3}\mathbf{I})$. For any value of N around which the **T-W** transition occurs, the corresponding value of the order parameter s is given by the equilibrium diagram for the given closure (see Fig. 3). Additionally, since at $t_0 = 0$ the differential equation is in a state of equilibrium, $\theta = 90^o$ and $\phi = 0^o$, resulting in $\mathbf{n} = (1, 0, 0)$ from (20).

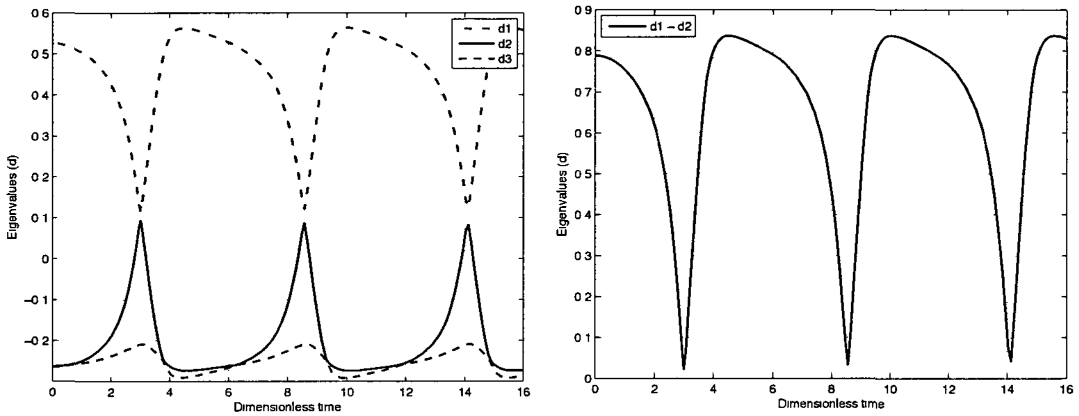

FIG. 35: The eigenvalues from the solution of $\frac{d\mathbf{Q}}{dt}$ for $N = 6.8$ from simulation with DQ closure rule during the tumbling phase. Left: Individual eigenvalues, d_1, d_2, d_3. Right: Difference in the first and second eigenvalues, $d_1 - d_2$.

The differential equation for $\mathbf{Q}$ (9) was solved using MATLAB's ODE15s ordinary differential equation solver. The nematic concentration is set to $N = 6.8$, resulting in $s = .789$ for the DQ closure (see Fig. 3). AUTO does not detect the **T-W** transition. In order to capture it, three different increasing shear rate values are chosen to depict **T**, **T-W**, and **W** phases respectively, while N remains constant. For each shear rate, the differential equation is solved for $\mathbf{Q}$ and its eigenvalues are graphed as a function of time. Fig. 35 depicts the tumbling solution of the DQ closure at $N = 6.8$ and $Pe = 2.3$. It can be seen that the largest two eigenvalues are close but not equal, $d_1 - d_2 = 0.04$. As the shear rate is increased to $Pe = 2.44$, the tumbling-wagging transition occurs, as detailed in Fig. 36. The largest two eigenvalues are equal to 1.0 and $d_1 - d_2 = 0$. Subsequently, as the shear rate is increased to $Pe = 2.6$, the largest two eigenvalues are no longer equal and $d_1 - d_2 = 0.05$, marking the flow transition into the wagging phase for $N = 6.8$ as depicted in Fig. 37.

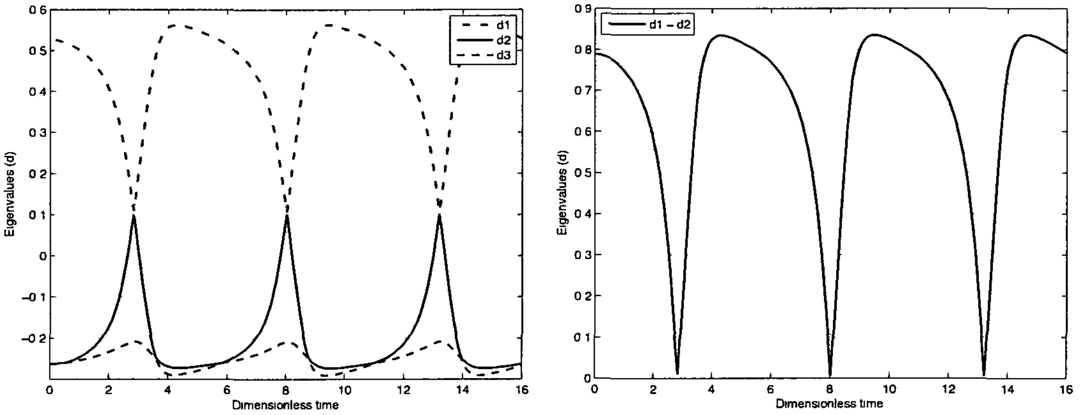

FIG. 36: The eigenvalues from the solution of $\frac{dQ}{dt}$ for $N = 6.8$ from simulation with DQ closure rule during the tumbling-wagging transition. Left: Individual eigenvalues, d_1, d_2, d_3. Right: Difference in the first and second eigenvalues, $d_1 - d_2$.

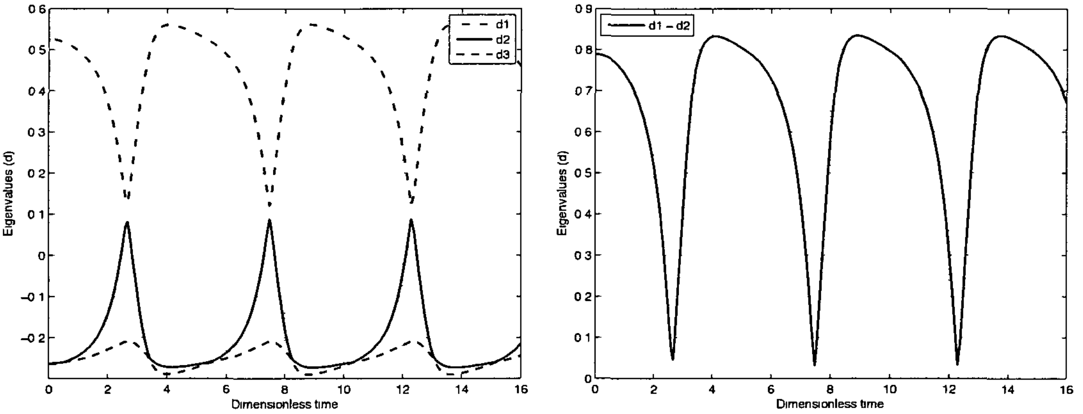

FIG. 37: The eigenvalues from the solution of $\frac{dQ}{dt}$ for $N - 6.8$ from simulation with DQ closure rule during the wagging phase. Left: Individual eigenvalues, d_1, d_2, d_3. Right: Difference in the first and second eigenvalues, $d_1 - d_2$.

TABLE XII: Stable states for each region in the DQ closure rule bifurcation diagram, Fig. 38, labeled from I to X.

Region	Stable states	Region	Stable states
I	**FA**	VI	**W/LR**
II	**OS**	VII	**LR**
III	**K2**	VIII	**T/LR**
IV	**W**	IX	**T/K1**
V	**W/K1**	X	**T**

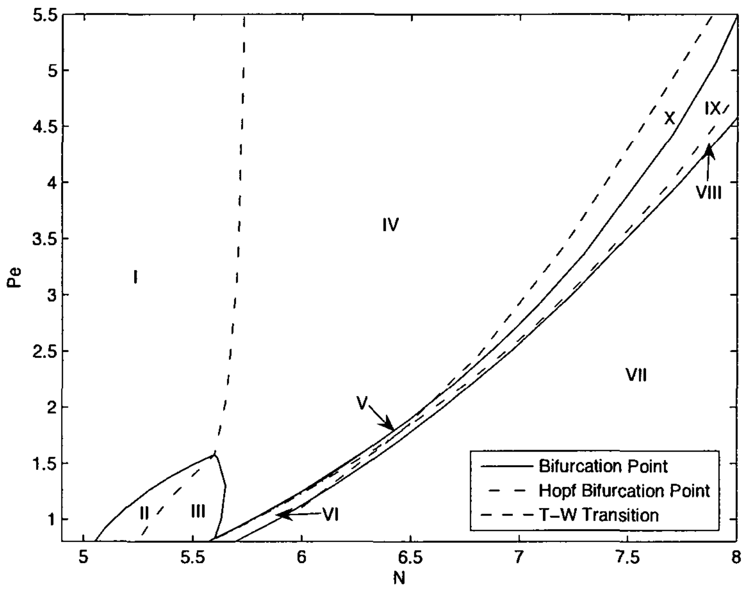

FIG. 38: Bifurcation diagram of stable states in (N, Pe) space for DQ closure. Table XII lists stable state(s) for each region labeled from I to X.

IV.4 BIFURCATION DIAGRAM FOR DQ CLOSURE RULE

Using AUTO bifurcation software, the bifurcation diagram for the DQ closure rule is generated by varying the parameters for the nematic concentration and the Peclet number from $4.6 \leq N \leq 8.5$ and $0 \leq Pe \leq 10$, respectively. As previously explained, after the bifurcation lines are drawn, a sampling of N and Pe values are selected so that each region of the bifurcation diagram is covered by a constant Pe value and a constant N value. The characteristic flow regions for these select N and Pe values are determined using the methods detailed in the previous two sections. Using the flow regions for each constant N or Pe value, the type of flow is determined for each stable region of the bifurcation diagram in (N, Pe) space. Additionally, by choosing a representative sample of N and Pe values from the basic bifurcation diagram, one can ensure that all regions of the bifurcation diagram are correctly identified in terms of flow types and boundaries. The regions are labeled I through X in the DQ closure rule bifurcation diagram, Fig. 38. The corresponding stable flow states are listed in Table XII. Note that the diagram represents bifurcations in the region $4.8 \leq N \leq 8.0$ and $.8 \leq Pe \leq 5.5$.

TABLE XIII: Stable states for each region in the bifurcation diagram, Fig. 39, from the kinetic simulation labeled from I to XIII [1].

Region	Stable states	Region	Stable states
I	**FA**	VIII	**K1/W**
II	**OS**	IX	**K1**
III	**K1/CH**	X	**W**
IV	**CH**	XI	**W/LR**
V	**T/LR**	XII	**LR**
VI	**K2**	XIII	**K1/T**
VII	**K1/K2**		

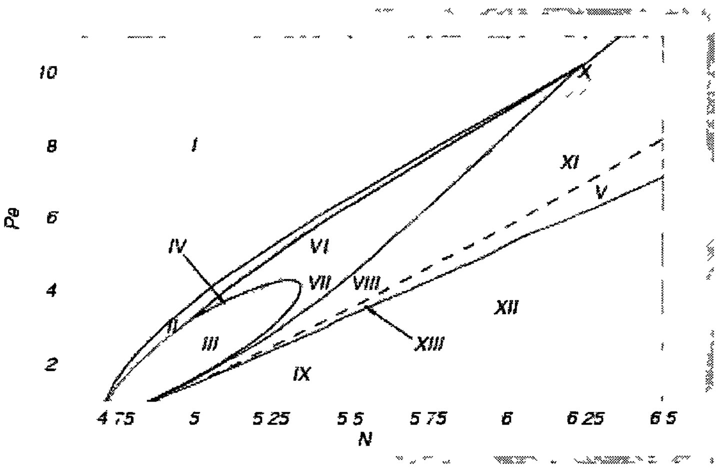

FIG. 39: Bifurcation diagram of stable states in (N, Pe) space for kinetic simulation [1]. Table XIII lists stable state(s) for each region labeled from I to XIII.

Courtesy of Forest, Wang, and Zhou [1], the bifurcation diagram for the kinetic simulation in AUTO is reprinted in Fig. 39 with the corresponding description of its flow regions in Table XIII. In comparison with the bifurcation diagram from the kinetic theory, from Fig. 38 it can be seen that the DQ closure rule fails to predict that for high *Pe* and *N*, the solution is FA. The cause of this is the asymptotic line of Hopf bifurcations at $N = 5.75$. While this is a significant shortcoming for the proposed closure rule, it is not unique among closure rules. It has been shown that the Bingham closure rule exhibits similar behavior [7]. It has an asymptotic Hopf bifurcation line at $N = 5.86$ and therefore fails to return to a steady stable **FA** state for high *Pe* and *N* values. Additionally, the DQ closure also fails to simulate chaos (**CH**). Chaos occurs when a periodic doubling bifurcation point spurs a second periodic doubling bifurcation point which spurs another periodic doubling bifurcation, and so on.

The bifurcations in the DQ closure rule happen at much lower Pe values than the bifurcations in the kinetic solution. This, along with the presence of the asymptotic Hopf bifurcation of make it difficult to do a side by side comparison of the flow region in the bifurcation diagrams of stable states in (N, Pe) space for the kinetic solution and the proposed DQ closure rule. However, a more general comparison can be made if each diagram is broken up into quadrants. For the kinetic solution, consider $N = 6.0$ and $Pe = 6.0$ to be your dividing lines. For the DQ solution, consider $N = 7.0$ and $Pe = 3.0$ to be your dividing lines. For the quadrant with *N* and *Pe* small, both the kinetic solution and the closure scheme contain **FA**, **OS**, **K1**, **K2**, and **W** flow regions. The kinetic solution also has **T** and **LR** regions. For the quadrant with *N* small and *Pe* large, the kinetic solution demonstrates **FA**, **OS**, **W**, **K1** and **K2** behavior, while the DQ solution demonstrates **FA** and **W** behavior. For the quadrant with *N* large and *Pe* large, both bifurcation diagrams of stable states contain **LR**, **T**, **W**, and **K1** regions. However, the DQ closure scheme fails to capture the **FA**, **OS**, and **K2** behavior that the kinetic solution demonstrates. For the quadrant with *N* small and *Pe* large, both bifurcation diagrams of stable states contain **T** and **LR** regions. The DQ closure scheme also has a small **K1** region.

IV.5 COMPARISON OF FLOW CHARACTERISTICS FOR SEVERAL CONCENTRATIONS

In this section, the normal stress differences and apparent viscosity of the solutions simulated with the DQ closure are computed for each flow type detected by the proposed closure, as denoted in Fig. 38 and Table XII. The resulting data is graphed as a function of Pe and compared to the known behavior of the kinetic solution [1].

The extra stress in dimensional form is given by [1,8,14]

$$\begin{aligned}\tau = (\eta_0 + 3\nu kT\zeta_3)\mathbf{D} + 3a\nu kT[\mathbf{Q} - N(\mathbf{Q} + \frac{\mathbf{I}}{3})\mathbf{Q} + N\mathbf{Q} : \langle \mathbf{mmmm} \rangle] \\ + 3\nu kT[\zeta_1(\mathbf{DM} + \mathbf{MD}) + \zeta_2 \mathbf{D} : \langle \mathbf{mmmm} \rangle] \quad (50)\end{aligned}$$

where ν_0 is the isotropic viscosity, $\zeta_n, n = 1, 2, 3$ are free parameters determined experimentally, and ν is the molecular number density.

The first and second normal stress differences N_1 and N_2, and the apparent viscosity η are given by

$$\begin{aligned} N_1 &= \tau_{xx} - \tau_{yy} \\ N_2 &= \tau_{yy} - \tau_{zz} \\ \eta &= \tau_{xy}/Pe \qquad (51) \end{aligned}$$

In the calculations for the normal stress differences N_1 and N_2 and the apparent viscosity η, the free parameters are set to $\zeta_1 = 0$, $\zeta_2 = 0.1$, and $\zeta_3 = 0.001$, which are consistent with infinite-aspect ratio rod-like nematic polymers and prior research of the kinetic solution [1].

The order parameters, d_1, d_2, d_3, for the flow-aligning and log-rolling solutions from the proposed closure rule will be calculated. The resulting data is used to capture the degree of alignment, characterized by d_1 as a function of shear rate Pe, as well as the maximum birefringence, characterized by $d_1 - d_3$, and the degree of biaxiality, characterized by $d_2 - d_3$ [1,8,13]. Additionally, the Leslie alignment angles will be calculated for the flow-aligning phase alone. By looking at theses flow characteristics for multiple concentrations, the general behavior of the simulation with the DQ closure rule can be observed and compared to that of the kinetic solution.

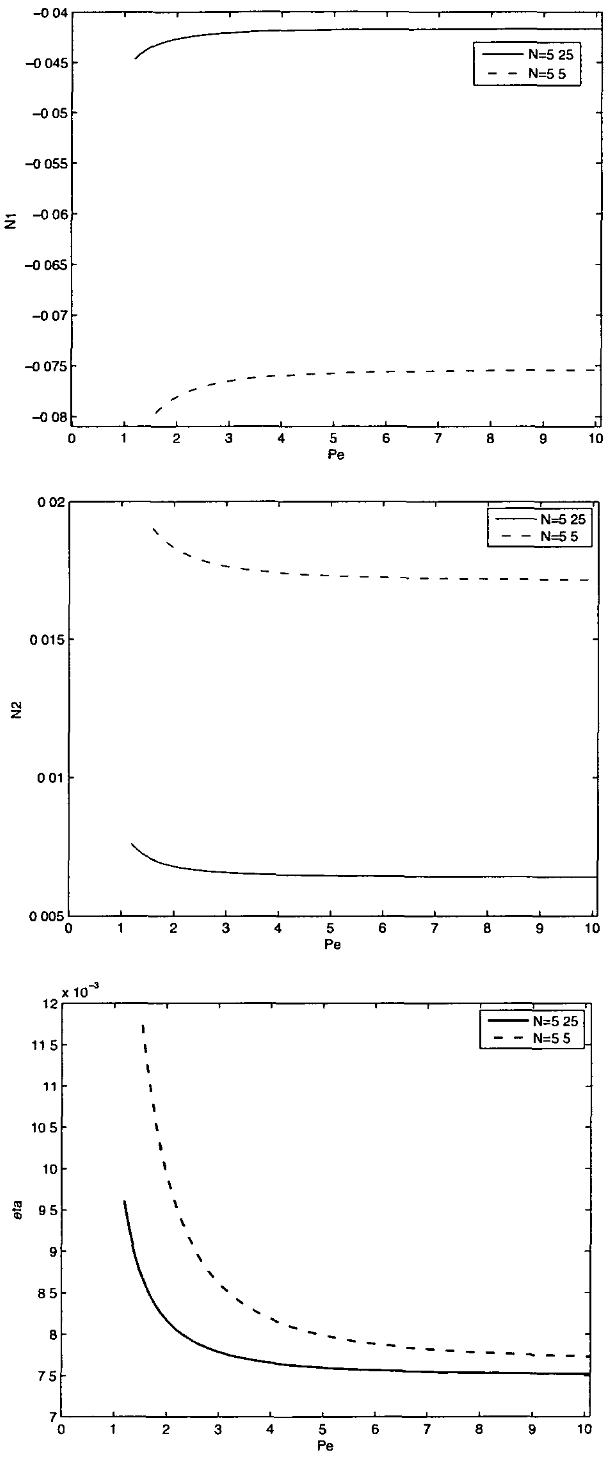

FIG. 40: Normal stress differences and apparent viscosity for flow-aligning (**FA**) stable states. Top: First normal stress difference N_1. Center: Second normal stress difference N_2. Bottom: Apparent viscosity η.

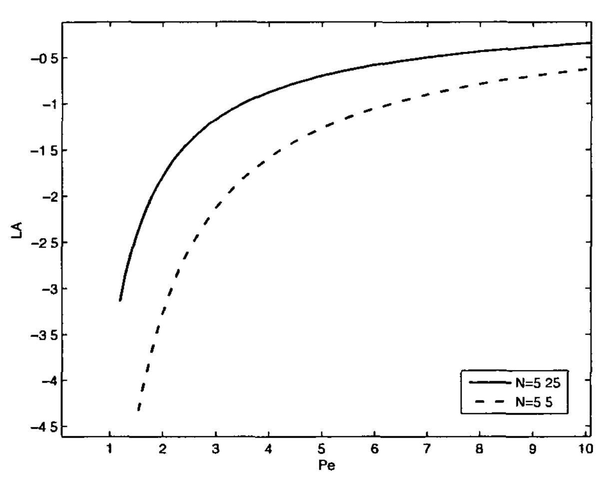

FIG. 41: Leslie alignment angle for flow-aligning (**FA**) stable states.

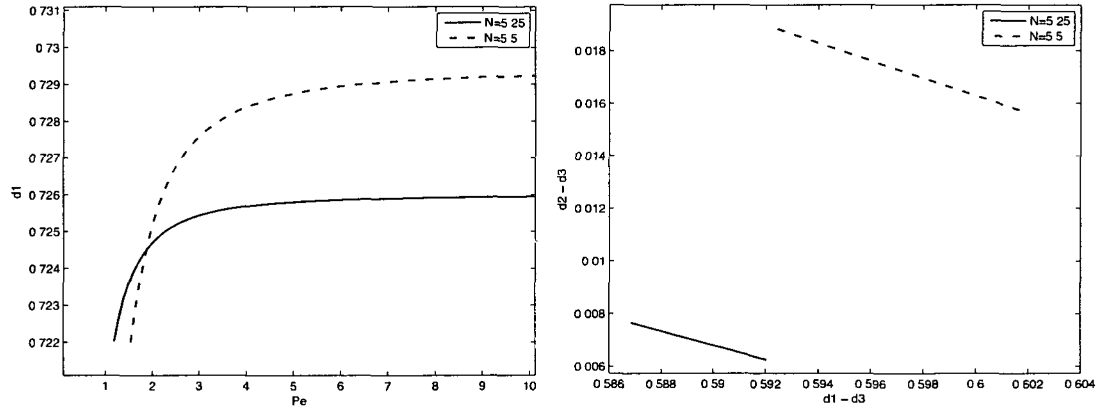

FIG. 42: Order parameters for flow-aligning (**FA**) stable states. Left: Degree of alignment d_1. Right: Maximum birefringence, $d_1 - d_3$, and the degree of biaxiality, $d_2 - d_3$, where Pe increases as $d_1 - d_3$ increases.

IV.5.1 Flow aligning

For the kinetic solution of the Smoluchowski differential equation, the **FA** state exists for any N and sufficiently high Pe. However, it has been shown that the DQ closure rule has an asymptotic region for $N > 5.75$, where the solution does not return to a **FA** state (see Fig. 38). Therefore, the study of the normal stress differences, N_1 and N_2 and apparent viscosity η is limited to the non-asymptotic region $N < 5.75$ for this flow phase.

Fig. 40 describes the normal stress differences and the apparent viscosity for the flow aligning state of the solution generated with the DQ closure scheme at $N = 5.25$ and $N = 5.5$. As Pe increases, N_1 increases and N_2 and η decrease, which is in agreement with the kinetic solution. For the kinetic solution, N_1 is positive for low polymer concentration, and negative for high polymer concentration [1]. While in Fig. 40, N_1 is negative for both $N = 5.25$ and $N = 5.5$, the value of N_1 decreases as the polymer concentration increases.

Fig. 41 and Fig. 42 depicts the Leslie alignment angle and order parameters for the flow aligning state at the concentrations $N = 5.25$ and $N = 5.5$. As Pe increases, the Leslie alignment angle, ϕ_L, increases. Note, that $\phi_L < 0$ in Fig. 41, but from Fig. 9, Fig. 15, Fig. 22, and Fig. 26, it is shown that for smaller concentrations, $\phi_L \geq 0$. Additionally, by examining all of these figures, it can be concluded that ϕ_L is generally small for high shear rates, $Pe \geq 1$, in the stable flow aligning phase. Lastly, the order parameters for the flow aligning states at the concentrations $N = 5.25$ and $N = 5.5$. are given in Fig. 42. The graph on the left shows the degree of alignment, d_1, as a function of shear rate Pe. As Pe increases, the degree of alignment increases. The graph on the right shows the maximum birefringence, $d_1 - d_3$, and the degree of biaxiality, $d_2 - d_3$. Pe increases as the maximum birefringence increases and the degree of biaxiality decreases. All of these results are in agreement with the behavior of the kinetic solution [1].

IV.5.2 Out of plane steady

For both the kinetic solution of the Smoluchowski differential equation and the solution generated from the DQ closure scheme, the **OS** state exists for only a narrow band of (N, Pe) space. From the examination of Fig. 38, the study of the normal stress differences, N_1 and N_2 and apparent viscosity η is limited to the region

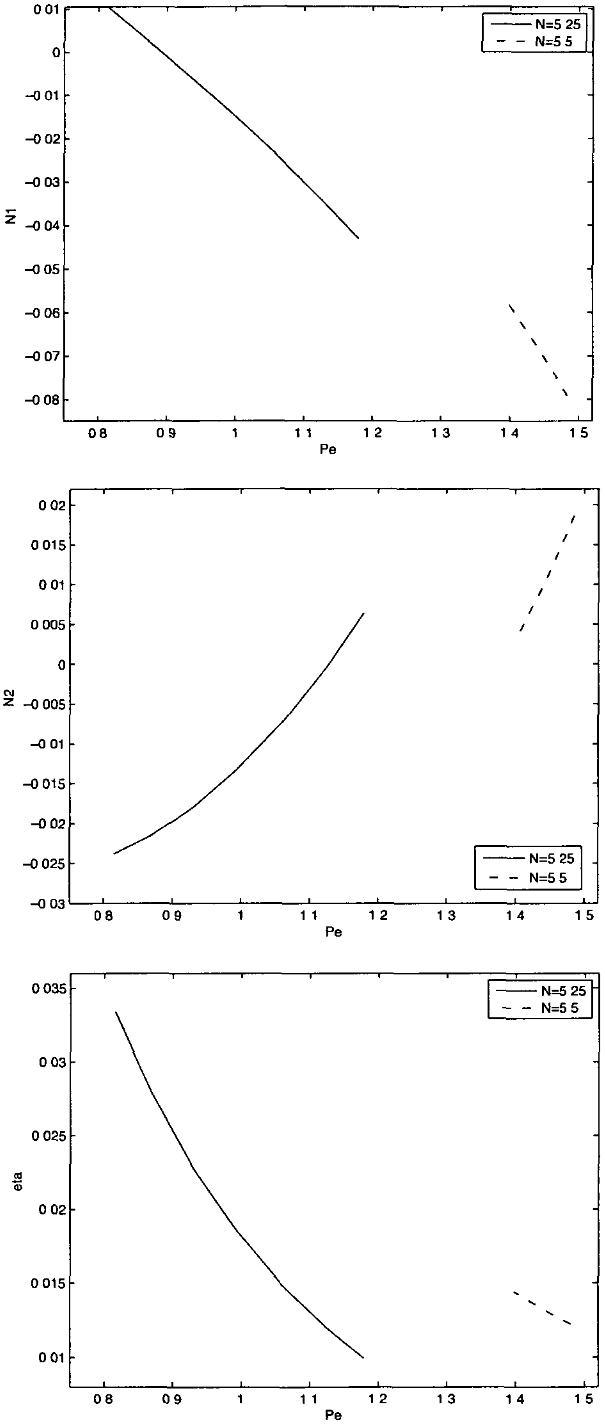

FIG. 43: Normal stress differences and apparent viscosity for out-of-plane steady (**OS**) stable states. Top: First normal stress difference N_1. Center: Second normal stress difference N_2. Bottom: Apparent viscosity η.

$5.2 \leq N \leq 5.5$ for $Pe \leq 2$.

Fig. 43 describes the normal stress differences and the apparent viscosity for the out-of-plane steady state of the solution generated with the DQ closure scheme at $N = 5.25$ and $N = 5.5$. As Pe increases, N_1 and η decrease, while N_2 increases. For the kinetic solution, as Pe increases, N_1 decreases, while N_2 and η increase. Additionally, the phase transition from **FA** to **OS** in the kinetic solution is characterized by a local minimum of N_1 and local maximums of N_2 and η [1]. Again, the behavior of N_1 and N_2 from the DQ closure simulation are in agreement with the kinetic solution, while the phase transition for **FA** to **OS** in the DQ closure simulation is not characterized by a local minimum or maximum of η.

IV.5.3 Logrolling

Fig. 44 describes the normal stress differences and the apparent viscosity for the log-rolling state of the solution generated with the DQ closure scheme at $N = 5.25$, $N = 5.5$, and $N = 6.0$. As Pe increases, N_1 increases, while N_2 and η decrease. For the kinetic solution, as Pe increases, N_1, N_2, and η increase. In both the kinetic and DQ case, the change in η as Pe increases in small. Additionally in the kinetic solution, $N_1 > 0$ an $N_2 > 0$ [1]. Thus, the behavior of N_1 from the DQ closure simulation is in agreement with the kinetic solution, while N_2 and η are not.

Fig. 45 depicts the order parameters for the log-rolling state of the solution at $N = 5.25$, $N = 5.5$, and $N = 6.0$. The graph on the left shows the degree of alignment, d_1, as a function of shear rate Pe. As Pe increases, the degree of alignment decreases. The graph on the right shows the maximum birefringence, $d_1 - d_3$, and the degree of biaxiality, $d_2 - d_3$. Pe increases as the degree of biaxiality increases, since all nematic equilibria ($Pe = 0$) are uniaxial [1]. The maximum birefringence initially increases with an increase of shear rate, but then there is a steady decline in the value $d_1 - d_3$ until a transition into the **K1** flow phase (see Fig. 29, Fig. 31, Fig. 38). All of these results are in agreement with the behavior of the kinetic solution [1].

IV.5.4 Kayaking

Fig. 46 describes the normal stress differences and the apparent viscosity for the kayaking **K1** and **K2** states of the solution generated with the DQ closure scheme at $N = 5.25$, $N = 5.5$, and $N = 6.0$, and $N = 5.25$ and $N = 5.5$, respectively. As Pe increases, N_1 and η decrease for both the **K1** and **K2** flow phase, while N_2

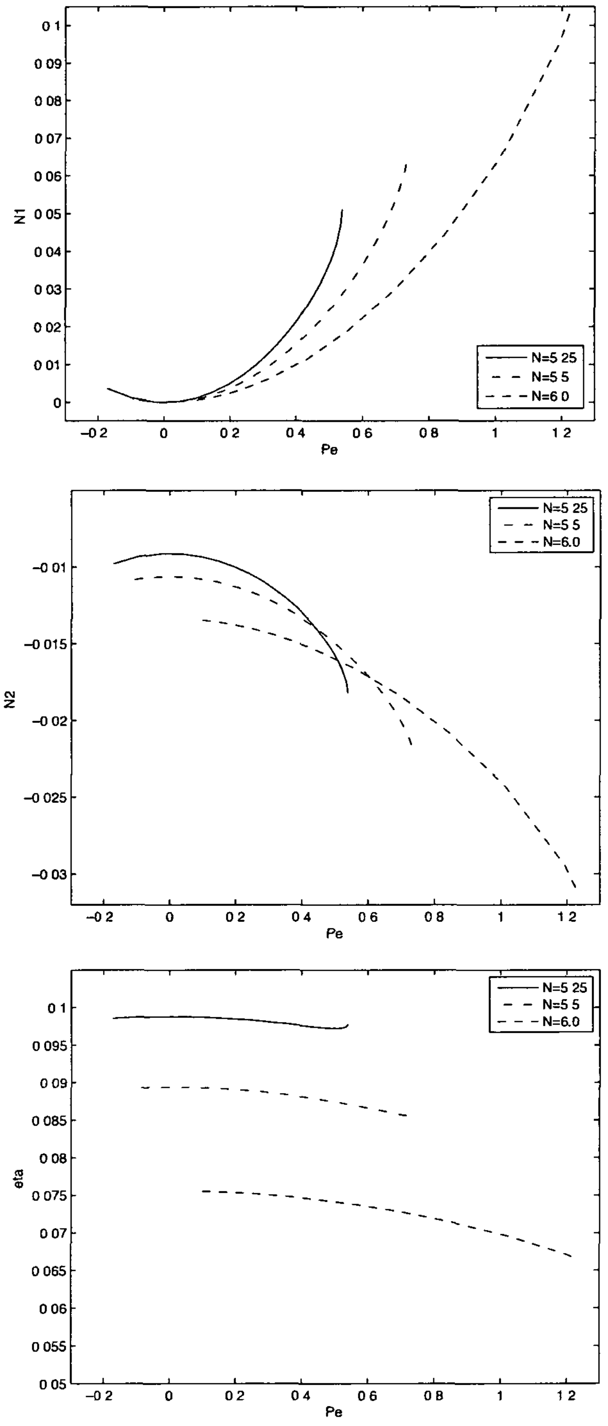

FIG. 44: Normal stress differences and apparent viscosity for logrolling (**LR**) stable states. Top: First normal stress difference N_1. Center: Second normal stress difference N_2. Bottom: Apparent viscosity η.

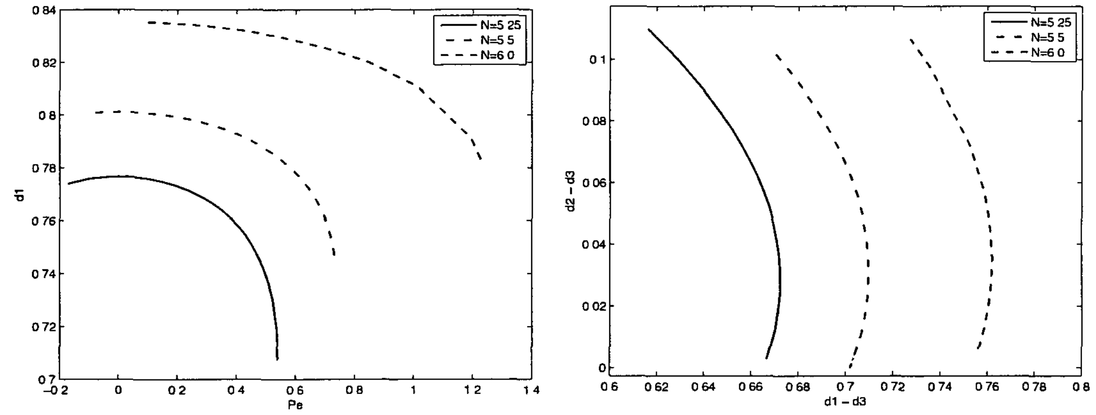

FIG. 45: Order parameters for the logrolling (**LR**) stable states. Left: Degree of alignment d_1. Right: Maximum birefringence, $d_1 - d_3$, and the degree of biaxiality, $d_2 - d_3$, where Pe increases as $d_2 - d_3$ increases.

increases for the **K1** flow phase and decreases for the **K2** flow phase. For the kinetic solution, as Pe increases, N_1 increases and N_2 decreases for both kayaking **K1** and **K2** phases, while η increases during the **K1** phase and decreases during the **K2** phase. Additionally, the phase transition from **OS** to **K2** in the kinetic solution is characterized by a local maximum of N_1 and local minimums of N_2 and η [1]. The behavior of N_2 from the DQ closure simulation are in agreement with the kinetic solution, while the phase transition for **OS** to **K2** in the DQ closure simulation is not characterized by a local minimum or maximum of N_1 or η; both are decreasing functions of Pe for both the **OS** and **K2** flow phase.

IV.5.5 Tumbling/Wagging

For the kinetic solution of the Smoluchowski differential equation, the tumbling and wagging states exists in a wide band of Pe for sufficiently large N (see Fig. 39), where for any given N, Pe has a finite range. In Fig. 38, it has been shown that the DQ closure rule has an asymptotic region for $N > 5.75$, where for some N in that region, Pe has an infinite range. Therefore, the study of the normal stress differences, N_1 and N_2 and apparent viscosity η is limited to the region around the asymptote $N = 5.75$ for this flow phase, where Pe is bounded.

Fig. 47 describes the normal stress differences and the apparent viscosity for the

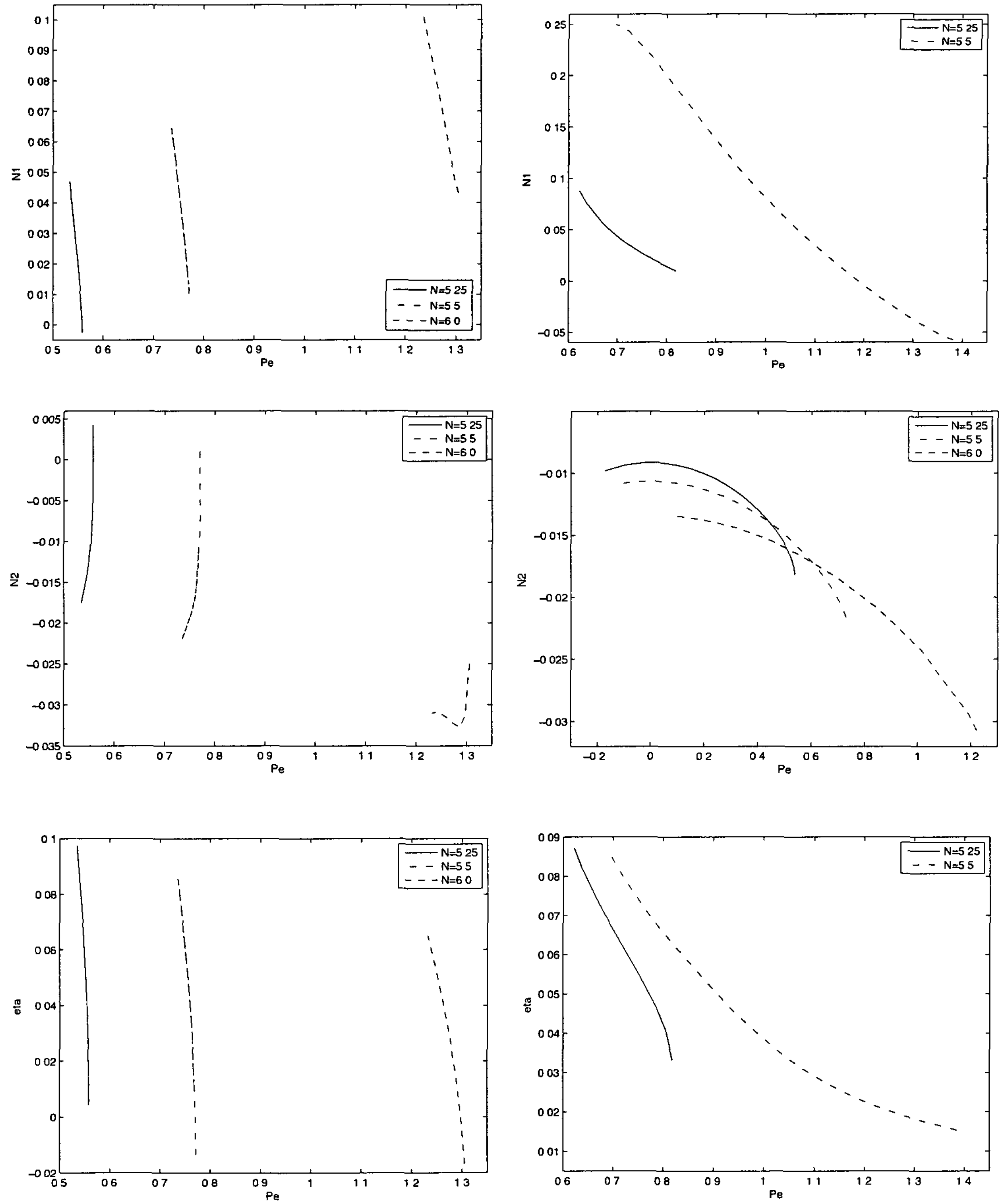

FIG. 46: Normal stress differences (N_1 and N_2) and apparent viscosity (η) for kayaking (**K1** and **K2**) periodic states. Left: **K1** attractor. Right: **K2** attractor.

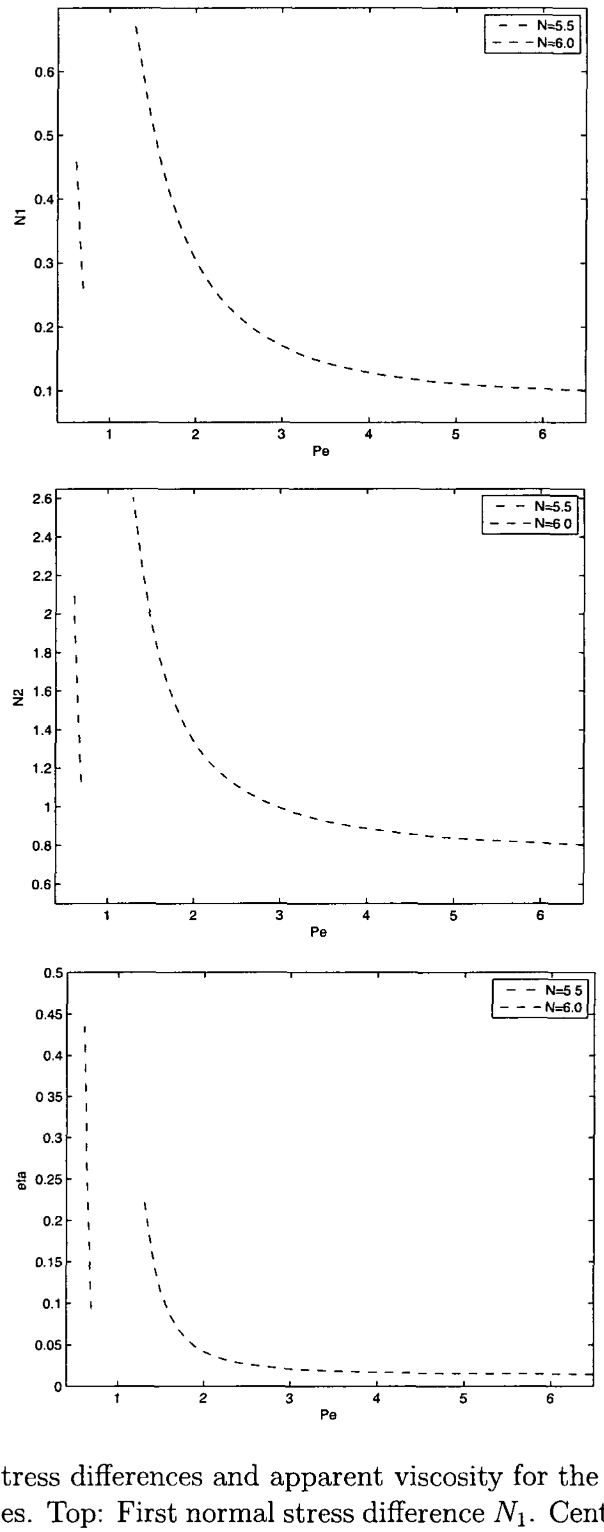

FIG. 47: Normal stress differences and apparent viscosity for the tumbling/wagging (**T/W**) stable states. Top: First normal stress difference N_1. Center: Second normal stress difference N_2. Bottom: Apparent viscosity η.

tumbling and wagging (**T/W**) steady states of the solution generated with the DQ closure scheme at $N = 5.5$ and $N = 6.0$. As Pe increases, N_1, N_2, and η decrease. Also, N_1, N_2, and η are all strictly positive. For the kinetic solution, as Pe increases, N_1 and η decrease, while N_2 increases. N_2 and η are strictly positive, while N_1 undergoes a sign change from positive to negative as the phases transition from tumbling to wagging [1]. While the DQ solution does simulate the phase transition from tumbling to wagging for $N = 6.0$, a sign change is not observed for N_1.

CHAPTER V

DQ CLOSURE IN PLANE COUETTE CELLS

In this chapter, the performance of the proposed DQ closure rule is studied under the condition of plane shear flow in Couette cells. In the first section, the model used to simulate the flow is described. In the following sections, the results from the simulation utilizing the DQ closure are presented. These findings are discussed along with other known results for simulations of liquid crystalline polymers in plane Couette cells.

V.1 MODEL FORMULATION IN PLANE COUETTE CELLS

The model being developed considers plane shear flow of large aspect ratio rod-like liquid crystalline polymers in a viscous solvent. Fig. 48 defines the coordinate system of the plane Couette cells, as well as the shear flow geometry. Here the liquid crystalline sample is placed between two large flat parallel plates located at $y = \pm h$, in Cartesian coordinates $\mathbf{x} = (x, y, z)$, giving a plate distance (or shear gap separation) of $2h$ [15,16,30]. Flow is induced by dragging the upper plate over the fluid with a constant velocity $\mathbf{v} = (v_0, 0, 0)$, while the lower plate moves in the opposite direction with constant velocity $\mathbf{v} = (-v_0, 0, 0)$. Variations in the direction of flow (x) and the vorticity direction (z), as well as transport in the vertical direction (y), are suppressed [15,16]. In accordance with (5) and Fig. 2, the rods are modeled as spheroids with axis of symmetry $\mathbf{m}$, whose PDF in time and across the shear gap is the primary focus.

There is an external and internal length scale in this problem, respectively the gap width $2h$ and the finite range l of molecular interaction, where l is the persistence length. The latter is set by the distortional elasticity in the Doi-Marucci-Greco (DMG) model. There are two time scales in the model as well. First, the bulk flow time scale ($t_0 = \frac{h}{v_0}$) that is set by the plates moving at a constant speed relative to each other. Secondly, the nematic time scale ($t_n = \frac{1}{D_r^0}$) which is set by the nematic average rotary diffusivity D_r^0. The ratio $\frac{t_n}{t_0}$ defines the Deborah number De [15,16]. There are also scales associated with solvent viscosity and three nematic viscosities, but they are not a priori known.

The DMG model is nondimensionalized using the length scale h, the time scale

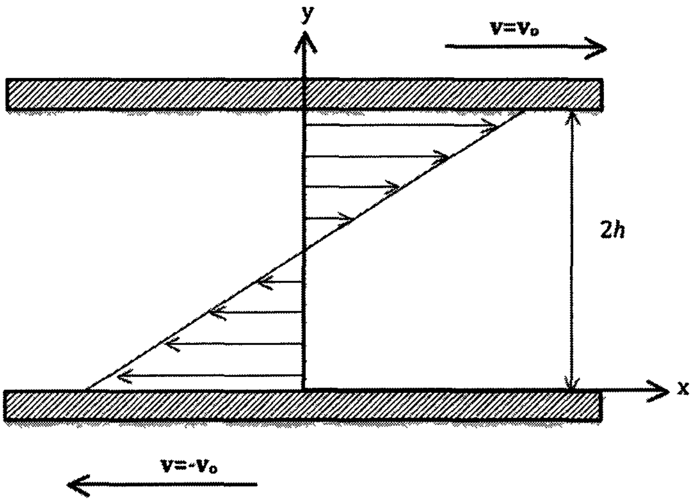

FIG. 48: Definition of Cartesian coordinate system and flow geometry for plane Couette cells. The liquid crystal sample is placed between two parallel plates, and is sheared by moving the top plate with a constant velocity $\mathbf{v}$. The gap separation is $2h$.

t_n, and the characteristic stress $\tau_0 = \frac{\rho h^2}{t_n^2}$, where ρ is the liquid density and p is a positive exponent less than one [15,16,31]:

$$\tilde{\mathbf{v}} = \frac{t_n}{h}\mathbf{v}, \quad \tilde{\mathbf{x}} = \frac{1}{h}\mathbf{x}, \quad \tilde{t} = \frac{t}{t_n}, \quad \tilde{\tau} = \frac{\tau}{\tau_0}, \quad \tilde{p} = \frac{p}{\tau_0}.$$

The following seven dimensionless parameters arise:

$$Re = \frac{\tau_0 t_n}{\eta}, \quad \alpha = \frac{3ckT}{\tau_0}, \quad Er = \frac{8h^2}{Nl^2}, \quad \mu_\imath = \frac{3ckT\zeta_\imath t_0}{t_n\tau_0}, \quad \imath = 1,2,3, \quad \theta = \frac{L^2}{\mathcal{L}^2},$$

where Re is the solvent Reynolds number; α measures the strength of entropic relative to kinetic energy (c is a number density of nematic molecules, k is the Boltzmann constant, and T is the absolute temperature); Er is the Ericksen number which measures short-range nematic potential strength relative to distortional elasticity strength depicted by the persistence length l; $\mu_\imath$, $\imath = 1,2,3$, are three nematic Reynolds numbers; and θ is a fraction between 0 and 1 that corresponds to equal ($\theta = 0$) or distinct ($\theta \neq 0$) elasticity constants [15,16]. The expression E^{-p}, $0 < p < 1$, is used represent a length scale spectrum that can predict passages to distortions with extremely high Ericksen numbers (on the order of tens of thousands) [16]. For other parameters, refer to [31]. For ease of reading, the tilde will be dropped on all variables. All figures correspond to normalized variables and length and time scales. The effect of translational diffusion is ignored, and instead the approximate rotary diffusivity is employed [2, 16].

In the case of plane Couette flow, the dimensionless Smoluchowski (kinetic) equation for the PDF $f = (\mathbf{m}, \mathbf{x}, t)$ is given by [16, 31]:

$$\frac{Df}{Dt} = \mathcal{R} \cdot [(\mathcal{R}f + f\mathcal{R}V)] - \mathcal{R} \cdot [\mathbf{m} \times \dot{\mathbf{m}} f], \tag{52}$$

with Jeffrey orbit $\dot{\mathbf{m}}$ (2). $\frac{Df}{Dt}$ is the material derivative $\frac{\partial}{\partial t} + \mathbf{v} \cdot \nabla$; $\mathcal{R}$ is the rotational gradient operator $\mathcal{R} = \mathbf{m} \times \frac{\partial}{\partial \mathbf{m}}$; $\mathbf{D}$ and $\mathbf{\Omega}$ (3) denote the symmetric and antisymmetric parts of $\nabla \mathbf{v}$ (or dimensionless rate-of-strain and vorticity tensors in the flow field $\mathbf{v}$). The second moment of the PDF, $\mathbf{M}$, and the Doi-Marucci-Greco potential, V, are [16, 31]:

$$\mathbf{M} = \mathbf{M}(f) = \int_{||\mathbf{m}||=1} \mathbf{m}\mathbf{m} f(\mathbf{m}, \mathbf{x}, t) d\mathbf{m}; \tag{53}$$

$$V = -\frac{3}{2} N \left[\left(\mathbf{I} + \frac{1}{3Er} \Delta \right) \mathbf{M} : \mathbf{m}\mathbf{m} + \frac{\theta}{3Er} \left(\mathbf{m}\mathbf{m} : (\nabla\nabla \cdot \mathbf{M}) \right) \right], \tag{54}$$

The dimensionless forms of the balance of linear momentum, the stress constitutive equation, and the continuity equation are [15, 16, 31]:

$$\frac{d\mathbf{v}}{dt} = \nabla \cdot (-p\mathbf{I} + \tau), \tag{55}$$

$$\begin{aligned} \tau = {} & \left(\frac{2}{Re} + \mu_3(a) \right) \mathbf{D} + a\alpha \left(\mathbf{M} - \frac{\mathbf{I}}{3} - N\mathbf{M} \cdot \mathbf{M} + N\mathbf{M} : \mathbf{M}_4 \right) \\ & - a\frac{\alpha}{6Er} \left(\Delta\mathbf{M} \cdot \mathbf{M} + \mathbf{M} \cdot \Delta\mathbf{M} - 2\Delta\mathbf{M} : \mathbf{M}_4 \right) \\ & - \frac{\alpha}{12Er} \left(2 \left(\Delta\mathbf{M} \cdot \mathbf{M} - \mathbf{M} \cdot \Delta\mathbf{M} \right) + \left(\nabla\mathbf{M} : \nabla\mathbf{M} - (\nabla\nabla\mathbf{M}) : \mathbf{M} \right) \right) \\ & - a\frac{\alpha\theta}{12Er} \left[\mathbf{M} \cdot \mathbf{M}_d + \mathbf{M}_d \cdot \mathbf{M} - 4(\nabla\nabla \cdot \mathbf{M}) : \mathbf{M}_4 \right] \\ & - \frac{\alpha\theta}{12Er} \left[\mathbf{M}_d \cdot \mathbf{M} - \mathbf{M} \cdot \mathbf{M}_d - (\nabla\nabla \cdot \mathbf{M}) \cdot \mathbf{M} + \mathbf{M}_{\beta\jmath,\alpha} \mathbf{M}_{\imath\jmath,\imath} \right] \\ & + \left[\mu_1(a) \left(\mathbf{D} \cdot \mathbf{M} + \mathbf{M} \cdot \mathbf{D} \right) + \mu_2(a) \mathbf{D} : \mathbf{M}_4 \right], \end{aligned} \tag{56}$$

$$\nabla \cdot \mathbf{v} = 0, \tag{57}$$

where $\mathbf{M}_d$ is a symmetrized second variation of $\mathbf{M}$ and $\mathbf{M}_4$ is the fourth moment of f,

$$\mathbf{M}_d = \nabla\nabla\cdot\mathbf{M} + (\nabla\nabla\cdot\mathbf{M})^T, \qquad \mathbf{M}_4 = \int_{||\mathbf{m}||=1} \mathbf{mmmm}f(\mathbf{m},\mathbf{x},t)d\mathbf{m}. \tag{58}$$

The dimensionless form for the orientation tensor $\mathbf{Q}$ is given as [15, 31]:

$$\begin{aligned}\frac{\partial\mathbf{Q}}{\partial t} &= \boldsymbol{\Omega}\cdot\mathbf{Q} - \mathbf{Q}\cdot\boldsymbol{\Omega} + a(\mathbf{D}\cdot\mathbf{Q} + \mathbf{Q}\cdot\mathbf{D}) + \frac{2}{3}a\mathbf{D} - 2a\mathbf{D}:\mathbf{M}_4 \\ &-6D_r\left(F(\mathbf{Q}) + \frac{1}{3Er}\left[\Delta\mathbf{Q}:\mathbf{M}_4 - \frac{1}{2}(\Delta\mathbf{Q}\cdot\mathbf{Q} + \mathbf{Q}\cdot\Delta\mathbf{Q}) - \frac{1}{3}\Delta\mathbf{Q}\right]\right)\end{aligned} \tag{59}$$

$$F(\mathbf{Q}) = \left(1 - \frac{N}{3}\right)\mathbf{Q} - N\mathbf{QQ} + N\mathbf{Q}:\mathbf{M}_4 \tag{60}$$

where D_r is the dimensionless rotational diffusion coefficient, which will be approximated [2]. In the stress constitutive equation (56) and the dimensionless equation for the orientation tensor (59), the fourth order tensor $\mathbf{M}_4$ appears. This term results in the second order system having a dependency on higher (fourth) order moments. Upon close inspection of (56) and (59), it can be seen that $\mathbf{M}_4$ does not need to be explicitly known; instead $\mathbf{D}:\mathbf{M}_4$, $\mathbf{Q}:\mathbf{M}_4$, and $\Delta\mathbf{Q}:\mathbf{M}_4$ must be determined. As in the case of simple shear flow, an approximation to the contractions in terms of lower (second) moments will be made by using the proposed DQ closure rule (18,19).

In this study, consideration is limited to one-dimensional space (the interval between the two plates). The boundary conditions [15, 16] for the velocity $\mathbf{v} = (v_x, 0, 0)$ are given by the Deborah number,

$$v_x(y = \pm 1) = \pm De. \tag{61}$$

Homogeneous anchoring at the plates is assumed, given by the quiescent stable nematic equilibrium

$$\mathbf{Q}|_{y=\pm 1} = s_0\left(\mathbf{nn} - \frac{\mathbf{I}}{3}\right), \tag{62}$$

where s_0 is determined from the bifurcation diagram for the DQ closure rule under equilibrium conditions, see Fig. 3 for details. $\mathbf{n}$ is the uniaxial order director, assumed to lie in the shear plane, at some experimentally dictated anchoring angle ψ_0 with respect to the flow direction,

$$\mathbf{n} = (\cos\psi_0, \sin\psi_0, 0). \tag{63}$$

The anchoring angle can be parallel ($\psi_0 = 0^o$), normal ($\psi_0 = 90^o$), or tilted ($0^o < \psi_0 < 90^o$) [15, 16, 30]. This study will focus only on parallel and normal anchoring.

Given the previously mentioned restrictions on the flow, such as the suppression of variations in the direction of flow (x) and the vorticity direction (z), as well as transport in the vertical direction (y), combined with the boundary conditions listed above, the momentum equation (55) reduces to a single equation for the velocity component v_x,

$$\frac{\partial v_x}{\partial t} = \frac{\partial \tau_{xy}}{\partial y}. \tag{64}$$

The expression for τ_{xy} in terms of the DQ closure scheme is given in the Appendix. By solving the coupled system of differential equations, (59) and (64), with the use of a closure approximation, a simulation can be executed.

V.2 SIMULATION IN PLANE COUETTE CELLS

In this section, the numerical methods used to solve the partial differential equations, (59) and (64), are explained, and the values of the fixed parameters are defined. The simulation is run under parallel and normal anchoring conditions. The Leslie angle, the peak orientation angle as a function of time, and the flow velocity (v_x) are studied for the in-plane flow states. Those results are used to compile a table of in-plane structure attractors and phase change for multiple decades of Deborah number (De) and Ericksen number (Er). Comparisons are made with known results for simulations of liquid crystalline polymers in plane Couette cells.

V.2.1 Structure formation – simulation parameters

As in the case of simple shear flow, for plane Couette flow the value of the molecular shape parameter (5) is restricted to $a = 1$. The nematic concentration is fixed to $N = 5.5$, which results in $s_0 = 0.685$ at equilibrium from Fig. 3. Other parameters include $Re = 100$, $\theta = 0$, $\alpha = 2$, $\mu_1 = 0.0004$, $\mu_2 = 0.15$, and $\mu_3 = 0.01$. All approximations to contractions of the form $\mathbf{A} : \mathbf{M}_4$ are done using the proposed DQ closure rule (18,19).

In the simulation, four distinct spatiotemporal attractors arise and are listed in Table XIV and Table XV. These include the elastic-driven steady state (**ES**), the viscous-driven steady state (**VS**), the composite tumbling-wagging periodic state (**TW**), and the wagging periodic state (**W**). The **ES** and **VS** attractors are characteristic of plane Couette flow and a detailed description of them is given in the next sections. The remainder of this chapter is a discussion of the content of Table XV.

TABLE XIV: Spatiotemporal attractors in plane Couette cells

ES:	elastic-driven steady state
VS:	viscous-driven steady state
TW:	composite tumbling-wagging periodic state
W:	wagging periodic state

TABLE XV: In-plane structure attractors and phase transitions for multiple decades of deborah number (De) and Ericksen number (Er) at fixed nematic polymer concentration $N = 5.5$ under parallel anchoring ($\psi = 0^o$) conditions with the DQ closure scheme.

De \ Er	**1**	**2**	**5**	**10**	**15**	**30**	**500**	**1000**	**5000**	**7000**	∞
0.05	ES	ES	ES	ES	ES	ES	ES	ES	W	W	T
0.1	ES	ES	ES	ES	ES	ES	ES	W	W	TW	T
0.5	ES	ES	ES	ES	ES	TW	TW	TW	TW	TW	T
1	ES	ES	ES	TW	TW	TW	TW	TW	TW	TW	T
3	ES	ES	TW	TW	TW	TW	TW	TW	TW	TW	T
5	ES	ES	W	W	W	W	W	W	W	W	W
6	ES	ES	W	W	W	W	W	W	W	W	W
8	ES	ES	ES	VS	VS	VS	VS	VS	VS	VS	FA
10	ES	ES	VS	VS	VS	VS	VS	VS	VS	VS	FA
12	ES	ES	VS	VS	VS	VS	VS	VS	VS	VS	FA

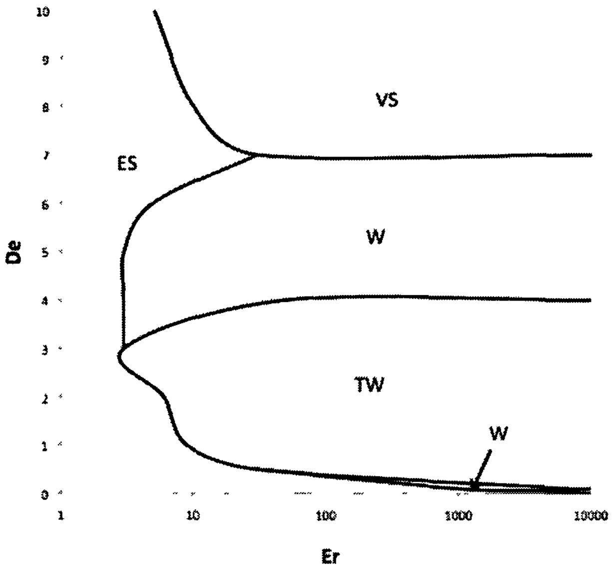

FIG. 49: Definition of Cartesian coordinate system and flow geometry for plane Couette cells. The liquid crystal sample is placed between two parallel plates, and is sheared by moving the top plate with a constant velocity $\mathbf{v}$. The gap separation is $2h$.

From inspection of Table XV and its accompanying graphical representation, Fig. 49, one can see the general relationship between Er and De values, and the flow regime. Plainly put, the Deborah number describes how fluid a material appears. The Ericksen number describe the deformation of the director field under flow. For Er sufficiently small, the **ES** steady state prevails for any De value; the elastic forces exceed the viscous forces and so the director field is not strongly affected by the flow field. In contrast, for polymers with De sufficiently large the material is highly fluid; the flow is strong enough that the rotational tendencies are dampened leading the **VS** steady state to prevail for sufficiently large Er. $Er = \infty$ corresponds to the monodomain simulations. Therefore, if the material is in a **ES** steady state as $Er \longrightarrow \infty$, it undergoes a phase transitions into a **FA** steady state, identical to the shear flow case. In the case were De is sufficiently small, increasing Er increases the rotational effects of the flow and the material undergoes a phase transition to the **W** or **TW** periodic flow regimes [3, 16, 30]. The characteristics of the **T**, **TW**, and **W** flow phases are similar to the monodomain case (see Fig. 35, 36, 37). The composite **TW** phase is a result of boundary effects, wherein the the oscillation near the boundaries will be less than 90^o resulting in **W**, but equal to 90^o in the middle of the plate resulting in **T**. As $Er \longrightarrow \infty$, if the material is in a **TW** phase, it transitions into a **T** phase as there is no boundary effect making it equivalent in structure to the shear flow tumbling attractor. From an in-plane periodic flow phase, increasing the De further leads to a phase transition to the **VS** steady state. These attractors are qualitatively consistent with previous research done by Tsuji and Rey [3,30] and Forest, Zhou, and Wang [16]. For normal anchoring conditions, a similar table can be constructed which will be quantitatively slightly different, but qualitatively the same as Table XV.

V.2.2 Structure formation – numerical method

TABLE XVI: Finite difference schemes

Derivative	Scheme	Formula of Discretization
1	2-point second-order central	$\frac{-f(y_{-1})+f(y_{+1})}{2\Delta y}$
2	3-point second-order central	$\frac{f(y_{-1})-2f(y_0)+f(y_{+1})}{(\Delta y)^2}$

As mentioned in the previous section, coupling (59), with (64) results in a system of partial differential equations. These are solved numerically by the method of lines (MOL) with a course finite difference grid, $n = 100$, in the space $-1 \leq y \leq 1$. In MOL, the partial differential equations are discretized with respect to space, resulting in a new system of ordinary differential equations with respect to time. This new system of ordinary differential equations can be solved using any sufficient numerical ODE solver.

The finite difference schemes for spatial derivatives from (3), (59), and (64), are described in the following. See Table XVI for a description of the discretization formulas used. $\Delta\mathbf{Q}$ is found by discretizing $\mathbf{Q}$ using a 3-point second-order central difference scheme for the second derivative, $\partial^2\mathbf{Q}/\partial y^2$. Recall, that any flow in the x or z direction is suppressed. $\nabla\mathbf{v}$ is discretized using a 2-point second-order forward difference scheme on a staggered grid for the first derivative $\partial v_x/\partial y$. The staggered grid is created by finding the midpoints between every pair of adjacent points on

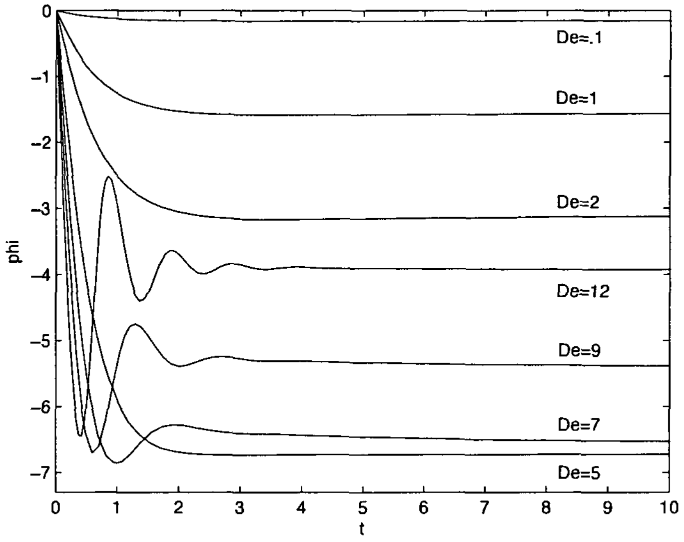

FIG. 50: Evolution of the peak orientation angle (ϕ) midway between the plate gap ($y = 0$) for $Er = 1$ and two decades of De, with parallel anchoring conditions at the plates ($\psi_o = 0^o$). The strong distortional elasticity at sufficiently low Er leads to steady structure attractors with relatively fast convergence to steady state, indicated by arrested motion at the mid-plane.

the current finite difference grid for y, and interpolating the velocity at those points if needed. This results in a "staggered" grid with a new array of velocity values corresponding to the midpoints of the spatial grid; it has one less element than the original velocity array. Similarly, τ_{xy} is discretized using a 2-point first-order forward finite difference scheme on a staggered grid for the first derivative $\partial\tau_{xy}/\partial y$. The resulting system of ODE's is solved using MATLAB's ode15s ordinary differential equation solver where the equilibrium behavior at $t = 0$ sets the initial conditions. ode15s, which is well suited for stiff ordinary differential equations like ours, utilizes a numerical differentiation formula with a variable time step.

V.2.3 Elasticity-dominated steady states (ES structure attractors)

The elastic driven steady state (**ES**) arrises when the spatial elasticity dominates; this occurs when the Ericksen number is sufficiently low and the value of the Deborah number is not huge. Here the elastic potential overwhelms the rotating effects due to viscous forces [16,30]. Fig. 50 through Fig. 52 focus on the peak orientation angle

ϕ of the PDF, associated with the major director of the nematic liquid. This PDF feature and subsequent related properties are computed from the second moment tensor $\mathbf{Q}$. As in the case of simple-shear flow, the eigenvector of $\mathbf{Q}$ corresponding to the largest eigenvalue signifies the major director, $\mathbf{n}_1$ (49). Within the confines of parallel and normal anchoring conditions, all steady solutions will be in-plane and therefore the major director takes the form

$$\mathbf{n}_1 = (\cos\phi, \sin\phi, 0). \tag{65}$$

The comparable shape distortions of the PDF are detected by the largest eigenvalue, d_1, of the major director [16].

Fig. 50 focuses on the evolution of the peak orientation angle (ϕ) at the center of the plate gap for $Er = 1$ and two decades of De, with parallel anchoring conditions at the plates ($\psi_o = 0^o$). The mid-plane orientation angle converges to a steady state at sufficiently low De, then acquires an oscillatory transient for $De > 5$. Of great interest is the fact that Forest, Zhou, and Wang [16] found $De > 5$ to be the point at which their solution acquired an oscillatory transient as well. The value of ϕ computed after the time of convergence to a steady state is the Leslie alignment angle (ϕ_L). Note the quick convergence time of 3 units for the peak orientation angle (ϕ) with $De \leq 5$. As time t approaches 3, for all De shown here, the transient oscillation shrinks until the entire gap becomes steady by $t = 5$. In the kinetic simulations, Forest, Zhou, and Wang [16] found that the entire gap became steady by $t = 3$. Qualitatively, the observations for these elasticity dominated steady states (**ES**) from simulations with the DQ closure scheme agree with the previous research [3, 16, 30].

Illustrations of De-dependent **ES** steady state structures across the plate gap are presented in Fig. 51 and Fig. 52. It is characteristic of the structure features of the **ES** attractors to be smoothly dependent [15, 16, 30]. In Fig. 51, the Leslie alignment angle (ϕ_L) is given for $Er = 1$ and a variety of De values under parallel anchoring conditions. The figure on the left is for relatively small Deborah numbers, $De = 1, 2, 3, 4, 5$; the figure on the right is for relatively large Deborah numbers, $De = 10, 12, 14, 17, 20$. These graphs illustrate that, for small De, the magnitude of ϕ_L increases as De is increased, up until the point at which the peak orientation angle acquires an oscillatory transient for $De > 5$ (see Fig. 50) . For $De > 5$, the magnitude of ϕ_L decreases as De values are increased. In their previous research, Forest, Zhou, and Wang [16] found that for sufficiently large De , $\phi_L \longrightarrow 0$. That does not seem to be an unreasonable assumption to make for the simulation with the

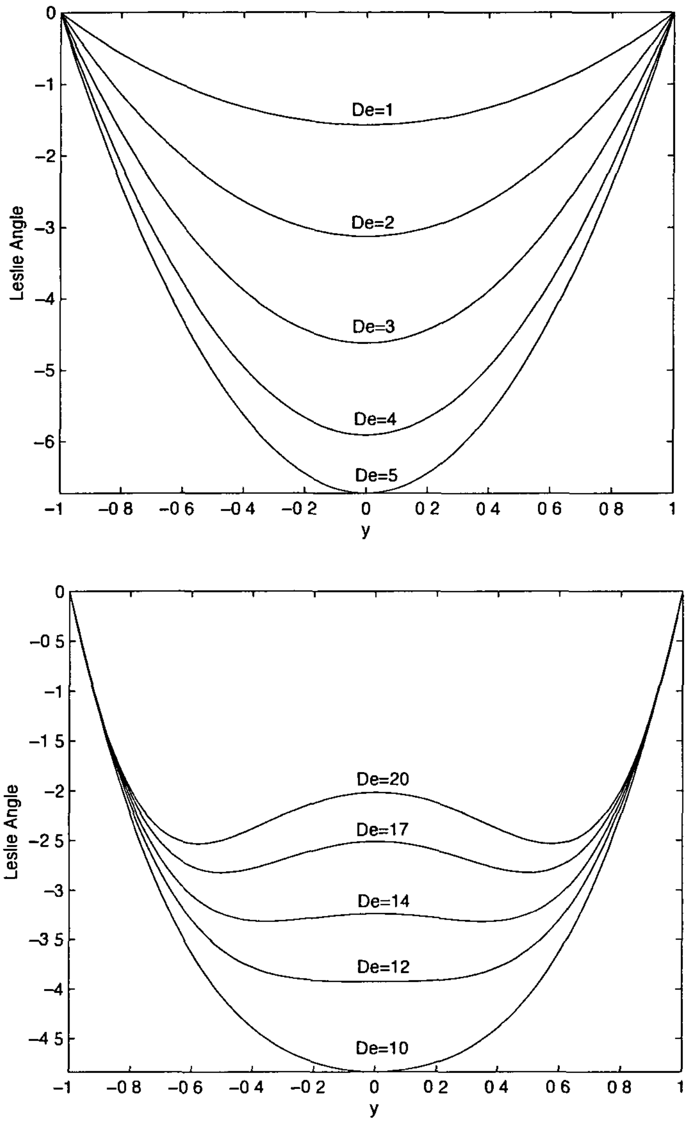

FIG. 51: Steady states for fixed small Ericksen number ($Er = 1$) and increasing Deborah number across the plate gap with parallel anchoring ($\psi_o = 0^o$).

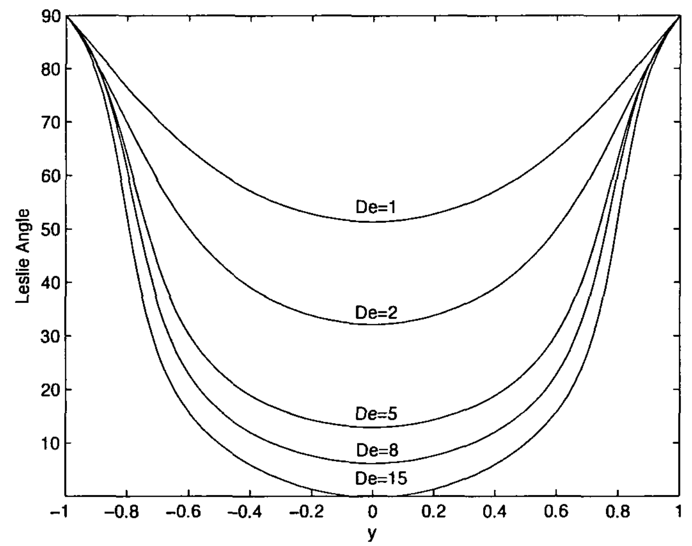

FIG. 52: Steady states for fixed small Ericksen number ($Er = 1$) and increasing Deborah number across the plate gap with normal anchoring ($\psi_o = 90^o$).

DQ closure scheme. Fig. 52 depicts ϕ_L for $Er = 1$ and increasing Deborah numbers, $De = 1, 2, 5, 8, 15$, under normal anchoring conditions. The figure shows that as De is increased, ϕ_L decreases; for sufficiently large De, $\phi_L \longrightarrow 0$.

The focus of this study on **ES** steady state flow now turns to the shape distortion of the PDF, referred to as the molecular elasticity. This is measured by the order parameter d_1, the largest eigenvalue of the major director, $\mathbf{n}_1$. This is an important feature for material properties, since the principal values of conductivity in a nematic polymer composite are directly correlated with the principal values of d_i of the PDF [16]. Recall, the eigenvalues (order parameters) describe the degree of alignment of the PDF with respect to the major director $\mathbf{n}_1$. The liquid crystalline polymer is in its isotropic phase when all eigenvalues are equal, $d_1 = d_2 = d_3 = 1/3$. Larger values of d_1 reflect focusing of the PDF around the major director. Some authors use $d_1 - d_2$, the Flory order parameter, which measures the maximum normalized birefringence [8, 13, 16]. Fig. 53 gives a representative shape distortion profile across the plate gap for $De = 2, Er = 1$ with parallel and normal anchoring, from Fig. 51 and Fig. 52 respectively. From the graph on the top of Fig. 53, one can see that the distortions are minor for parallel anchoring and are focused at the mid-gap of the plate. The graph on the bottom indicates that for normal anchoring conditions, there

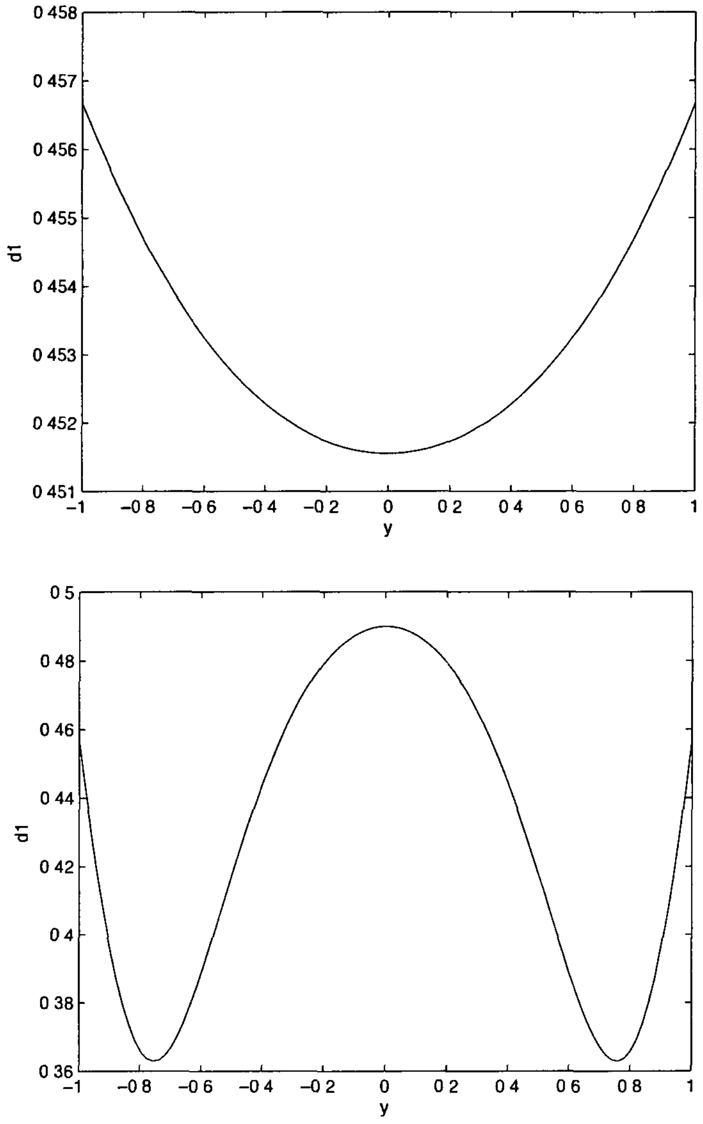

FIG. 53: Degree of alignment in **ES** steady state for $Er = 1$ and $De = 2$ across the plate gap. Top: parallel anchoring ($\psi_o = 0^o$). Bottom. normal anchoring ($\psi_o = 90^o$)

are notable distortions near the plate boundaries. Again, these results from the DQ closure simulations agree with the results from prior research on the subject [15, 16].

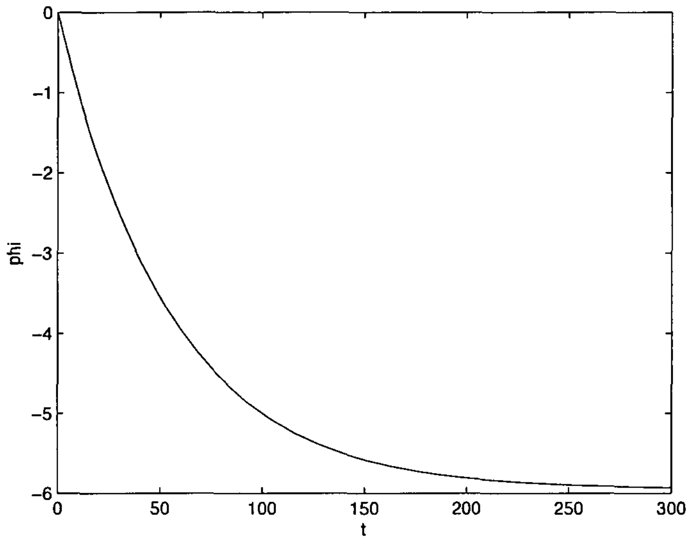

FIG. 54: Evolution of the peak orientation angle (ϕ) midway between the plate gap ($y = 0$) for $Er = 500, De = 0.05$ with parallel anchoring ($\psi_o = 0^o$).

Lastly, the study of the **ES** steady state with the DQ closure scheme is extended to the case of moderate Er values at sufficiently low De, as in the case of $Er = 500, De = 0.05$ shown in Fig. 54 and Fig. 55. In agreement with the results from prior research [16, 30], as the Ericksen number is increased, Fig. 54 shows that convergence to the steady state is extremely slow; Fig. 55 shows the smooth steady state structure characteristic of the **ES** attractor. However, the transition from the **ES** regime to the **TW** regime at sufficiently high Er values observed in the kinetic simulation for $De < 0.5$ [16], does not occur in the simulation with the DQ closure. Instead, the **ES** steady state transitions into a **W** periodic state (see Table XV and Fig. 49), and the **ES** regime exists for a much larger range of Er values at low Deborah numbers ($De < 0.5$) than in the kinetic simulation.

V.2.4 Viscous-dominated steady states (VS structure attractors)

The viscous driven steady state (**VS**) arises when the viscous driving forces induced by the moving plate overwhelm short range elasticity, which governs bulk monodomain dynamics. This occurs when the Deborah number is sufficiently high;

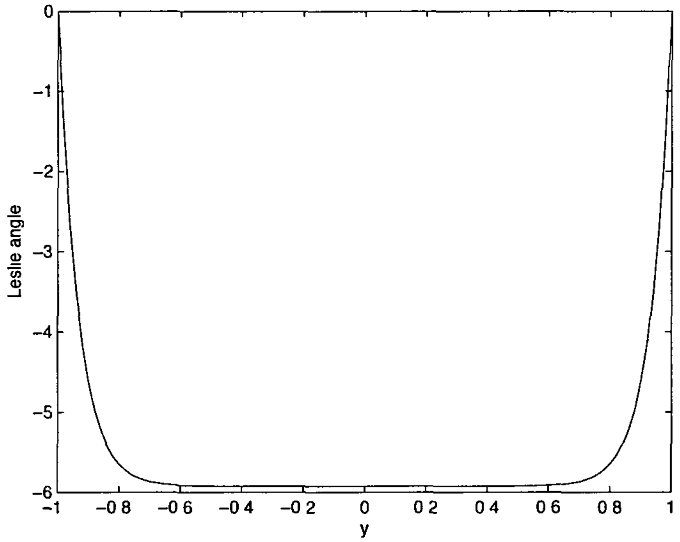

FIG. 55: Leslie alignment angle across the gap in the **ES** steady state for the same parameters for $Er = 500, De = 0.05$ with parallel anchoring ($\psi_o = 0^o$)

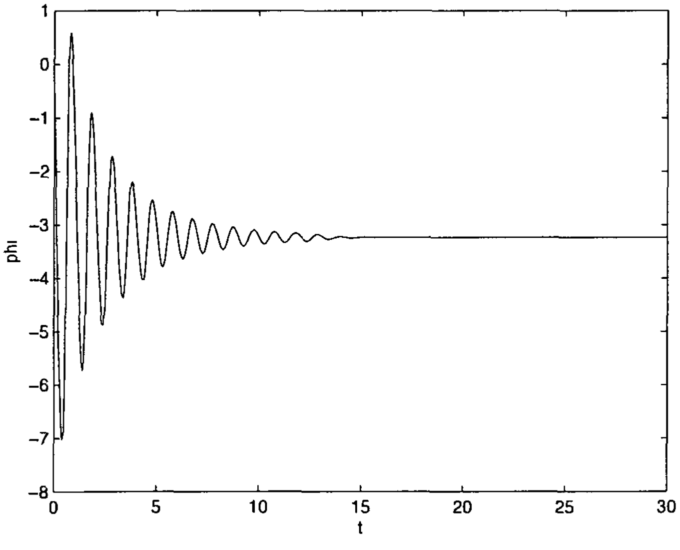

FIG. 56: Evolution of the peak alignment angle (ϕ) midway between the plate gap ($y = 0$) for $Er = 1000, De = 12$, with parallel anchoring conditions at the plates ($\psi_o = 0^o$). Convergence to steady state is indicated by arrested motion at the mid-plane.

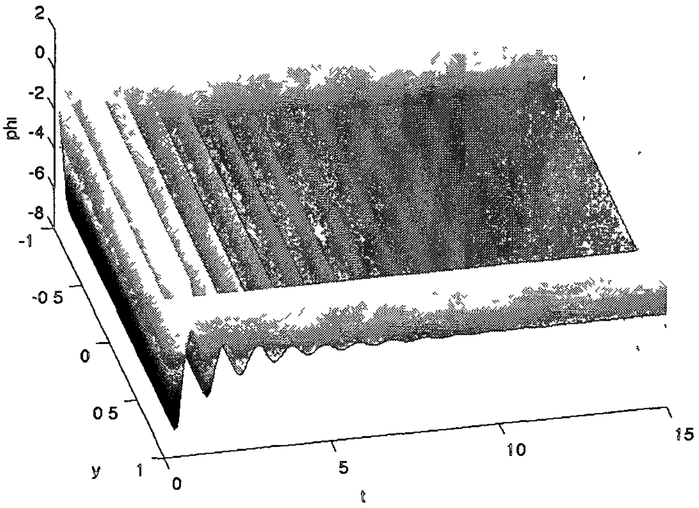

FIG. 57: Evolution of the peak alignment angle (ϕ) across the entire plate gap for $Er = 1000, De = 12$, with parallel anchoring conditions at the plates ($\psi_o = 0^o$).

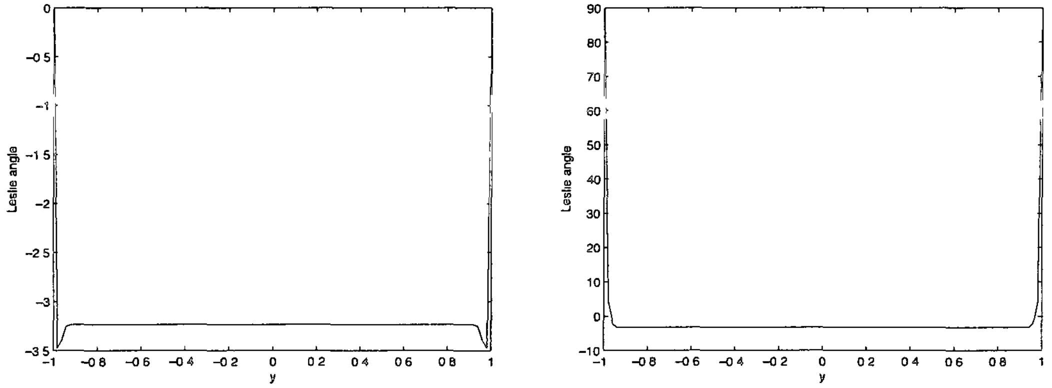

FIG. 58: Leslie alignment angle (ϕ_L) across the gap for $Er = 1000$, $De = 12$ with parallel anchoring ($\psi_o = 0^o$) and normal anchoring ($\psi_o = 90^o$). Left: Parallel anchoring. Right: Normal anchoring.

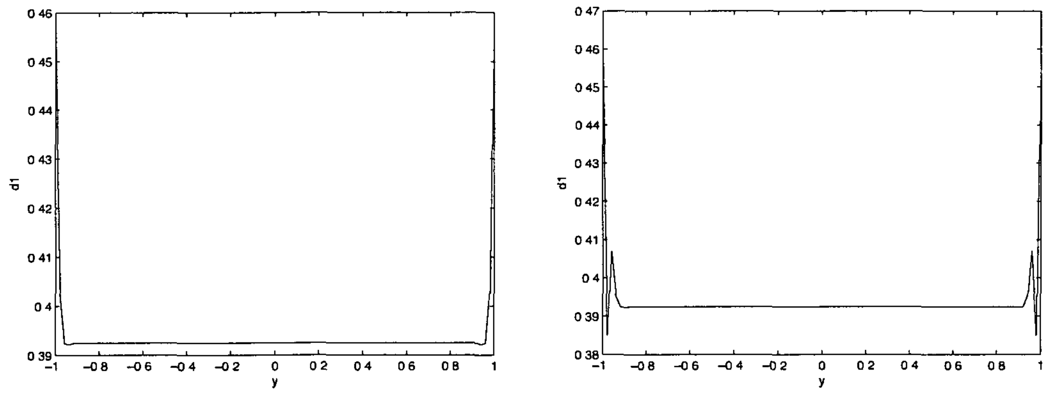

FIG. 59: Degree of alignment (d_1) across the gap in the **VS** steady state for $Er = 1000, De = 12$ with parallel anchoring ($\psi_o = 0^o$) and normal anchoring ($\psi_o = 90^o$). Left: Parallel anchoring. Right: Normal anchoring.

the molecular distribution at each gap height aligns along some preferred direction [16,30]. Fig. 56 shows the peak alignment angle ϕ of the PDF at the midpoint of the plate gap ($y = 0$), associated with the major director of the nematic liquid, for $Er = 1000$ and $De = 12$ with parallel anchoring at the plates. Alternatively, Fig. 57 displays the peak alignment angle ϕ of the PDF across the entire plate gap for the same parameter values, showing the dynamics of a coherent spatial structure. The underdamped oscillatory behavior of the peak orientation is characteristic of this regime [16,30], and convergence to a steady state is indicated by arrested motion at the mid-plane.

Fig. 58 displays the Leslie angle and degree of alignment for $Er = 1000$ and $De = 12$ with parallel and normal anchoring respectively, and Fig. 59 displays the degree of alignment (d_1) with parallel and normal anchoring for the same parameter values. Note the rapid changes near the boundary layers and the flat interior profile for both the peak axis (ϕ) and shape (d_1). These sharp boundary layers of the **VS** attractors provide a distinction from the **ES** regime where the director profile is parabolic. When comparing the parallel anchoring simulation to normal anchoring, the amplitude distortions in ϕ and d_1 are greater for the normal anchoring case, which is consistent with the results for Forest, Wang, and Zhou [16].

The steady state transition from the **ES** regime to the **VS** regime is explored in Fig. 60, with normal anchoring conditions and $De = 12$. The Ericksen number is

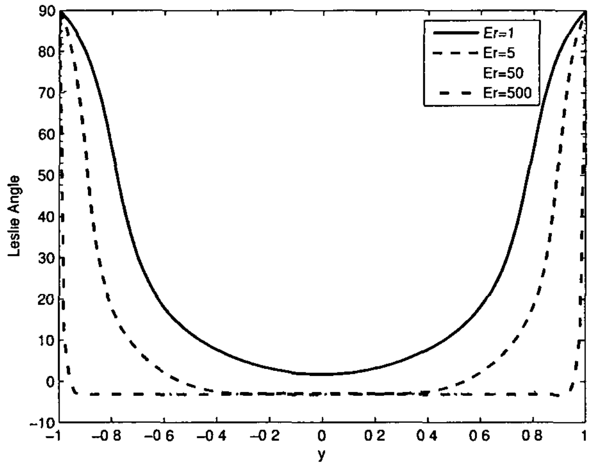

FIG. 60: Structure continuation profiles with fixed Deborah number ($De = 12$) and varying Er across the plate gap with normal anchoring. The nematic structure features of **ES** attractors at low Er develop sharp boundary layers at high Er, characteristic of **VS** attractors.

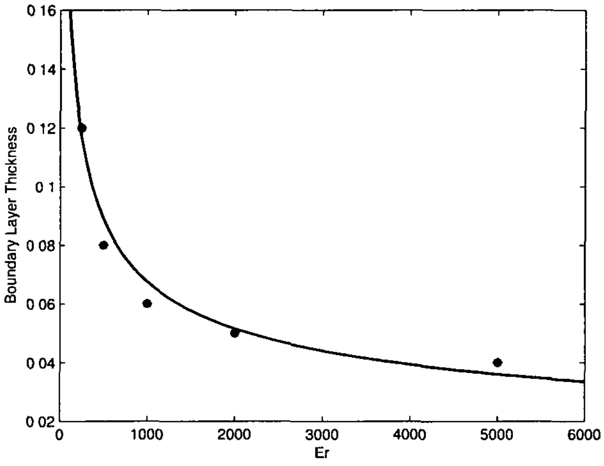

FIG. 61: The scaling behavior of the boundary layer thickness for $De = 12$ with normal anchoring. The solid line shows the exponential fit, $Er^{-0.39}$, of the discrete dots from the closure rule simulation.

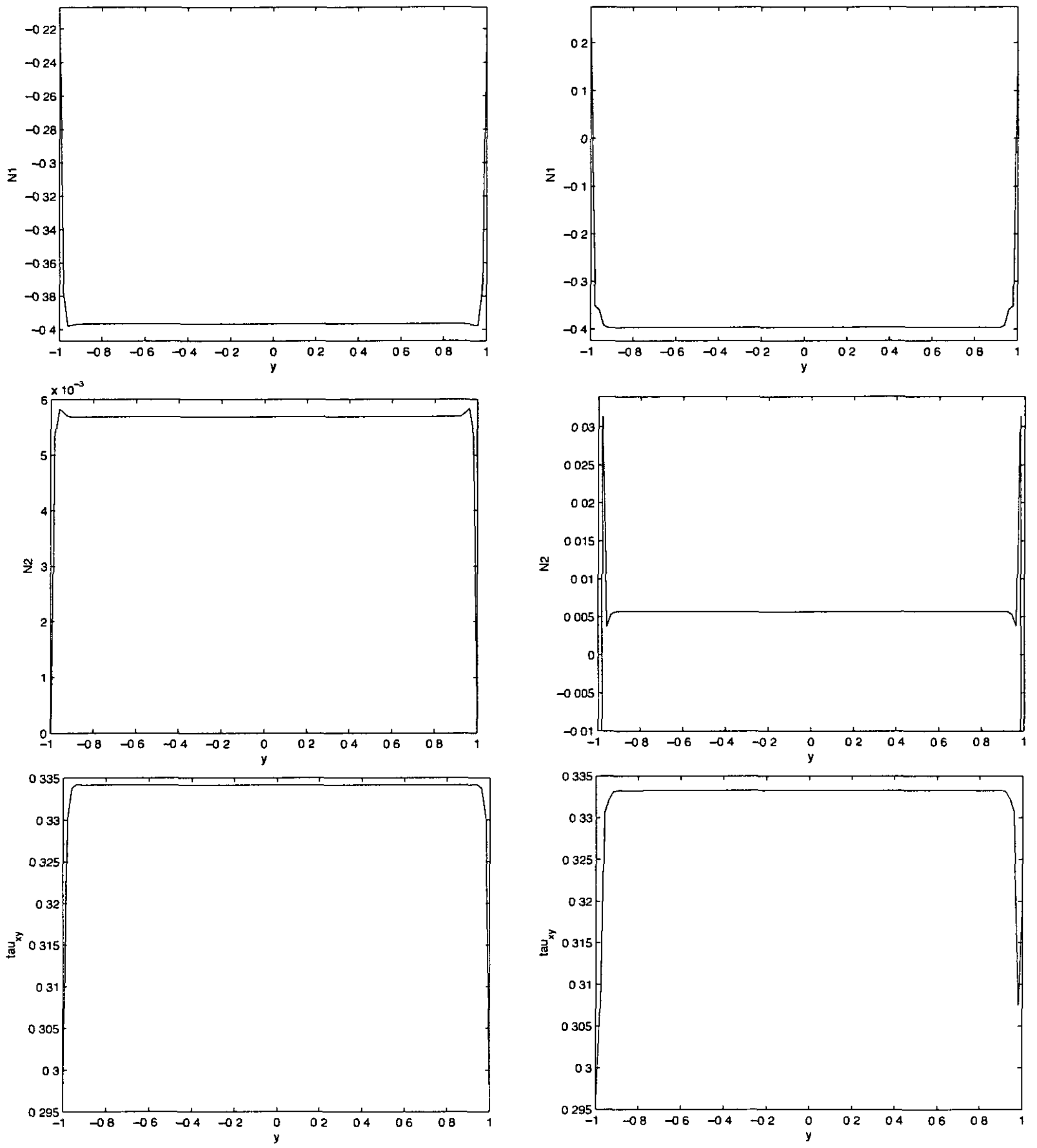

FIG. 62: Normal stress differences, N_1, N_2, and shear stress (τ_{xy}) for $Er = 1000, De = 12$. Left: parallel anchoring. Right: normal anchoring.

increased in order to capture the Leslie angle as the attractors transition from **ES** for low values ($Er = 1$), to **VS** at higher values ($Er = 500$) where sharp boundary layers emerge. From mesoscopic model analysis [15], the scaling behavior of the boundary layer thickness is predicted to be $Er^{-1/2}$ in the asymptotic limit of low De and Er. For $De = 12$, the behavior for simulations with the DQ closure is shown in Fig. 61. To produce this figure, the derivative of the alignment angle in the gap is calculated using a 2-point second-order finite difference scheme (see Table XVI). In the boundary layer, the numerical derivative is large, while in the interior region the derivative is small. The thickness of the boundary layer is estimated from the position in the plate gap where there is a sign change in the derivative values, indicating a transition from the boundary layer where the derivative is negative to the interior bulk region where the derivative is non-negative for $y < 0$ (see Fig. 60). The best exponential fit from the discrete data points in Fig. 61 is $Er^{-0.39}$, which is consistent with the findings of Forest, Wang, and Zhou [16] who determined the boundary layer width scaling to be approximately $Er^{-0.4}$ in their numerical results.

Fig. 62 shows the normal stress differences, $N_1 = \tau_{xx} - \tau_{yy}$ and $N_2 = \tau_{yy} - \tau_{zz}$, along with the shear stress (τ_{xy}) for both anchoring conditions. Except at the boundaries, the value of the first normal stress difference (N_1) is negative, while the value of the second (N_2) is positive. The sharp boundary layers appear in all stress data in Fig. 62. Further, it is important to note that the stress values are independent of the anchoring conditions, as indicated by the fact that at the interior points their values are almost equivalent. The stress results are very important because this data can be directly measured in a laboratory and their results have specific physical interpretations. For example, the sign of N_1 determines whether the liquid is drawing the plates toward one another or pushing them apart. Sign changes within the sample require an average over the plate gap to determine effective normal stress differences [16]. These results are consistent with the findings of Forest, Wang, and Zhou [16], and thus qualitatively agree with the monodomain kinetic simulations [1].

V.2.5 Composite tumbling-wagging periodic states (TW structure attractors)

The **ES** and **VS** steady state attractors give way to spatiotemporal attractors when neither elasticity nor viscosity dominates [16]. The composite tumbling-wagging periodic state occurs when the major director oscillates from -90^o to 90^o in the

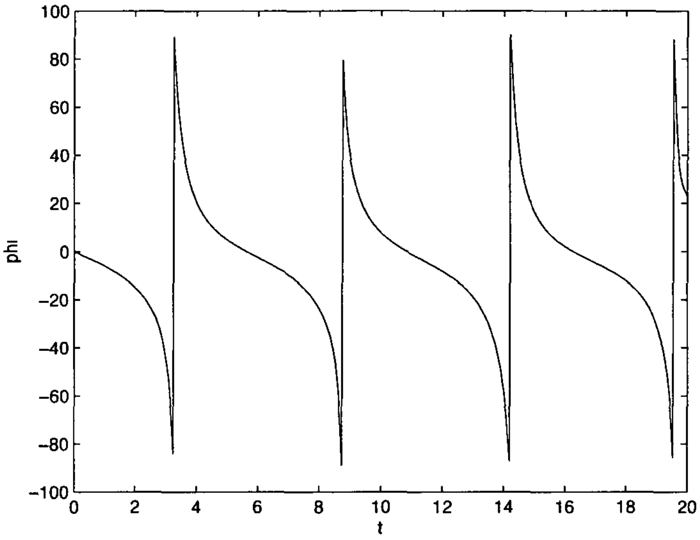

FIG. 63: Evolution of the peak orientation angle (ϕ) for the **TW** attractor midway between the plate gap ($y = 0$) for $Er = 500$ and $De = 3$ with parallel anchoring. 90^o and -90^o imply the same director orientation.

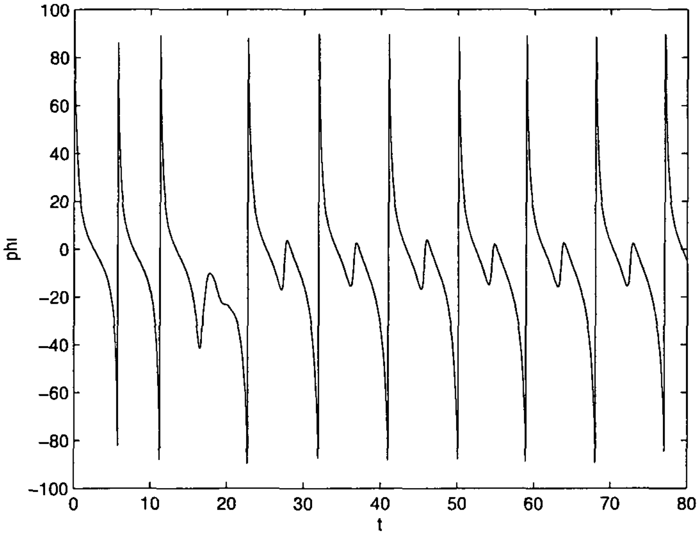

FIG. 64: Evolution of the peak orientation angle (ϕ) for the **TW** attractor midway between the plate gap ($y = 0$) for $Er = 500$ and $De = 3$ with normal anchoring. 90^o and -90^o imply the same director orientation.

middle of the plate gap, similar to the tumbling attractor in the simple shear case. As a results of boundary effects, the oscillation of the major director is less than 90^o near the plates, similar to the wagging attractor in the simple shear case [16, 30]. Note, one only needs to observe the behavior at the mid-gap in order to identify the **TW** attractors. **TW** periodic regime exists at low to moderate De values with sufficiently large Er values [16,30]. The **TW** structures arises before the intermediate **W** state as the De value is increased for fixed Er to attain the **VS** steady state. The **TW** also arises after a transition from the **ES** or intermediate **W** states as the Er value is increased for fixed De. In this case, as $Er \longrightarrow \infty$, the **TW** mode becomes identical to the **T** mode from the simple shear case due to the absence of long-range elasticity and boundary effects. These patterns can be observed in Table XV and Fig. 49.

Fig. 63 is an illustration of the **TW** structure attractor at the middle of the plate gap ($y = 0$) for $Er = 500$, $De = 3$, with parallel anchoring conditions. Here the solution oscillates between -90^o and 90^o with a constant wavelength. However, for the **TW** attractor with normal anchoring conditions seen in Fig. 64, the solution converges to a periodic solution after an initial transition. This is assumed to be a result of the numerical solver and the closure rule, and it is not characteristic of the kinetic solution. For lower Er or lower De values, this behavior is not observed. From Table XV, if the Deborah number is increased from $De = 3$, to say $De = 6$, the structure attractors will transition from **TW** to **W**.

V.2.6 Wagging periodic states (W structure attractors)

The wagging periodic state occurs when the maximum amplitude of oscillation of the major director is less than 90^o, similar to the simple shear flow case, for any point between the plates. It exists for moderate De values with sufficiently large Er values [16,30]. The **W** structures arise as an intermediate state between the **ES** and **TW** states as the Er value is increased for fixed De, or between the **TW** and **VS** states as the De value is increased for fixed Er. This pattern can be observed in Table XV. Note that the transitions between **TW** and **W** occur at slightly lower Deborah and Ericksen numbers for the simulations with the DQ closure than for the kinetic simulations. Additionally, the wagging regime is in a smaller range of Deborah numbers ($5 \leq De \leq 6$) for the closure rule than for the kinetic simulations, where **W** arises for $6 \leq De \leq 8$ for $Er \geq 15$ [16].

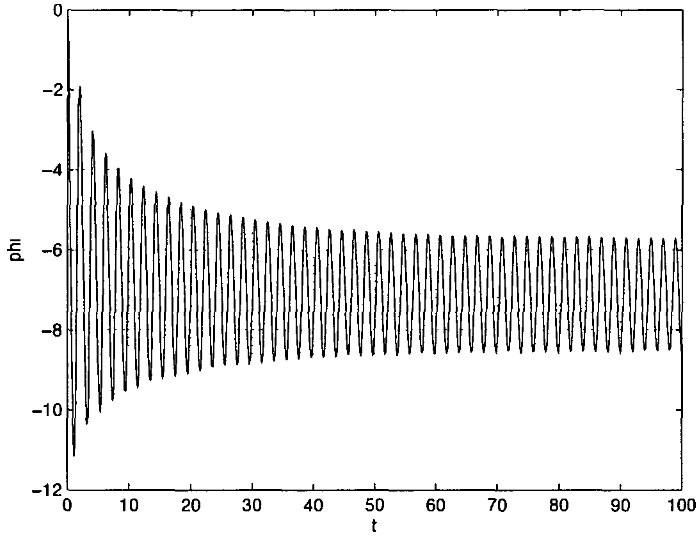

FIG. 65: Evolution of the peak orientation angle (ϕ) for the **W** attractor midway between the plate gap ($y = 0$) for $Er = 500$ and $De = 6$ with parallel anchoring.

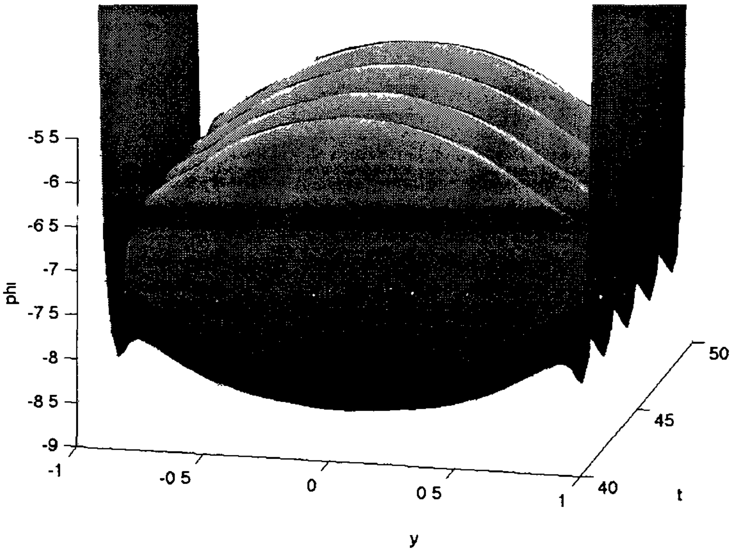

FIG. 66: Spatiotemporal structure of the alignment angle for $Er = 500$ and $De = 6$, with parallel anchoring conditions at the plates ($\psi_o = 0^o$).

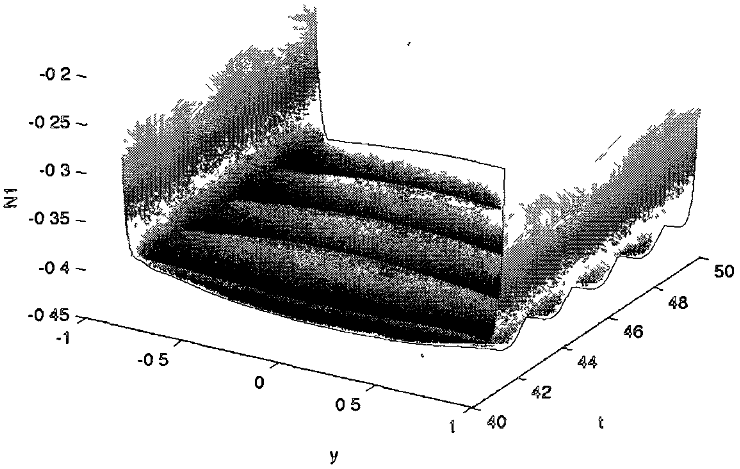

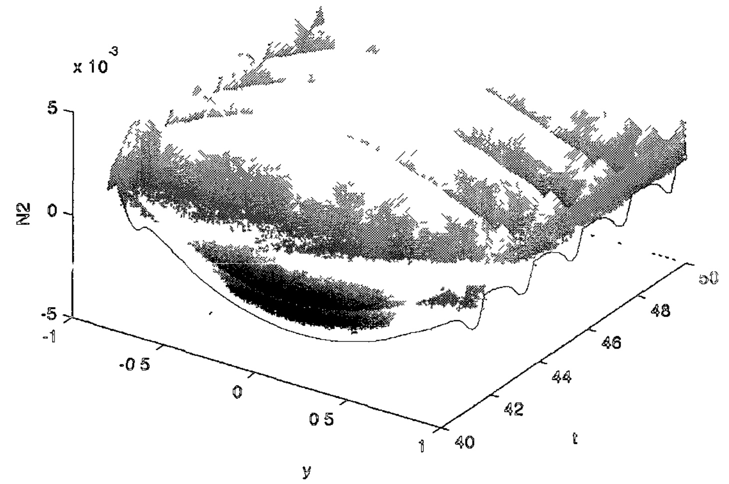

FIG. 67: Spatiotemporal structure of the normal stress differences for $Er = 500$ and $De = 6$, with parallel anchoring conditions at the plates ($\psi_o = 0^o$). Top: First normal stress difference N_1. Bottom: Second normal stress difference N_2.

In Fig. 63 and Fig. 64, the **TW** was observed for $Er = 500$, $De = 3$ with parallel and normal anchoring respectively. Upon increasing the Deborah number to $De = 6$, the structure attractors transition from **TW** to **W**. Fig. 65 is an illustration of the **W** structure attractor at the middle of the plate gap ($y = 0$) for $Er = 500$, $De = 6$, with parallel anchoring conditions ($\phi_o = 0^o$). Initially the solution oscillates between -2^o and -11^o before it dampens to a steady periodic state, where (ϕ) oscillates between -8.5^o and -5.75^o. Again, this transient dampening seems to be the result of the numerical solver and the closure rule, and not characteristic of the kinetic solutions. Fig. 66 is an illustration of the **W** attractor's spatiotemporal structure across the entire plate gap during a time interval where the solution is in its steady periodic state. Here one can see the evolution of the alignment angle: near the plates, the maximum angle of oscillation is approximately -7.5^o, while at the mid-plate gap it is -5.75^o. Additionally, Fig. 67 displays the spatiotemporal structure's of the first (N_1) and second (N_2) normal stress differences under the same conditions. For N_1, sharp boundary layers are present and the value of N_1 is negative as the solution oscillates about $N_1 = -0.425$. For N_2, boundary layers are present and the solution undergoes a sign change as it oscillates about the N_2 axis. Recall that sign changes within the sample require an average over the plate gap to determine effective normal stress differences [16]. In their work, Forest, Wang, and Zhou found that both normal stress differences oscillated about their respective stress axes in the **W** regime [16].

Fig. 68 is an illustration of the **W** structure attractor at the middle of the plate gap for normal anchoring conditions ($\phi_o = 90^o$) with the same parameter values. The solution has a very short dampening zone before it reaches the steady periodic state, where (ϕ) oscillates between -9^o and -5^o. For lower Er values, this behavior is not observed. Note, how the oscillation is not centered about $\phi = 0$. This is not unexpected and overall the results agree with the prior research on the subject [16,30]. Finally, as the Deborah number is increased from $De = 6$, to say $De = 8$, the structure attractors will transition from **W** to **VS** as described in Table XV and Fig. 49.

V.2.7 Velocity Profiles

Previous studies have yielded an exactly solvable asymptotic formula for the velocity of steady-flow nematic structures in plane Couette cells [15]. In it, numerical solutions using the DOI closure are compared with a derived exact asymptotic formula in the

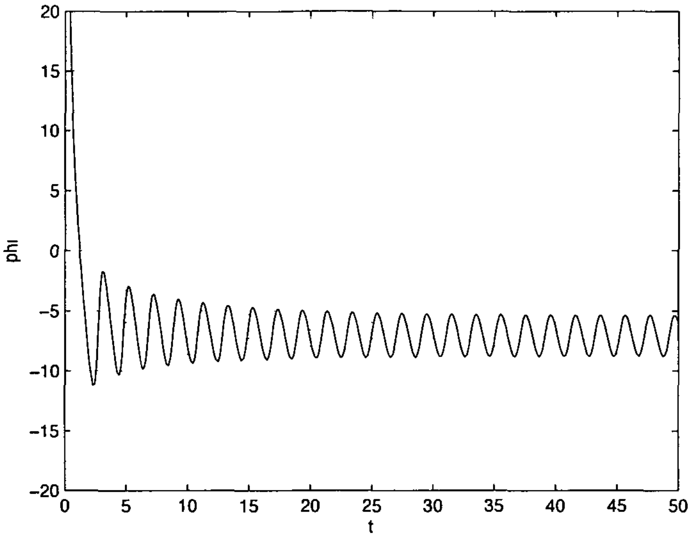

FIG. 68: Evolution of the peak orientation angle (ϕ) for the **W** attractor midway between the plate gap ($y = 0$) for $Er = 500$ and $De = 6$ with normal anchoring.

ES attractor regime. An interesting result of the study is the emergence of non-linear velocity for the numerical solutions. The research showed that while the velocity was linear for the exact asymptotic solution under both anchoring conditions, the velocity exhibited qualitatively distinct velocity structures for the numerical solutions with normal and parallel anchoring conditions. The velocity profiles for the numerical solutions with normal anchoring displayed a greater degree of non-linearity and were of opposite concavity than those with parallel anchoring [15].

The velocity structure for the solution with the DQ closure under parallel anchoring ($\psi_o = 0^o$) conditions for **ES** attractors is examined first. From the top row of Fig. 69, one can see that the velocity is nearly linear for $Er = 1$ and $De = 0.05$. As the Ericksen number is increased from $Er = 1$ to $Er = 30$, the magnitude of the Leslie alignment at the mid-gap of the plate increases and the velocity becomes increasingly non-linear. The bottom row Fig. 69 shows that the velocity profile for the solution with the DQ closure under normal anchoring ($\psi_o = 90^o$) conditions for the same parameter values. In contrast to the parallel anchoring case, as the Ericksen number is increased, the magnitude of the Leslie alignment angle decreases while the degree of non-linearity for the velocity increases. From Fig. 69, one can see the concavity of the non-linear velocity under normal anchoring is opposite that of parallel

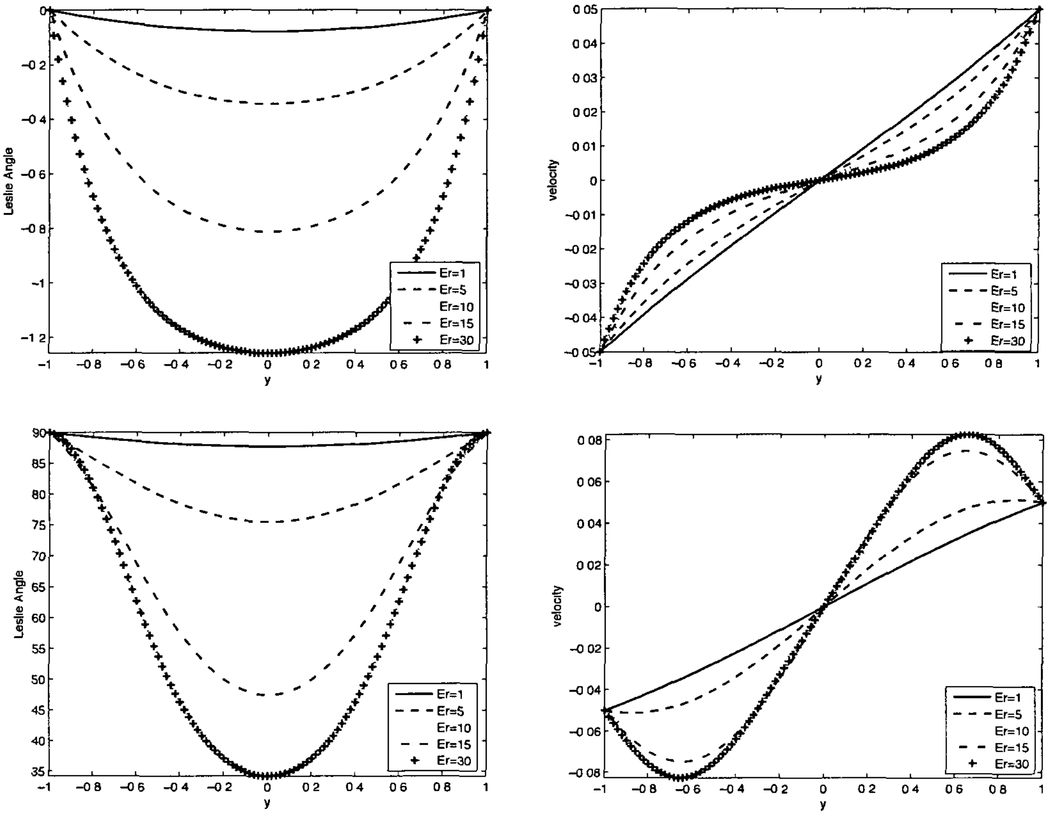

FIG. 69: Numerical solutions for the Leslie alignment angle and velocity structure for $De = 0.05$ and varying Er across the plate gap in the **ES** steady state. Top: parallel anchoring. Bottom: normal anchoring.

anchoring. These results are in agreement with the known numerical results using the DOI closure discussed earlier [15]. From a comparison of the different anchoring conditions in Fig. 69, it is clear that normal and parallel anchoring conditions have different velocity profiles.

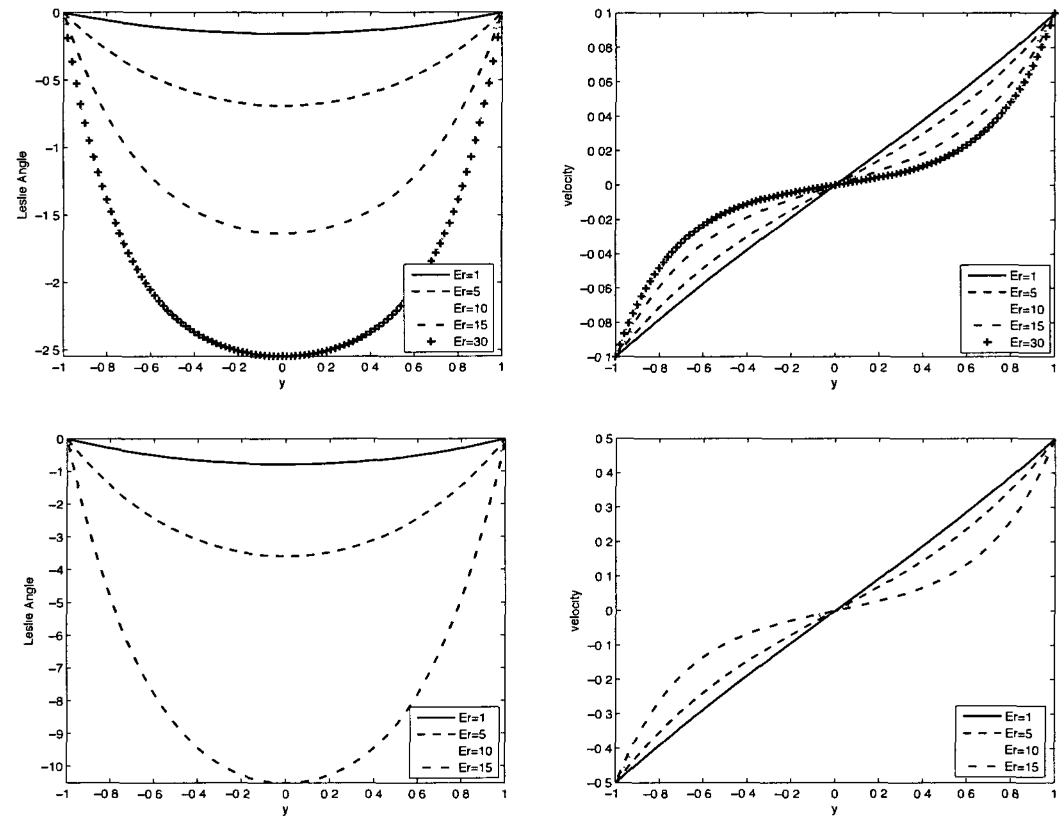

FIG. 70: Numerical solutions for the Leslie alignment angle and velocity structure for increasing De and varying Er across the plate gap in the **ES** steady state with parallel anchoring. Top: $Er = 0.1$. Bottom: $Er = 0.5$.

As an extension of previous research [15, 16, 30], the effects of Ericksen number (Er) and Deborah number (De) on the phenomena of non-linear velocity structures under parallel ($\psi_o = 0^o$) and normal ($\psi_o = 90^o$) anchoring conditions are examined. Fig. 69, Fig. 70, Fig. 71, and Fig. 72 depict the velocity profiles over the range of Ericksen numbers from the **ES** attractor regime in Table XV for small Deborah numbers ($De \leq 0.5$). For the case of parallel anchoring, from Fig. 69, Fig. 70, and Fig. 72, it appears that increasing the Ericksen number has a much greater effect

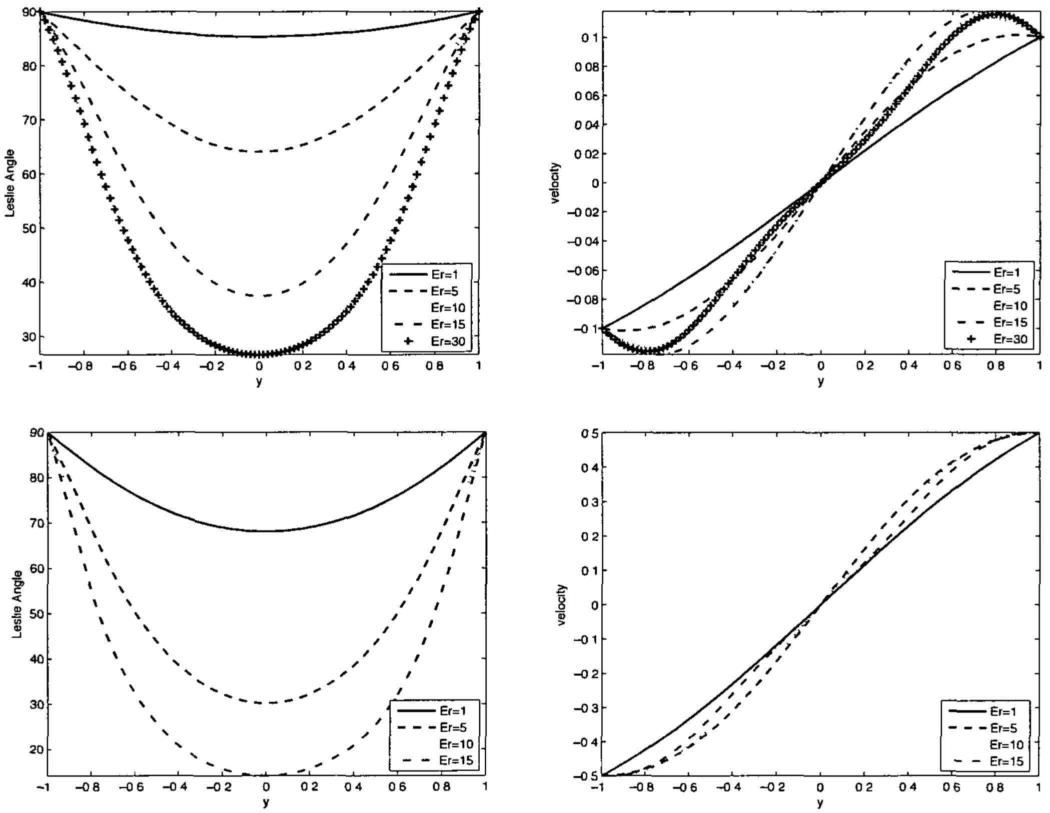

FIG. 71: Numerical solutions for the Leslie alignment angle and velocity structure for increasing *De* and varying *Er* across the plate gap in the **ES** steady state with normal anchoring. Top: $Er = 0.1$. Bottom: $Er = 0.5$.

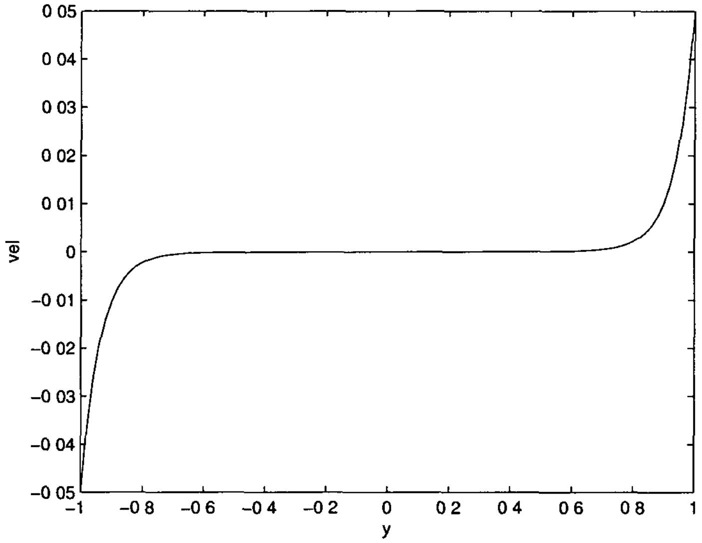

FIG 72 Numerical solution for the velocity structure for $Er = 500, De = 0\ 05$ with parallel anchoring ($\psi_o = 0^o$) across the plate gap See Fig 54 for evolution of the peak orientation angle and Leslie alignment angle in the **ES** steady state for the same parameters

on the velocity profile than by increasing the Deborah number In general, for a fixed De value, increasing the Er value increases the degree of non-linearity for the velocity structure For all given De values, the velocity is nearly linear for $Er = 1$ under parallel anchoring conditions In Fig 72, the effect of weak flow is further examined for $Er = 500$ and $De = 0\ 05$ Here the velocity is highly non-linear at the plate boundaries The same behavior at high Ericksen numbers has been observed for the DQ closure under normal anchoring conditions Fig 69 and Fig 71 depict the velocity profiles for $De = 0\ 05, 0\ 1, 0\ 5$ with $\psi_o = 90^o$ Similar to the parallel anchoring case, increasing the Ericksen number has a greater effect on the velocity profile than increasing the Deborah number However, for $De = 0\ 5$, the velocity is slightly non-linear for $Er = 1$ under normal anchoring conditions indicating that Deborah number does effect the velocity profile

Extending this idea further, Fig 73 explores the effects of the Deborah number on the velocity profile in the **ES** attractor regime (see Table XV and Fig 49) for

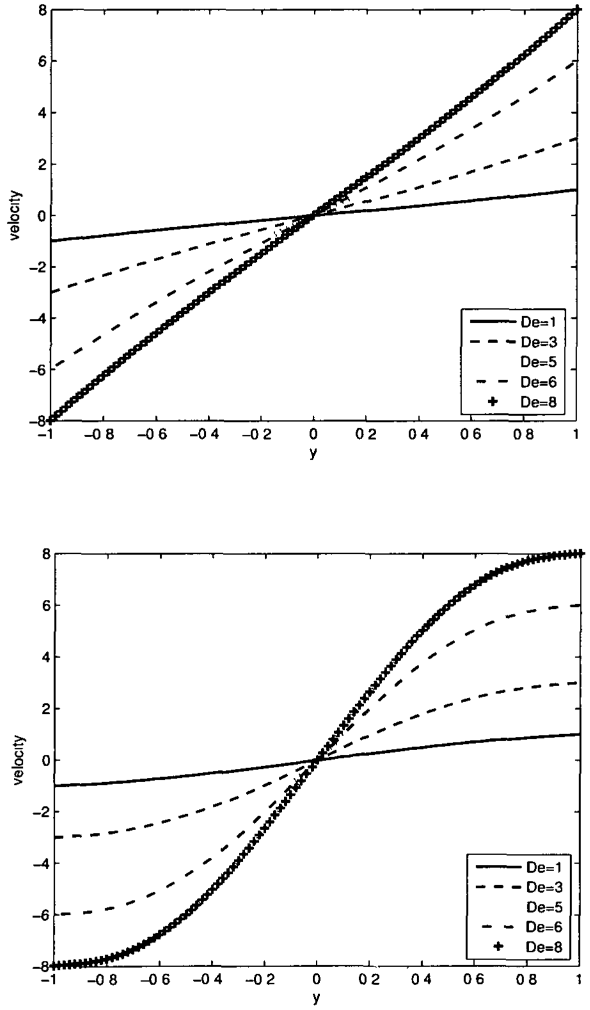

FIG. 73: Numerical solutions of the velocity structure for $Er = 1$ and increasing De across the plate gap in the **ES** steady state. See Fig. 51 and Fig. 52 for the Leslie alignment angle in the **ES** steady state for the same parameters. Top: parallel anchoring. Bottom: normal anchoring.

a small Ericksen number ($Er = 1$). The top graph in Fig. 73 displays the velocity structure for $Er = 1$ with the Deborah number increasing from $De = 1$ to $De = 8$ for parallel anchoring conditions. Note how the velocity is nearly linear for the given values of De. Alternatively, the bottom of Fig. 73 displays the velocity structure for normal anchoring with the same parameter values. Here the degree of non-linearity for the velocity structure increases as the Deborah number gets larger.

In summary, normal and parallel anchoring conditions have qualitatively distinct velocity profiles; the non-linear velocity profiles for the two anchoring conditions are of opposite concavity. For the **ES** attractor regime, increasing the Ericksen number has a significant effect on the linearity of the velocity profile for both parallel and normal anchoring conditions. Additionally, under normal anchoring conditions, the degree of non-linearity of the velocity structure increases as the Deborah number gets larger for small Er values in the **ES** regime. The same phenomena is not observed with parallel anchoring conditions.

CHAPTER VI

CONCLUSIONS

There is a current interest in simulating liquid crystalline polymers in order to better understand their applications in material processing. Unfortunately, the kinetic model is computationally intensive and its solution depends on information from higher order moments. As a result, the kinetic equations utilize closure approximations to derive a system of differential equations which can be solved numerically at a relatively lower computational cost. However, most current closure schemes have many shortcomings. In response, a new closure scheme, the DQ closure, was designed by doing a least squares fit on data from simulations with four current closure schemes, DOI, TR, HL1, and HL2, under simple shear flow conditions. The resulting DQ closure was compared with these and the Bingham closure schemes under a variety of flow conditions in order to determine its validity.

Under equilibrium conditions, the bifurcation diagram from the proposed DQ closure scheme more closely resembled the kinetic solution's than either the DOI or TR; and the proposed closure performed as well, if not better, than the HL1 closure at equilibrium. Additionally, the DQ closure gave an acceptable quantitative approximation to the kinetic solution without the use of artificial shift parameters, unlike in the case of the HL1 and HL2 closures.

For shear flow conditions, the performance of the DQ closure is superior to its component closure schemes and comparable to the Bingham closure, which is currently considered to be one of the best closure schemes. For $Pe < 0.189$, the proposed closure fails to predict any periodic flow. This can be a result of the numerical solver or the closure scheme, since this problem exists only within a small range of flow rates. The DOI closure fails to predict periodic flow for all (N, Pe) space. For flow conditions with a minimal flow rate ($Pe \geq 0.189$), the DQ closure scheme simulates all attractor types except **CH**. For stronger flow with higher polymer concentration ($N > 5.75$), the DQ closure fails to predict a return to the **FA** regime, which is a known result from the kinetic simulations. It does succeed in predicting the other attractors in this region that the kinetic solution identifies, and its shortcomings are not unique. The Bingham closure also fails to predict the existence of the **FA** regime at sufficiently high Pe and N values. The HL1 and HL2 closures are pathological at high Pe and N values. Also noteworthy is the ability of the DQ closure to identify the T-W transition, which is not detected by AUTO and can only be found through post-processing the data. This transition occurs in the kinetic solution and its bifurcation properties are not widely agreed upon, and so it is of particular interest that a closure rule detected it in approximately the same (N, Pe) space as the kinetic solution.

Lastly, the performance of the DQ closure was examined under conditions of plane Couette flow in cells with both parallel and normal anchoring conditions at the plates. In accordance with the kinetic solution and independent of anchoring type, the proposed DQ closure identified **ES** attractors for sufficiently low Er values; **VS** attractors for sufficiently high De and Er values; **TW** attractors for moderate De values with sufficiently high Er values; and the **W** transient state which occurs between the **ES** and **TW** regimes and the **TW** and **VS** regimes. The normal stress differences and shear stress calculated from the simulations with the DQ closure had the same behavior at the plate boundaries and were of the same sign as the kinetic solutions. Additionally, the velocity profiles from the solutions with the closure scheme displayed the same non-linear phenomena as solutions generated with existing closure schemes. Normal and parallel anchoring conditions gave qualitatively distinct velocity profiles and their corresponding velocity curves were of opposite concavity. Velocity results from simulations with the proposed closure suggested that increasing the Ericksen number has a greater effect on the velocity profile than increasing the Deborah number for the **ES** attractor regime.

In summary, the DQ closure scheme gives a better qualitative approximation to the kinetic solution than its component rules, DOI, TR, HL1, and HL2. Without the use of artificial shift parameters, it gives an acceptable approximation to the kinetic solution at equilibrium. For shear flow conditions, it gives a more complete flow phase diagram than it component rules. It has limitations, but they are not unique or catastrophic. For flow in plane Couette cells, the DQ closure give a complete description of the attractor regimes in accordance with the known kinetic solutions and displays the phenomena of non-linear velocity common to other numerical solutions.

Considering the success of the DQ closure under the equilibrium, plane shear flow, and plane Couette flow testing conditions, future work can be conducted in an attempt to improve the performance of the proposed scheme and better understand the phenomena associated with it. Research can be conducted on the T-W transition in the shear flow case for the both the kinetic solution and the closure rule solutions in order to better understand if a bifurcation occurs during the transition, and if so, what type of bifurcation. Along similar lines, one can further inspect the non-linear velocity profile of solutions with closure rules verse the linear velocity profile of the kinetic solution in plane Couette cells. Additionally, research can be conducted to design a new least squares closure rule by fitting the data over a smaller area of (N, Pe) space to see if the accuracy of the quantitative and qualitative results can be increased. In doing such a least squares fit, the closure rules being used to simulate the data can also changed based on the space one is trying to predict the behavior for. For example, since HL1 and HL2 perform poorly at high N and Pe values, one may choose to not use them in the least squares fit for that range.

BIBLIOGRAPHY

[1] M. G. Forest, Q. Wang, R. Zhou, The flow-phase diagram of Doi-Hess theory for sheared nematic polymers ii: finite shear rates, Rheol. Acta 44 (2004) 80–93.

[2] M. Doi, S. F. Edwards, The Theory of Polymer Dynamics, no. 73 in International Series of Monographs on Physics, Oxford University Press, 1986.

[3] T. Tsuji, A. D. Rey, Effect of long range order on sheared liquid crystalline materials part 1: compatibility between tumbling behavior and fixed anchoring, J. Non-Newtonian Fluid Mech. 73 (1997) 127–152.

[4] C. V. Chaubal, L. G. Leal, A closure approximation for liquid-crystalline polymer models based on parametric density estimation, J. Rheol. 42 (1) (1998) 177–201.

[5] M. Kroger, A. Ammar, F. Chinesta, Consistent closure schemes for statistical models of anisotropic fluids, J. Non-Newtonian Fluid Mech. 149 (2008) 40–55.

[6] J. Feng, C. V. Chaubal, L. G. Leal, Closure approximations for the Doi theory: Which to use in simulating complex flows of liquid-crystaline polymers?, J. Rheol. 42 (5) (1998) 1095–1119.

[7] M. Grosso, P. L. Maffettone, F. Dupret, A closure approximation for nematic liquid crystals based on the canonical distribution subspace theory, Rheol Acta 39 (2000) 301–310.

[8] M. G. Forest, Q. Wang, R. Zhou, The weak shear kinetic phase diagram for nematic polymers, Rheol. Acta 43 (2004) 17–37.

[9] P. L. Maffettone, V. Faraoni, M. Grosso, S. Crescitelli, The rigid-rod model for nematic polymers: An analysis of the shear flow problem, J. Rheol. 43 (3) (1999) 829–843.

[10] Q. Wang, Comparative studies on closure approximations in flows of liquid crystal polymers: I. elongational flows, J. Non-Newtonian Fluid Mech. 72 (1997) 141–162.

[11] Q. Wang, Comparative studies on closure approximations in flows of liquid crystal polymers: II. fiber flows, J. Non-Newtonian Fluid Mech. 72 (1997) 163–185.

[12] M. G. Forest, Q. Wang, R. Zhou, E. P. Choate, Monodomain response of arbitrary aspect ratio nematic polymers in general linear planar flows, J. Non-Newtonian Fluid Mech. 118 (2004) 17–31.

[13] M. G. Forest, Q. Wang, Monodomain response of finite-aspect-ratio macromolecules in shear and related linear flows, Rheol. Acta 42 (2003) 20–46.

[14] M. G. Forest, R. Zhou, Q. Wang, Scaling behavior of kinetic orientational distributions for dilute nematic polymers in weak shear, J. Non-Newtonian Fluid Mech. 116 (2004) 183–204.

[15] M. G. Forest, Q. Wang, H. Zhou, R. Zhou, Structure scaling properties of confined nematic polymers in plane Couette cells: The weak flow limit, J. Rheol. 48 (1) (2004) 175–192.

[16] M. G. Forest, R. Zhou, Q. Wang, Kinetic structure simulations of nematic polymers in plane Couette cells ii: in-plane structure transitions, Multiscale Model Simul. 4 (4) (2005) 1280–1304.

[17] M. Grosso, P. L. Maffettone, P. Halin, R. Keunings, V. Legat, Flow of nematic polymers in eccentric cylinder geometry: influence of closure approximation, J. Non-Newtonian Fluid Mech. 94 (2000) 119–134.

[18] H. C. Ottinger, On the stupendous beauty of closure, J. Rheol. 53 (6) (2009) 1285–1304.

[19] M. Doi, Molecular dynamics and rheological properties of concentrated solutions of rodlike polymers in isotropic and liquid crystalline phases, J. Polym Sci. Polym. Phys. Ed. (19) (1981) 229–243.

[20] S. Hess, Fokker-Planck-equation approach to flow alignment in liquid crystals, Z. Naturforsch 31A (1976) 1034–1037.

[21] A. V. Bhave, R. K. Menon, R. C. Armstrong, R. A. Brown, A constitutive equation for liquid-crystalline polymer solutions, J. Rheol. 37 (3) (1993) 413–441.

[22] E. J. Hinch, L. G. Leal, Constitutive equations in suspension mechanics. Part 2: Approximate forms for a suspension of rigid particles affected by Brownian rotations, J. Fluid Mech. 76 (1) (1976) 187–208.

[23] M. G. Forest, R. Zhou, Q. Wang, Symmetries of the Doi kinetic theory for nematic polymers of arbitrary aspect ratio: at rest and in linear flows, Phys. Rev. E 66 (3) (2002) 031712.

[24] L. Onsager, The effects of shape on the interaction of colloidal particles, Ann. N.Y. Acad. Sci. 51 (1949) 627–659.

[25] R. G. Larson, H. Ottinger, The effect of molecular elasticity on out-of-plane orientations in shearing flows of liquid crystalline polymers, Macromolecules 24 (1991) 6270–6282.

[26] R. L. Burden, J. D. Faires, Numerical Analysis, 7th Edition, Brooks/Cole, Pacific Grove, CA, 2001.

[27] C. D. Meyer, Matrix Analysis and Applied Linear Algebra, SIAM, Philadelphia, PA, 2000.

[28] E. J. Doedel, A. R. Champneys, T. F. Fairgrieve, Y. A. Kuznetsov, B. Sandstede, X. Wang, AUTO97: continuation and bifurcation software for ordinary differentail equations, Concordia University (March 1998).

[29] A. Jutan, implot.m, http://www.mathworks.com/matlabcentral/fileexchange/300-implot-m (February 1999).

[30] T. Tsuji, A. D. Rey, Effect of long range order on sheared liquid crystalline materials: Flow regimes, transitions, and rheological phase diagrams, Phys. Rev. E 62 (6) (2000) 8141–8151.

[31] Q. Wang, A hydrodynamic theory for solutions of nonhomogeneous nematic liquid crystalline polymers of different configurations, J. Chem. Phys. 116 (2002) 9120–9136.

APPENDIX A

TENSOR NOTATION

The following defines the tensor notation used in the text.

For two second order tensors **A** and **B**, $\mathbf{A} \cdot \mathbf{B}$ is matrix multiplication:

$$\mathbf{A} \cdot \mathbf{B} = \sum_{j=1}^{3} A_{ij} B_{jk}. \tag{66}$$

For two second order tensors **A** and **B**, the tensor contraction is defined as:

$$\mathbf{A} : \mathbf{B} = \sum_{i=1}^{3} \sum_{j=1}^{3} A_{ij} B_{ij}. \tag{67}$$

For a second order tensors **A** and a fourth order symmetric tensor **C**, the tensor contraction is defined as:

$$\mathbf{A} : \mathbf{C} = \sum_{i=1}^{3} \sum_{j=1}^{3} A_{ij} C_{ijkl}. \tag{68}$$

APPENDIX B

TRACE OF THE CLOSURE RULES

A valid closure rule for $\mathbf{Q} : \langle \mathbf{mmmm} \rangle$ must meet the condition

$$tr(\mathbf{Q} : \langle \mathbf{mmmm} \rangle) = \mathbf{Q} : \mathbf{M}, \tag{69}$$

where Q is symmetric and traceless and $\mathbf{Q} = \mathbf{M} - \frac{1}{3}\mathbf{I}$.

$$tr(\mathbf{Q}) = 0 \qquad tr(\mathbf{M}) = 1. \tag{70}$$

The following shows how the DOI, HL1, and HL2 closure rules fulfill the condition, while the TR closure rule does not for $\mathbf{Q} : \langle \mathbf{mmmm} \rangle$. The DOI closure rule is as follows:

$$\mathbf{Q} : \langle \mathbf{mmmm} \rangle \approx (\mathbf{Q} : \mathbf{M})\mathbf{M}. \tag{71}$$

Giving

$$tr((\mathbf{Q} : \mathbf{M})\mathbf{M}) = (\mathbf{Q} : \mathbf{M})(tr(\mathbf{M})) = \mathbf{Q} : \mathbf{M}, \tag{72}$$

showing that the condition is met.

The HL1 closure rule is as follows:

$$\mathbf{Q} : \langle \mathbf{mmmm} \rangle \approx \frac{1}{5}\left[6\mathbf{M} \cdot \mathbf{Q} \cdot \mathbf{M} - \mathbf{M}\left(\mathbf{Q} : \mathbf{M}\right) - 2\left((\mathbf{MM}) : \mathbf{Q}\right)\mathbf{I} + 2\mathbf{M} : \mathbf{Q}I\right]. \tag{73}$$

First consider the terms $\mathbf{M} \cdot \mathbf{Q} \cdot \mathbf{M}$ and $(\mathbf{MM}) : \mathbf{Q}$.

Define $\mathbf{MM} = \mathbf{G}$, where $\mathbf{MM} = \mathbf{M} \cdot \mathbf{M} = \mathbf{M}^2$

$$\begin{aligned}
\mathbf{G} : \mathbf{Q} &= \sum_{i,j=1}^{3} \mathbf{G}_{ij}\mathbf{Q}_{ij}. \\
tr(\mathbf{M} \cdot \mathbf{Q} \cdot \mathbf{M}) &= tr(\mathbf{M} \cdot \mathbf{M} \cdot \mathbf{Q}). \\
tr(\mathbf{M} \cdot \mathbf{M} \cdot \mathbf{Q}) &= tr(\mathbf{G} \cdot \mathbf{Q}). \\
tr(\mathbf{G} \cdot \mathbf{Q}) &= \sum_{i,j=1}^{3} \mathbf{G}_{ij}\mathbf{Q}_{ij}. \\
\therefore tr(\mathbf{M} \cdot \mathbf{Q} \cdot \mathbf{M}) &= (\mathbf{MM}) : \mathbf{Q}.
\end{aligned} \tag{74}$$

Using the above and that $tr((\mathbf{Q} : \mathbf{M})\mathbf{M}) = \mathbf{Q} : \mathbf{M}$ from the Doi closure rule, the trace from HL1 can easily be found.

$$
\begin{aligned}
tr(\frac{1}{5}[6\mathbf{M}\cdot\mathbf{Q}\cdot\mathbf{M}-\mathbf{MM}:\mathbf{Q}-2(\mathbf{M}^2:\mathbf{Q})\mathbf{I}+2\mathbf{M}:\mathbf{Q}I])\\
=(\frac{1}{5}[6tr(\mathbf{M}\cdot\mathbf{Q}\cdot\mathbf{M})-\mathbf{M}:\mathbf{Q}tr(\mathbf{M})-2(\mathbf{M}^2:\mathbf{Q})tr(\mathbf{I})+2\mathbf{M}:\mathbf{Q}tr(\mathbf{I})])\\
=(\frac{1}{5}[6tr(\mathbf{M}\cdot\mathbf{Q}\cdot\mathbf{M})-\mathbf{M}:\mathbf{Q}-6(\mathbf{M}^2:Q)\mathbf{I}+6\mathbf{M}:\mathbf{Q}])\\
=\frac{1}{5}[5\mathbf{M}:\mathbf{Q}].
\end{aligned}
$$

$$
\therefore tr(\frac{1}{5}[6\mathbf{M}\cdot\mathbf{Q}\cdot\mathbf{M}-\mathbf{MM}:\mathbf{Q}-2(\mathbf{M}^2:\mathbf{Q})\mathbf{I}+2\mathbf{M}:\mathbf{Q}I])=\mathbf{Q}:\mathbf{M}, \tag{75}
$$

showing that the condition is met.

The HL2 closure rule is as follows:

$$
\begin{aligned}
\mathbf{Q}:\langle\mathbf{mmmm}\rangle &\approx \mathbf{M}(\mathbf{M}:\mathbf{Q})+2\left[\mathbf{M}\cdot\mathbf{Q}\cdot\mathbf{M}-\mathbf{M}^2\left(\mathbf{M}^2:\mathbf{Q}\right)/\left(\mathbf{I}:\mathbf{M}^2\right)\right]\\
&\quad+\alpha\left[\frac{52}{315}\mathbf{Q}-\frac{8}{21}\left(\mathbf{Q}\cdot\mathbf{M}+\mathbf{M}\cdot\mathbf{Q}-\frac{2}{3}(\mathbf{M}:\mathbf{Q})\mathbf{I}\right)\right]. \qquad (76)\\
\alpha &= exp\left[2\left(1-3\mathbf{M}^2:\mathbf{I}\right)/\left(1-\mathbf{M}^2:\mathbf{I}\right)\right].
\end{aligned}
$$

Given the symmetry of M and Q it simplifies to:

$$
\begin{aligned}
\mathbf{Q}:\mathbf{M} &\approx \mathbf{M}(\mathbf{M}:\mathbf{Q})+2\left[\mathbf{M}\cdot\mathbf{Q}\cdot\mathbf{M}-\mathbf{M}^2\left(\mathbf{M}^2:\mathbf{Q}\right)/\left(\mathbf{I}:\mathbf{M}^2\right)\right]\\
&\quad+\alpha\left[\frac{52}{315}\mathbf{Q}-\frac{8}{21}\left(2\mathbf{Q}\cdot\mathbf{M}-\frac{2}{3}(\mathbf{M}:\mathbf{Q})\mathbf{I}\right)\right].
\end{aligned} \tag{77}
$$

First consider the terms $I:\mathbf{M}^2$ and $tr(\mathbf{M}^2)$.

$$
\begin{aligned}
Let\ \mathbf{M}^2 &= \mathbf{G}.\\
I:\mathbf{M}^2 &= I:\mathbf{G}=\sum_{i,j=1}^{3}I_{ij}\mathbf{G}_{ij}=\sum_{i=1}^{3}\mathbf{G}_{ii}.\\
tr(\mathbf{M}^2) &= tr(\mathbf{G})=\sum_{i=1}^{3}\mathbf{G}_{ii}.\\
\therefore(\mathbf{I}:\mathbf{M}^2) &= tr(\mathbf{M}^2).
\end{aligned} \tag{78}
$$

Now consider the terms $\mathbf{M}:\mathbf{Q}$ and $tr(\mathbf{Q}\cdot\mathbf{M})$.

$$
\mathbf{M}:\mathbf{Q} = \sum_{i,j=1}^{3}M_{ij}\mathbf{Q}_{ij}.
$$

$$
tr(\mathbf{Q}\cdot\mathbf{M})=\sum_{i,j=1}^{3}\mathbf{Q}_{ij}\mathbf{M}_{ij}.
$$

$$
\therefore\mathbf{M}:\mathbf{Q}=tr(\mathbf{Q}\cdot\mathbf{M}). \tag{79}
$$

Using the above, the previous results $tr(\mathbf{M}\cdot\mathbf{Q}\cdot\mathbf{M}) = (\mathbf{M}^2 : \mathbf{Q})$ and $tr((\mathbf{Q} : \mathbf{M})\mathbf{M}) = \mathbf{Q} : \mathbf{M}$, the symmetry and trace of $\mathbf{M}$ and $\mathbf{Q}$, it follows that:

$$\begin{aligned}
& tr(\mathbf{M}(\mathbf{M} : \mathbf{Q}) + 2[\mathbf{M}\cdot\mathbf{Q}\cdot\mathbf{M} - \mathbf{M}^2\left(\frac{\mathbf{M}^2 : \mathbf{Q}}{I : \mathbf{M}^2}\right)] \\
& \quad +\alpha[\frac{52}{315}\mathbf{Q} - \frac{8}{21}(2\mathbf{Q} : \mathbf{M} - \frac{2}{3}(\mathbf{M} : \mathbf{Q})\mathbf{I})]) \\
&= (\mathbf{M} : \mathbf{Q})tr(\mathbf{M}) + 2[tr(\mathbf{M}\cdot\mathbf{Q}\cdot\mathbf{M}) - \left(\frac{\mathbf{M}^2 : \mathbf{Q}}{I : \mathbf{M}^2}\right) tr(\mathbf{M}^2)] \\
& \quad +\alpha[\frac{52}{315}tr(\mathbf{Q}) - \frac{8}{21}(2tr(\mathbf{Q}\mathbf{M}) - \frac{2}{3}(\mathbf{M} : \mathbf{Q})tr(\mathbf{I}))] \\
&= (\mathbf{M} : \mathbf{Q}) + 2[tr(\mathbf{M}\cdot\mathbf{Q}\cdot\mathbf{M}) - \left(\frac{\mathbf{M}^2 : \mathbf{Q}}{I : \mathbf{M}^2}\right) tr(\mathbf{M}^2)] \\
& \quad +\alpha[-\frac{8}{21}(2tr(\mathbf{Q}\mathbf{M}) - 2(\mathbf{M} : \mathbf{Q}))] \\
&= (\mathbf{M} : \mathbf{Q}) + 2[tr(\mathbf{M}\cdot\mathbf{Q}\cdot\mathbf{M}) - (\mathbf{M}^2 : \mathbf{Q})]. \qquad (80)
\end{aligned}$$

Giving

$$\begin{aligned}
& tr(\mathbf{M}(\mathbf{M} : \mathbf{Q}) + 2[\mathbf{M}\cdot\mathbf{Q}\cdot\mathbf{M} - \mathbf{M}^2\left(\frac{\mathbf{M}^2 : \mathbf{Q}}{I : \mathbf{M}^2}\right)] \\
& +\alpha[\frac{52}{315}\mathbf{Q} - \frac{8}{21}(\mathbf{Q}\cdot\mathbf{M} + \mathbf{M}\cdot\mathbf{Q} - \frac{2}{3}(\mathbf{M} : \mathbf{Q})\mathbf{I})]) = \mathbf{Q} : \mathbf{M}, \qquad (81)
\end{aligned}$$

showing that the condition is met.

The Tsuji-Rey closure rule is as follows:

$$\begin{aligned}
\mathbf{Q} : \langle\mathbf{mmmm}\rangle \;\approx\; & \frac{1}{4}\Big[(\mathbf{Q} : \mathbf{M})\mathbf{M} + \mathbf{Q}\cdot\mathbf{M}\cdot\mathbf{M} + \mathbf{M}\cdot\mathbf{Q}\cdot\mathbf{M} \\
& +\mathbf{M}^2\cdot\mathbf{Q} - (\mathbf{M}^2 : \mathbf{Q})\,\mathbf{I}\Big] + \frac{1}{3}\mathbf{Q} : \mathbf{M}I \qquad (82)
\end{aligned}$$

Which given the symmetry of $\mathbf{M}$ and $\mathbf{Q}$ simplifies to

$$\mathbf{Q} : \langle\mathbf{mmmm}\rangle \approx \frac{1}{4}[(\mathbf{Q} : \mathbf{M})\mathbf{M} + 3\mathbf{M}\cdot\mathbf{Q}\cdot\mathbf{M} - (\mathbf{M}^2 : \mathbf{Q})\mathbf{I}] + \frac{1}{3}(\mathbf{Q} : \mathbf{M})\mathbf{I}. \qquad (83)$$

Finally, using the results $tr(\mathbf{M}\cdot\mathbf{Q}\cdot\mathbf{M}) = (\mathbf{M}^2 : \mathbf{Q})$ and $tr((\mathbf{Q} : \mathbf{M})\mathbf{M}) = \mathbf{Q} : \mathbf{M}$ from above, the trace is as follows:

$$\begin{aligned}
& tr(\frac{1}{4}[(\mathbf{Q} : \mathbf{M})\mathbf{M} + 3\mathbf{M}\cdot\mathbf{Q}\cdot\mathbf{M} - (\mathbf{M}^2 : \mathbf{Q})\mathbf{I}] + \frac{1}{3}(\mathbf{Q} : \mathbf{M})\mathbf{I}) \\
&= \frac{1}{4}[tr((\mathbf{Q} : \mathbf{M})\mathbf{M}) + 3tr(\mathbf{M}\cdot\mathbf{Q}\cdot\mathbf{M}) - (\mathbf{M}^2 : \mathbf{Q})tr(\mathbf{I})] + \frac{1}{3}(\mathbf{Q} : \mathbf{M})tr(\mathbf{I}) \\
&= \frac{1}{4}[(\mathbf{Q} : \mathbf{M}) + 3tr(\mathbf{M}\cdot\mathbf{Q}\cdot\mathbf{M}) - 3(\mathbf{M}^2 : \mathbf{Q})] + (\mathbf{Q} : \mathbf{M}) \\
&= \frac{1}{4}(\mathbf{Q} : \mathbf{M}) + (\mathbf{Q} : \mathbf{M}). \qquad (84)
\end{aligned}$$

Giving

$$tr(\frac{1}{4}[(\mathbf{Q}\colon \mathbf{M})\mathbf{M} + \mathbf{Q}\cdot\mathbf{M}\cdot\mathbf{M}\mathbf{M}\cdot\mathbf{Q}\cdot\mathbf{M} + \mathbf{M}^2\cdot\mathbf{Q} - (\mathbf{M}^2\colon \mathbf{Q})\mathbf{I}]) = \frac{5}{4}\mathbf{Q} : \mathbf{M}, \quad (85)$$

which does not meet the condition $tr(\mathbf{Q} : \langle\mathbf{mmmm}\rangle) = \mathbf{Q} : \mathbf{M}$ It must be noted that Tsuji and Rey constructed the closure rule for the contraction $\mathbf{Q} : \langle\mathbf{QQQQ}\rangle$ [3]. However, in the construction of the DQ closure rule, the higher order tensor needed to be $\langle\mathbf{mmmm}\rangle$. As a result, the fact that the trace of TR closure when applied to $\mathbf{Q} : \langle\mathbf{mmmm}\rangle$ was $1.25\mathbf{Q} : \mathbf{M}$ needs to be factored into the proposed DQ closure, but it does not prevent the TR closure from being utilized in the least squares fit.

APPENDIX C

τ_{xy} FROM THE STRESS CONSTITUTIVE EQUATION

τ_{xy} from the stress constitutive equation (56) is stated below in terms of the orientation tensor $\mathbf{Q}$. The DQ closure is used to approximate all tensor contractions with $\mathbf{M}_4$.

$$\begin{aligned}
\tau_{xy} &= \left(\frac{2}{Re} + \mu_3 a\right) \mathbf{D}_{12} \\
&+ a\alpha\Bigg(\mathbf{Q}_{12} + N\Bigg[.6042J + \mathbf{Q}_{12}(1.4001H - .8021) - 1.2410\frac{JK}{H} \\
&+ 0.6205exp(G)\left(\frac{52}{315}\mathbf{Q}_{12} - \frac{16}{21}J\right)\Bigg]\Bigg) \\
&- \frac{1}{6}\frac{a\alpha}{Er}\Bigg(- 0.0694C - 1.2854\mathbf{Q}_{12}\left(\mathbf{Q}_{22}\frac{\partial^2 \mathbf{Q}_{11}}{\partial y^2} + \mathbf{Q}_{11}\frac{\partial^2 \mathbf{Q}_{22}}{\partial y^2}\right) \\
&- 5.5112\mathbf{Q}_{12}\left(\mathbf{Q}_{11}\frac{\partial^2 \mathbf{Q}_{11}}{\partial y^2} + \mathbf{Q}_{13}\frac{\partial^2 \mathbf{Q}_{13}}{\partial y^2} + \mathbf{Q}_{23}\frac{\partial^2 \mathbf{Q}_{23}}{\partial y^2} + \mathbf{Q}_{22}\frac{\partial^2 \mathbf{Q}_{22}}{\partial y^2}\right) \\
&+ \frac{\partial^2 \mathbf{Q}_{12}}{\partial y^2}\left(-5.55585\mathbf{Q}_{12}^2 - 2.98505\mathbf{Q}_{11}\mathbf{Q}_{22} - 0.04465H + 0.3251\right) \\
&+ 2.9404\left[\mathbf{Q}_{23}\left(\frac{\partial^2 \mathbf{Q}_{11}}{\partial y^2}\mathbf{Q}_{13} - \frac{\partial^2 \mathbf{Q}_{13}}{\partial y^2}\mathbf{Q}_{11} + \mathbf{Q}_{13}\frac{\partial^2 \mathbf{Q}_{22}}{\partial y^2}\right) - \mathbf{Q}_{13}\mathbf{Q}_{22}\frac{\partial^2 \mathbf{Q}_{23}}{\partial y^2}\right] \\
&+ 2.4820\frac{JP}{H} - 1.2410exp(G)\left(-\frac{4}{45}\frac{\partial^2 \mathbf{Q}_{12}}{\partial y^2} - \frac{8}{21}C\right)\Bigg) \\
&- \frac{1}{6}\frac{\alpha}{Er}\Bigg(\frac{\partial^2 \mathbf{Q}_{11}}{\partial y^2}\mathbf{Q}_{12} + \frac{\partial^2 \mathbf{Q}_{12}}{\partial y^2}\mathbf{Q}_{22} + \frac{\partial^2 \mathbf{Q}_{13}}{\partial y^2}\mathbf{Q}_{23} \\
&- \frac{\partial^2 \mathbf{Q}_{12}}{\partial y^2}\mathbf{Q}_{11} - \frac{\partial^2 \mathbf{Q}_{22}}{\partial y^2}\mathbf{Q}_{12} - \frac{\partial^2 \mathbf{Q}_{23}}{\partial y^2}\mathbf{Q}_{13}\Bigg) + \mu_1(a)\mathbf{D}_{12}\left(\mathbf{Q}_{11} + \mathbf{Q}_{22} + \frac{2}{3}\right) \\
&+ \mu_2(a)\mathbf{D}_{12}\Bigg(0.3865H + 0.83855\mathbf{Q}_{12}^2 + .92315\mathbf{Q}_{11}\mathbf{Q}_{22} + .3721(\mathbf{Q}_{22} + \mathbf{Q}_{11}) \\
&+ .1111 - \frac{0.1476J}{H} + 0.0369exp(G)\left(-\frac{8}{45} - \frac{8}{21}\left[\mathbf{Q}_{11} + \mathbf{Q}_{22}\right]\right)\Bigg),
\end{aligned}$$

where

$$C = \frac{\partial^2 \mathbf{Q}_{11}}{\partial y^2}\mathbf{Q}_{12} + \frac{\partial^2 \mathbf{Q}_{12}}{\partial y^2}(\mathbf{Q}_{11} + \mathbf{Q}_{22}) + \frac{\partial^2 \mathbf{Q}_{13}}{\partial y^2}\mathbf{Q}_{23} + \frac{\partial^2 \mathbf{Q}_{22}}{\partial y^2}\mathbf{Q}_{12} + \frac{\partial^2 \mathbf{Q}_{23}}{\partial y^2}\mathbf{Q}_{13},$$

$$\begin{aligned} F = {} & \mathbf{Q}_{12}^2\left(\mathbf{Q}_{11}^2 + 2\mathbf{Q}_{11}\mathbf{Q}_{22} + \mathbf{Q}_{22}^2 + \frac{4}{3}\mathbf{Q}_{11} + \frac{4}{3}\mathbf{Q}_{22} + \frac{4}{9}\right) \\ & +2\mathbf{Q}_{12}\mathbf{Q}_{13}\left(\mathbf{Q}_{11}\mathbf{Q}_{23} + \mathbf{Q}_{22}\mathbf{Q}_{23} + \frac{4}{3}\mathbf{Q}_{23}\right) + \mathbf{Q}_{13}^2\mathbf{Q}_{23}^2, \end{aligned}$$

$$G = \frac{6(\mathbf{Q}_{11}^2 + \mathbf{Q}_{12}^2 + \mathbf{Q}_{13}^2 + \mathbf{Q}_{22}^2 + \mathbf{Q}_{23}^2 + \mathbf{Q}_{11}\mathbf{Q}_{22})}{\left(\mathbf{Q}_{11}^2 + \mathbf{Q}_{12}^2 + \mathbf{Q}_{13}^2 + \mathbf{Q}_{22}^2 + \mathbf{Q}_{23}^2 + \mathbf{Q}_{11}\mathbf{Q}_{22} - \frac{1}{3}\right)},$$

$$H = 2(\mathbf{Q}_{11}^2 + \mathbf{Q}_{12}^2 + \mathbf{Q}_{13}^2 + \mathbf{Q}_{22}^2 + \mathbf{Q}_{23}^2 + \mathbf{Q}_{11}\mathbf{Q}_{22}) + \frac{1}{3},$$

$$J = \mathbf{Q}_{11}\mathbf{Q}_{12} + \mathbf{Q}_{12}\mathbf{Q}_{22} + \mathbf{Q}_{13}\mathbf{Q}_{23} + \frac{2}{3}\mathbf{Q}_{12},$$

$$\begin{aligned} K = {} & 2(\mathbf{Q}_{11}^2 + \mathbf{Q}_{12}^2 + \mathbf{Q}_{13}^2 + \mathbf{Q}_{22}^2 + \mathbf{Q}_{23}^2 + \mathbf{Q}_{11}\mathbf{Q}_{22}) \\ & +3\mathbf{Q}_{11}(\mathbf{Q}_{12}^2 - \mathbf{Q}_{22}^2 - \mathbf{Q}_{23}^2 - \mathbf{Q}_{11}\mathbf{Q}_{22}) \\ & +3\mathbf{Q}_{22}(\mathbf{Q}_{12}^2 - \mathbf{Q}_{13}^2) + 6\mathbf{Q}_{12}\mathbf{Q}_{13}\mathbf{Q}_{23} + \frac{1}{9}, \end{aligned}$$

$$\begin{aligned} P = {} & \frac{\partial^2 \mathbf{Q}_{11}}{\partial y^2}\left(\mathbf{Q}_{12}^2 - \mathbf{Q}_{22}^2 - \mathbf{Q}_{23}^2 - 2\mathbf{Q}_{11}\mathbf{Q}_{22} + \frac{4}{3}\mathbf{Q}_{11} + \frac{2}{3}\mathbf{Q}_{22}\right) \\ & +2\frac{\partial^2 \mathbf{Q}_{12}}{\partial y^2}\left(\mathbf{Q}_{11}\mathbf{Q}_{12} + \mathbf{Q}_{12}\mathbf{Q}_{22} + \mathbf{Q}_{13}\mathbf{Q}_{23} + \frac{2}{3}\mathbf{Q}_{12}\right) \\ & +\frac{\partial^2 \mathbf{Q}_{22}}{\partial y^2}\left(-\mathbf{Q}_{11}^2 + \mathbf{Q}_{12}^2 - \mathbf{Q}_{13}^2 - 2\mathbf{Q}_{11}\mathbf{Q}_{22} + \frac{2}{3}\mathbf{Q}_{11} + \frac{4}{3}\mathbf{Q}_{22}\right) \\ & +\frac{\partial^2 \mathbf{Q}_{13}}{\partial y^2}\left(2\mathbf{Q}_{12}\mathbf{Q}_{23} - 2\mathbf{Q}_{13}\mathbf{Q}_{22} + \frac{4}{3}\mathbf{Q}_{13}\right) \\ & +2\frac{\partial^2 \mathbf{Q}_{23}}{\partial y^2}\left(-\mathbf{Q}_{11}\mathbf{Q}_{23} + \mathbf{Q}_{12}\mathbf{Q}_{13} + \frac{2}{3}\mathbf{Q}_{23}\right). \end{aligned}$$

VITA

Traci Ann Sievenpiper
Department of Mathematics and Statistics
Old Dominion University
Norfolk, VA 23529

Education:
-M.S. Applied Mathematics, Old Dominion University (Norfolk, VA), May 2008
-B.S. Computer Engineering, University of Pittsburgh (Pittsburgh, PA), April 2002

Employment:
Lecturer, Lasell College (Newton, MA), Fall 2010-Spring 2011
Adjunct Instructor, SUNY Adirondack (Wilton, NY) Fall 2008-Fall 2010
Instructor, Old Dominion University (Norfolk, VA) Fall 2007-Spring 2008

Research Presentations:
-A least square closure approximation for liquid crystalline polymers based on kinetic simulations, Society of Industrial and Applied Mathematics (SIAM) Annual Meeting (Pittsburgh, Pennsylvania), Jul 2010
-A least square closure approximation for liquid crystalline polymers based on kinetic simulations, Southeastern Atlantic Mathematical Science (SEAMS) Cha-Cha Days Workshop (Orlando, Florida), Nov 2009
-A comparison of closure rules for the Doi-Hess theory of the liquid crystalline polymers, Old Dominion University SIAM Student Chapter-Math Awareness Conference (Norfolk, Virginia), April 2008
-Poster: A comparison of closure rules for the Doi-Hess theory of the liquid crystalline polymers, Old Dominion University Office of Research-Annual Research Exposition (Norfolk, Virginia), April 2008

Typeset using LaTeX.